# The Instability of Mesoscale Jets in Idealized Two-Layer Models

by

Robert Irwin

A thesis
presented to the University of Waterloo
in fulfillment of the
thesis requirement for the degree of
Master of Mathematics
in
Applied Mathematics

Waterloo, Ontario, Canada, 2014

© Robert Irwin 2014

## Author's Declaration

I hereby declare that I am the sole author of this thesis. This is a true copy of the thesis, including any required final revisions, as accepted by my examiners.

I understand that my thesis may be made electronically available to the public.

**Abstract**

The rotating shallow water (RSW) equations have been used extensively in oceanographic literature to model dynamical elements of the world's oceans and atmosphere at large scales. The RSW model is a simple and useful model of geophysical fluids because it allows for the consideration of rotation, topography, and, by adding layers, the effects of stratification. In this thesis, the RSW model will be used to investigate the instability of two-layer, mesoscale, Bickley jets. Several different jet configurations will be used to accentuate different types of instabilities in the flow. The two primary instabilities investigated are barotropic (BT) and baroclinic (BC) instabilities, and the classical models of these two instabilities will be discussed. In addition to the RSW model, a piecewise constant potential vorticity (PV) quasi-geostrophic (QG) model will also be introduced. This QG model is more restrictive than the RSW model because it does not admit steep topography, nor does it describe flows of length-scales much different than the Rossby radius of deformation. However, because the model is simpler, it is more efficient to use to explore parameter space. In this thesis, the RSW and QG models will be used in tandem to describe stability characteristics of mesoscale jets over a wide parameter space in both the linear and nonlinear regimes. Finally the effects of stratification and rotation, and the effects of shelflike topography on mesoscale jets will be addressed.

**Acknowledgements**

I would like to thank the entire Environmental and Geophysical Fluids Group for offering guidance and direction during the writing of this thesis. A special thanks goes to Dr. Francis Poulin for his counsel and insight throughout my graduate studies.

## Dedication

To the Toronto Maple Leafs organization. May this thesis bring them strength and resilience for years to come.

# Table of Contents

# List of Tables

# List of Figures

The notation used in this text follows the notation in Vallis, [30], closely. When referring to the shallow water model, the pressure will be written in terms of the interface displacements, $\eta$, or layer depths, $h$, for what is most convenient at the time.

| **Variable** | **Description** |
|---|---|
| $x, y, z$ | Coordinates representing zonal, meridional and vertical position respectively. |
| $u, v, w$ | Velocity in the zonal, meridional and vertical directions, respectively. |
| $\zeta$ | Third component of vorticity, $\frac{\partial v}{\partial x} - \frac{\partial u}{\partial y}$. |
| $p$ | Pressure. |
| $h$ | Layer thickness. |
| $\eta$ | Interface displacement. |
| $\eta_b$ | Height of the lower surface (bottom topography). |
| $\cdot_i$ | Property $\cdot$ of layer $i$. The surface layer corresponds to $i = 1$. |
| $g$ | Acceleration due to gravity. |
| $g'$ | Reduced gravity coefficient. |
| $f$ | The Coriolis parameter. |
| $Ro$ | Rossby number, $\frac{U_0}{fL}$. |
| $Bu$ | Burger number, $\frac{gH}{f^2L^2}$. |
| $\frac{\mathrm{D}}{\mathrm{D}t}$ | Material derivative, $\frac{\partial}{\partial t} + u\frac{\partial}{\partial x} + v\frac{\partial}{\partial y}$. |

# Chapter 1

# Introduction

Pressure, gravity, thermal forcing, rotation, and a myriad of other forces contribute to the evolving dynamics of the world's oceans. Modeling the entire oceanic system from small scale wave-breaking to large scale global circulation is a daunting task. Since the 1800's, physicists have attempted to identify, characterize, and explain each piece of the ocean physics mosaic. Lord Rayleigh, Osborne Reynolds, Henri Bénard, and others pioneered methods of mathematical analysis to explain complicated fluid behaviours using simple mathematical models. G.I. Taylor, Eric Eady, Jule Charney, and Horace Lamb were among the next generation to further mathematical techniques applied to fluid dynamics. Afterwards, the dawn of the information age brought massive computational power to the hands of fluids dynamicists. This computing potential is at the forefront of modern fluid dynamics research. In this thesis, the stability of mesoscale oceanographic flows are studied using classical linear stability analyses, and modern computational techniques.

Nonlinear *partial differential equations* (PDEs) form the core of fluid dynamics (specifically, the Rotating Shallow Water (RSW) equations will be used to analyze large-scale fluid flow in this thesis). General solutions of many nonlinear PDEs do not exist, and so other mathematical techniques are used to extract quantitative information from the system. One such classical technique is *linear stability analysis*, which has been used since the 1800's, and is still widely used in modern oceanography, [9], [20], [21], [22].

Lord Rayleigh used the technique of linear stability analysis to develop necessary conditions of instability for horizontal shear flows. Kuo expanded on Rayleigh's analysis to derive the Rayleigh-Kuo criterion for *barotropic* (BT) instability, [30]. Barotropic instability is an important mechanism that can form vortices that transport fluid properties over large distances and timescales, and can be identified by flows whose perturbations extract

energy from horizontal shear of the basic state, [18]. In addition to barotropic instability, the mechanism of *baroclinic* (BC) instability is the other important mechanism of instability discussed in this work. Baroclinic instability is identified by perturbations extracting available potential energy of the basic state, [18]. Eric Eady [7], and Jule Charney [5] were the first to quantify this process, and studies of baroclinically unstable flows are prominent in modern fluids literature, [1], [15], [23].

The multi-layer RSW equations form a simple mathematical model that will be used to study shear flows in the following chapters. It is limited to discretely stratified layers of immiscible fluid, but it allows for both BT and BC instabilities and is more general than other simplified models, such as the quasi-geostrophic (QG) model. Additionally, the model admits steep topographic deformations that allow for the investigation of topographic effects on geophysical flows. Many studies have used the RSW model paradigm to investigate large-scale fluid processes, [3], [13] & [12], [2], [31], and the model will be used extensively in this thesis to investigate linear stability and nonlinear evolution of unstable jets.

Despite the simplicity of the RSW model, the linear stability of general channel-like flows is not analytically solvable. Numerical techniques must be applied to solve large eigenvalue problems. This is problematic as these methods are often slow and computationally taxing. An even simpler model, which admits semi-analytic solutions to the linear stability analysis, is the piecewise constant Potential Vorticity (PV) QG model, that is used extensively in modern geophysical analysis, [16], [4], [26], [27]. This model is derived under more restrictive assumptions, but it will be shown that the qualitative predictions of the model extend outside of the regime where one might expect the model to be valid.

The aforementioned RSW and QG models permit forms of topography that may influence stability characteristics of certain flows. In this thesis, the effect of shelflike topography on the stability of jets will be investigated in the context of a two-layer flow. Shelflike topography occurs when the flow moves along a shelf (i.e. when topography varies perpendicular to the direction of flow). The influence of topography on instability has been investigated in many paradigms including: the single-layer RSW model [21], the single layer QG model [4], [26], the two-layer QG model [27], a continuously stratified model [14], and in the three-layer RSW model [25]. This is by no means a comprehensive review of the literature, but merely shows the ubiquity of the topic in current research. This thesis will investigate the effects of shelflike topography on barotropically and baroclinically unstable mesoscale jets using both two-layer QG and two-layer RSW models.

This thesis will focus on the stability characteristics of Bickley jets in the two-layer RSW model and two-layer QG model. In particular, two configurations of Bickley jets

will be investigated: a primarily barotropic case, and a mixed barotropic-baroclinic case. Non-dimensional parameters will be varied for both of these configurations. The Rossby parameter regimes investigated include the quasi-geostrophic regime, $Ro \ll 1$, and the intermediate regime $Ro \sim 1$. Additionally, varying values of stratification will be used — weak stratification, $g' = 0.01$, strong stratification, $g' = 0.1$, and in some cases, very strong stratification $g' = 1$. These stratification values are chosen, as they are representative of values commonly found in the interior of the world's oceans, [28].

The structure of this thesis will be as follows. Chapter 2 will present the underlying mathematical models and techniques used to investigate two-layer flows. Chapter 3 will conduct parameter sweeps over the Rossby number and stratification parameters for four Bickley jet configurations. Chapter 4 will extend the results of chapter three by analyzing the effects of topography on the unstable systems presented in the previous chapter. Finally, chapter 5 will summarize the findings of this work.

# Chapter 2

# Methods and Background

## 2.1 The Model Equations

The RSW equations will be derived in this section for both single- and multi-layer models. Additionally, the multi-patch constant vorticity two-layer QG model will be derived.

### 2.1.1 The Single Layer Model

Although this work focuses on multi-layered models, the single layer model is presented as a starting point. This model is largely pedagogical, but it does recover some important physical phenomena in the ocean. Notationally, the positive $z$-direction is pointing up, starting with $z = 0$ at the bottom of the fluid. The horizontal components are defined as usual, with the positive $x$-direction pointing east, and the positive $y$-direction pointing north.

#### Assumptions

The single layer RSW model is a simple, idealized form of standard large-scale fluid motion. There are several assumptions that it requires.

1. The length scale is much larger than the height scale (as implied by the name). Mathematically,

$$L \gg H. \tag{2.1}$$

2. The density is constant in the fluid. Stratification effects can be emulated by using multi-layer models.

$$\rho(x, y, z, t) = \rho_0. \tag{2.2}$$

3. The fluid is in hydrostatic equilibrium, and the pressure at the surface is negligible.

$$\frac{\partial p}{\partial z} = -g\rho, \tag{2.3}$$

$$p(x, y, z = \eta, t) = 0. \tag{2.4}$$

4. The horizontal velocities are assumed to be invariant with depth in each layer,

$$\vec{u} = \vec{u}(x, y, t). \tag{2.5}$$

Additionally, the effects of surface tension and viscosity will be neglected.

**Deriving the Momentum Equations**

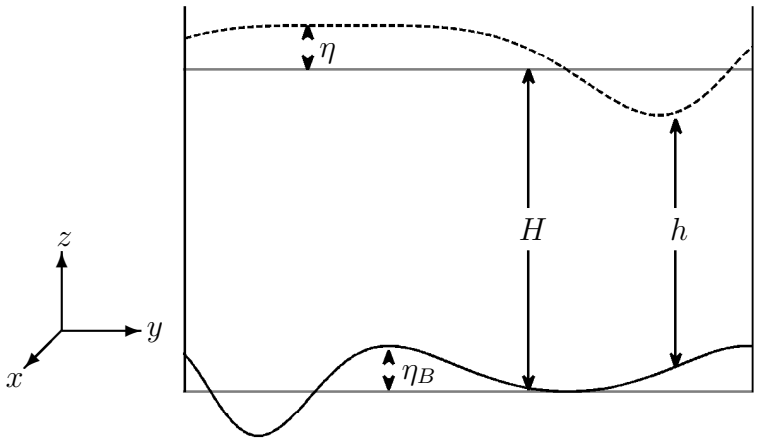


Figure 2.1: The one-layer rotating shallow water model.

By assuming hydrostatic equilibrium, the vertical momentum equation simply reduces to,

$$\frac{\partial p}{\partial z} = -g\rho. \tag{2.6}$$

The density is constant and so this can be integrated to yield,

$$p(x, y, z, t) = -g\rho z + p_0(x, y, t), \tag{2.7}$$

where $p_0$ is the function obtained as a result of integration. The pressure is assumed to be nil at the surface, $z = \eta + H$, allowing an expression for $p_0$ to be obtained,

$$p_0(x, y, t) = g\rho(\eta(x, y, t) + H). \tag{2.8}$$

Thus, the vertical momentum equation yields the expression for pressure,

$$p(x, y, z, t) = g\rho(\eta(x, y, t) + H - z). \tag{2.9}$$

The horizontal equations of motion come from the Euler momentum equations in a rotating frame of reference,

$$\frac{\mathrm{D}\vec{u}}{\mathrm{D}t} + 2\vec{\Omega} \times \vec{u} = -\frac{1}{\rho}\vec{\nabla}p. \tag{2.10}$$

Using the assumption that the velocities are invariant with respect to depth, the horizontal momentum equations are:

$$\frac{\partial u}{\partial t} + u\frac{\partial u}{\partial x} + v\frac{\partial u}{\partial y} - fv = -g\frac{\partial \eta}{\partial x}, \tag{2.11a}$$

$$\frac{\partial v}{\partial t} + u\frac{\partial v}{\partial x} + v\frac{\partial v}{\partial y} + fu = -g\frac{\partial \eta}{\partial y}. \tag{2.11b}$$

**Conservation of Mass**

We consider a column of fluid of height $h(x, y, t)$ and base area $A$. The total mass of the fluid column is:

$$M = \iint_A \rho h \, \mathrm{d}A. \tag{2.12}$$

The rate of change of mass in the fluid column is the time derivative of $M$.

$$\frac{d}{dt}M = \frac{d}{dt}\iint_A \rho h \, \mathrm{d}A. \tag{2.13}$$

If $A$ is a material surface, the Reynolds Transport Theorem can be applied,

$$\frac{dM}{dt} = \iint_A \rho \frac{\partial h}{\partial t}\, \mathrm{d}A + \oint_{\partial A} \rho h \vec{u} \cdot \hat{n}\, \mathrm{d}S \qquad \text{Use Divergence Theorem,} \tag{2.14}$$

$$= \iint_A \rho \frac{\partial h}{\partial t}\, \mathrm{d}A + \iint_A \vec{\nabla} \cdot (\rho h \vec{u})\ \mathrm{d}A, \tag{2.15}$$

$$= \iint_A \rho \left[ \frac{\partial h}{\partial t} + \vec{\nabla} \cdot (h\vec{u}) \right]\ \mathrm{d}A. \tag{2.16}$$

If mass is conserved then $\frac{dM}{dt} = 0$. The base area $A$ is an arbitrary material surface, thus, the integrand must vanish, yielding the mass continuity equation,

$$\frac{\partial h}{\partial t} + \vec{\nabla} \cdot (h\vec{u}) = 0. \tag{2.17}$$

**Summary of the Single Layer RSW Equations**

The complete RSW equations are given below,

$$\frac{\mathrm{D}\vec{u}}{\mathrm{D}t} + \left( f\hat{k} \times \vec{u} \right) = -g\vec{\nabla}\eta, \tag{2.18a}$$

$$\frac{\partial h}{\partial t} + \vec{\nabla} \cdot (h\vec{u}) = 0. \tag{2.18b}$$

The pressure in the interior of the fluid is,

$$p(x, y, z, t) = g\rho \left[ \eta(x, y, t) + H - z \right]. \tag{2.18c}$$

It is noted that $\eta$ and $h$ are related by the following,

$$\eta(x, y, t) = h(x, y, t) - H + \eta_b(x, y). \tag{2.18d}$$

**Conservation of Potential Vorticity**

Consider the momentum equations,

$$\frac{\partial u}{\partial t} + u\frac{\partial u}{\partial x} + v\frac{\partial u}{\partial y} - fv = -g\frac{\partial \eta}{\partial x}, \tag{2.19}$$

$$\frac{\partial v}{\partial t} + u\frac{\partial v}{\partial x} + v\frac{\partial v}{\partial y} + fu = -g\frac{\partial \eta}{\partial y}. \tag{2.20}$$

The cross derivatives of the above equations are taken, yielding:

$$\frac{\partial^2 u}{\partial y \partial t} + \frac{\partial u}{\partial y}\frac{\partial u}{\partial x} + u\frac{\partial^2 u}{\partial x \partial y} + \frac{\partial v}{\partial y}\frac{\partial u}{\partial y} + v\frac{\partial^2 u}{\partial y^2} - f\frac{\partial v}{\partial y} = -g\frac{\partial^2 \eta}{\partial x \partial y}, \tag{2.21}$$

$$\frac{\partial^2 v}{\partial x \partial t} + \frac{\partial u}{\partial x}\frac{\partial v}{\partial x} + u\frac{\partial^2 v}{\partial x^2} + \frac{\partial v}{\partial x}\frac{\partial v}{\partial y} + v\frac{\partial^2 v}{\partial x \partial y} + f\frac{\partial u}{\partial x} = -g\frac{\partial^2 \eta}{\partial x \partial y}. \tag{2.22}$$

The vorticity variable $\zeta = \frac{\partial v}{\partial x} - \frac{\partial u}{\partial y}$ is introduced. Subtracting the previous equations recovers the vorticity equation.

$$\frac{\partial \zeta}{\partial t} + \left(\vec{u} \cdot \vec{\nabla}\right)\zeta + (\zeta + f)\,\vec{\nabla} \cdot \vec{u} = 0. \tag{2.23}$$

The above equation can be simplified,

$$\frac{\mathrm{D}}{\mathrm{D}t}(\zeta + f) = -(\zeta + f)\,\vec{\nabla} \cdot \vec{u}. \tag{2.24}$$

Each term in (2.24) bears a physical meaning. In particular, the equation states that a moving column of absolute vorticity $(\zeta + f)$ is only modified in the presence of convergence or divergence and non-zero absolute vorticity, [18].

This equation can be simplified further by rearranging the continuity equation to solve for the horizontal divergence,

$$\vec{\nabla} \cdot \vec{u} = -\frac{1}{h}\frac{\mathrm{D}h}{\mathrm{D}t}. \tag{2.25}$$

Using this result, equation (2.24) can be modified as,

$$\frac{\mathrm{D}}{\mathrm{D}t}(\zeta + f) - \frac{(\zeta + f)}{h}\frac{\mathrm{D}h}{\mathrm{D}t} = 0. \tag{2.26}$$

Noting again that $f$ is constant under the $f$-plane approximation, this can be written in conservation form:

$$\frac{\mathrm{D}}{\mathrm{D}t}\left[\frac{\zeta + f}{h}\right] = 0. \tag{2.27}$$

The term $Q = \frac{\zeta + f}{h}$ is known as the shallow water potential vorticity and it is a material invariant in the RSW equations.

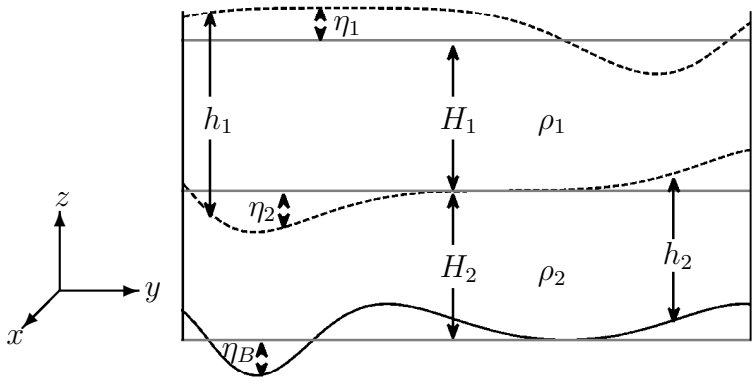


Figure 2.2: The two-layer rotating shallow water model.

### 2.1.2 The Multi-Layer Model

The single layer model is adequate for describing some aspects of horizontal shear in the ocean, but it fails to address effects of stratification and vertical shear. A simple extension to this model is to add layers of fluid on top of each other, effectively "stacking" coupled shallow water layers. The list of assumptions for the multi-layer model includes all of the single layer assumptions and adds the following:

1. The fluids are immiscible. Density is not diffused and the interface is the only way in which the fluids interact.

2. While the density is discontinuous at the interface, the pressure is continuous.

The physical variables, $\vec{u}, p$ will be split into layer-wise variables,

$$[\vec{u}, p] = \begin{cases} [\vec{u}_1(x,y,t), p_1(x,y,t)], & \eta_1 + H > z > \eta_2 + H - H_1, \\ [\vec{u}_2(x,y,t), p_2(x,y,t)], & \eta_2 + H - H_1 > z > \eta_3 + H - H_1 - H_2, . \\ \vdots \end{cases} \tag{2.28}$$

The horizontal momentum equations remain similar in structure to the single layer case,

$$\frac{\mathrm{D}\vec{u}_i}{\mathrm{D}t} + 2\vec{\Omega} \times \vec{u}_i = -\frac{1}{\rho_i}\vec{\nabla} p_i, \tag{2.29}$$

however the form of $p_i$, the pressure in each layer, changes. The coupling of the equations occurs in the pressure variables. In order to determine the form of $p_i$, the hydrostatic balance equation is integrated in each layer. For example consider $z \in (H-H_1+\eta_2, H+\eta_1)$,

$$\frac{\partial p_1}{\partial z} = -\rho_1 g, \tag{2.30}$$

$$p_1(x,y,z,t) = \rho_1 g \left(H + \eta_1(x,y,t) - z\right). \tag{2.31}$$

In the second layer, there is the contribution of pressure from the first layer in addition to the contribution from the interface displacement of the second layer. Writing this in terms of variables yields,

$$p_2(x,y,z,t) = p_1(x,y,H-H_1+\eta_2,t) + \rho_2 g \left(H - H_1 + \eta_2 - z\right), \tag{2.32}$$

$$= \rho_1 g \left(\eta_1 + H_1 - \eta_2\right) + \rho_2 g \left(H - H_1 + \eta_2 - z\right), \tag{2.33}$$

$$= \rho_1 g \eta_1 + \rho_1 g_1' \eta_2 - \rho_1 g_1' H_1 + \rho_2 g (H - z). \tag{2.34}$$

where the reduced gravity at the interface is $g_1' = g(\rho_2 - \rho_1)/\rho_1$. It will be seen that only the horizontal derivatives of pressure occur in the momentum equations, thus the dependence on $z$ will not play a role in the dynamics. The gradient of pressure in layer two may now be written as,

$$\vec{\nabla} p_2(x,y,z,t) = \vec{\nabla}\left(\rho_1 g \eta_1 + \rho_1 g_1' \eta_2\right). \tag{2.35}$$

Continuing this integration for $N$ layers of fluid, the pressure gradient in layer $n$ can be expressed as a sum,

$$\vec{\nabla} p_n = \rho_1 \sum_{i=1}^{n} g_{i-1}' \vec{\nabla} \eta_i, \quad n \geq 1, \tag{2.36}$$

where $g_i' = g(\rho_{i+1} - \rho_i)/\rho_1$ for $i \geq 1$ and $g_0' = g$. The exact equations for pressure have a vertical dependence, see [30] for more details.

The mass conservation equations will maintain the same form as the single layer case. To show this, consider a column of fluid in an arbitrary layer, $n$. The mass of the column is:

$$M = \iint_A \rho_n \left(H_n + \eta_n - \eta_{n+1}\right) \, dA. \tag{2.37}$$

The bracketed term in the integrand is now rewritten as $h_n$. Following the same steps as the one layer case yields the continuity equation in each layer,

$$\frac{\partial h_n}{\partial t} + \vec{\nabla} \cdot (h_n \vec{u}_n) = 0. \tag{2.38}$$

### Summary of the Multi-Layer RSW Equations

The layer-wise momentum equations and continuity equation for the multi-layer rotating shallow water equations are presented here:

$$\frac{\partial \vec{u}_n}{\partial t} + \left(\vec{u}_n \cdot \vec{\nabla}\right) \vec{u}_n + f \times \vec{u}_n = -\frac{1}{\rho_n}\vec{\nabla} p_n, \tag{2.39a}$$

$$\frac{\partial h_n}{\partial t} + \vec{\nabla} \cdot (h_n \vec{u}_n) = 0, \tag{2.39b}$$

where,

$$\vec{\nabla} p_n = \vec{\nabla}\left[\rho_1 \sum_{i=1}^{n} g'_{i-1}\eta_i\right]. \tag{2.40}$$

Where $g'_i = g\left(\rho_{i+1} - \rho_i\right)/\rho_1$ for $i \geq 1$ and $g'_0 = g$.

### Extending the Conservation of Potential Vorticity to Multiple Layers

The material conservation of potential vorticity extends simply to multiple layers. The algebra is nearly identical to the single layer case, and so it will not be repeated here. The potential vorticity conservation statement for an $N$ layer system reduces to,

$$\frac{\mathrm{D}_i}{\mathrm{D}t} \underbrace{\left[\frac{\zeta_i + f}{h_i}\right]}_{Q_i} = 0, \qquad i = 1, \ldots, N \tag{2.41}$$

where

$$\frac{\mathrm{D}_i}{\mathrm{D}t} = \frac{\partial}{\partial t} + u_i \frac{\partial}{\partial x} + v_i \frac{\partial}{\partial y}, \tag{2.42}$$

$$\zeta_i = \frac{\partial v_i}{\partial x} - \frac{\partial u_i}{\partial y}, \tag{2.43}$$

$$h_i = H_i + \eta_i - \eta_{i+1}. \tag{2.44}$$

In other words, the potential vorticity of layer $i$ is a materially conserved quantity in layer $i$.

**The Two-Layer RSW Equations**

This thesis focusses on the $N = 2$ case of the multi-layer equations and so these equations are explicitly stated below.

$$\frac{\partial \vec{u}_1}{\partial t} + \left(\vec{u}_1 \cdot \vec{\nabla}\right) \vec{u}_1 + \vec{f} \times \vec{u}_1 = -g\vec{\nabla}\left[h_1 + h_2 + \eta_b\right], \tag{2.45a}$$

$$\frac{\partial h_1}{\partial t} + \vec{\nabla} \cdot (h_1 \vec{u}_1) = 0, \tag{2.45b}$$

$$\frac{\partial \vec{u}_2}{\partial t} + \left(\vec{u}_2 \cdot \vec{\nabla}\right) \vec{u}_2 + \vec{f} \times \vec{u}_2 = -\frac{\rho_1}{\rho_2}\vec{\nabla}\left[g\left(h_1 + h_2 + \eta_b\right) + g'\left(h_2 + \eta_b\right)\right], \tag{2.45c}$$

$$\frac{\partial h_2}{\partial t} + \vec{\nabla} \cdot (h_2 \vec{u}_2) = 0, \tag{2.45d}$$

where $\vec{u}_i = (u_i, v_i)$.

### 2.1.3 Semi-Analytic Quasi-Geostrophic Model

The QG model assumes that interfacial and surface deformations are small compared to the depth of the fluid and that the scale of motion is not significantly larger, or smaller, than the deformation scale of the system, [30]. The two layer analogue of QG consists of two equations and two variables, the streamfunctions, to describe the dynamics of a two-layer system. Clearly this is simpler than the two-layer RSW model which consists of six equations and six unknowns.

Begin with the two-layer quasi-geostrophic equations. The quasi-geostrophic potential vorticity in each layer is,

$$q_1 = \nabla^2\psi_1 + \frac{f^2}{g'H_1}\left(\psi_2 - \psi_1\right) + \frac{f^2}{gH_1}\psi_1, \tag{2.46a}$$

$$q_2 = \nabla^2\psi_2 + \frac{f^2}{g'H_2}\left(\psi_1 - \psi_2\right) + f\frac{\eta_b}{H_2}, \tag{2.46b}$$

with evolution equation,

$$\frac{\partial q_i}{\partial t} + J(\psi_i, q_i) = 0. \tag{2.46c}$$

Here, $J(A, B) = \frac{\partial A}{\partial x}\frac{\partial B}{\partial y} - \frac{\partial A}{\partial y}\frac{\partial B}{\partial x}$, is the Jacobian operator. The streamfunctions satisfy the standard equations,

$$u_i = -\frac{\partial \psi_i}{\partial y}, \qquad v_i = \frac{\partial \psi_i}{\partial x}, \tag{2.47}$$

and can be expressed in terms of the perturbations of interfaces,

$$\eta_0' = \frac{f}{g}\psi_1, \qquad \eta_1' = \frac{f}{g'}\left(\psi_2 - \psi_1\right). \tag{2.48}$$

It is important to note that these values are perturbations of the basic state variables $\eta_0$ and $\eta_1$, see [30] for more details.

For the cases presented here a rigid lid and flat bottom will be considered, and so the last terms of (2.46a) and (2.46b) will be ignored. This is due to $\eta_0' \to 0$, which causes the last term of $q_1$ to be eliminated, and $\eta_b \to 0$, which causes the last term of $q_2$ to be eliminated, [30].

Consider a mean state layer-wise potential vorticity (streamfunction), $Q_n(y)$ ($\Psi_n(y)$), and perturbation potential vorticity (streamfunction) $q_n'(x,y,t)$ ($\psi_n'(x,y,t)$), and linearize the evolution equations,

$$\frac{\partial q_n'}{\partial t} + \frac{\partial \psi_n'}{\partial x}\frac{dQ_i}{dy} - \frac{\partial q_n'}{\partial x}\frac{d\Psi_n}{dy} = 0. \tag{2.49}$$

This can be written in terms of the streamfunctions as,

$$\left(\frac{\partial}{\partial t} + U_n\frac{\partial}{\partial x}\right)\left[\nabla^2\psi_n' - (-1)^n\frac{f^2}{g'H_n}\left(\psi_2' - \psi_1'\right)\right] + \frac{dQ_n}{dy}\frac{\partial \psi_n'}{\partial x} = 0. \tag{2.50}$$

Apply a normal mode decomposition of the form $\psi_n = \hat{\psi}_n(y)e^{ik(x-ct)}$, and substitute into the previous equation,

$$\left(U_n - c\right)\left[\frac{d^2\hat{\psi}_n}{dy^2} - k^2\hat{\psi}_n - (-1)^n\frac{f^2}{g'H_n}\left(\hat{\psi}_2 - \hat{\psi}_1\right)\right] + \hat{\psi}_n\frac{dQ_n}{dy} = 0. \tag{2.51}$$

This equation is not simple to solve in general. The solution of $\hat{\psi}_n$ inherently depends on $c$, creating a complicated eigenvalue problem. Instead of considering a general case, one can make the assumption that the basic state potential vorticity is constant, $\frac{dQ_n}{dy} = 0$. This simplifies the equations significantly and leads to an analytical treatment of the equations.

The requirement that $\frac{dQ_n}{dy} = 0$ means that the basic state is restricted to velocities of

the form,

$$0 = -\frac{d^2U_n}{dy^2} + (-1)^n \frac{f^2}{g'H_1}(U_2 - U_1),$$

$$\Rightarrow U_1(y) = C_1 \frac{g'H_1H_2}{f^2(H_1+H_2)} e^{-y\sqrt{\frac{f^2(H_1+H_2)}{g'H_1H_2}}} + C_2 \frac{g'H_1H_2}{f^2(H_1+H_2)} e^{y\sqrt{\frac{f^2(H_1+H_2)}{g'H_1H_2}}} + C_3 y + C_4, \tag{2.52a}$$

$$U_2(y) = -C_1 \frac{g'H_1^2}{f^2(H_1+H_2)} e^{-y\sqrt{\frac{f^2(H_1+H_2)}{g'H_1H_2}}} - C_2 \frac{g'H_1^2}{f^2(H_1+H_2)} e^{y\sqrt{\frac{f^2(H_1+H_2)}{g'H_1H_2}}} + C_3 y + C_4. \tag{2.52b}$$

If it is further assumed that $U_i \neq c$ (no critical levels), then the solution to the equations for $\hat{\psi}_i$ are found by solving equation (2.51),

$$\hat{\psi}_1 = C_1 e^{ky} + C_2 e^{-ky} + C_3 e^{\kappa y} + C_4 e^{-\kappa y}, \tag{2.53a}$$

$$\hat{\psi}_2 = C_1 e^{ky} + C_2 e^{-ky} - \frac{H_2}{H_1} C_3 e^{\kappa y} - \frac{H_2}{H_1} C_4 e^{-\kappa y}, \tag{2.53b}$$

$$\text{where} \quad \kappa = \sqrt{k^2 + \frac{f^2}{g'} \frac{H_1+H_2}{H_1H_2}}.$$

The constants are determined by the boundary/far-field/matching conditions.

The assumption that PV is constant limits the solutions of the streamfunctions to the form presented in equation (2.53). The works of [4], and [26], [27], presented models that allowed for the investigation of the stability of piecewise constant PV jets. The following section will follow [27] closely.

### Basic Setup

Consider a basic state velocity profile, $U_1(y)$ and $U_2(y)$ divided into $n$ meridional slices. The basic state velocity profiles are continuous across the potential vorticity jumps. Considering the geostrophic balance equations, it is seen that the streamfunctions $\psi_n$ must be continuous,

$$U_n = -\frac{\partial \psi_n}{\partial y}. \tag{2.54}$$

If $\psi_n$ were discontinuous, infinite velocities would be admissible and there would be infinite energy in the system, which is unphysical. Thus, the first condition is,

$$[\hat{\psi}_n]_{y_0} = 0, \quad \text{where } y_0 \text{ is a break and} \quad [X]_{y_0} = X(y_0^+) - X(y_0^-). \tag{2.55}$$

Now integrate equation (2.51) across a profile break $y_0$,

$$\int_{y_0-\varepsilon}^{y_0+\varepsilon} \left\{ (U_n - c)\left[\frac{d^2\hat{\psi}_n}{dy^2} - k^2\hat{\psi}_n - (-1)^n \frac{f^2}{g'H_n}(\hat{\psi}_2 - \hat{\psi}_1)\right] + \hat{\psi}_n \frac{dQ_n}{dy} \right\} dy = 0. \tag{2.56}$$

If $\varepsilon \to 0$, then continuous quantities can be assumed constant, and taken out of the integral. In this case, $U_n$ are assumed to be continuous, and by the first condition, equation (2.55), the integral reduces to the following,

$$\left[(U_n - c)\frac{d\hat{\psi}_n}{dy}\right]_{y_0} + \int_{y_0-\varepsilon}^{y_0+\varepsilon} \hat{\psi}_n \frac{dQ_n}{dy}\, dy = 0. \tag{2.57}$$

Substitute the equation for $\frac{dQ_n}{dy}$ into the previous equation to yield,

$$\left[(U_n - c)\frac{d\hat{\psi}_n}{dy}\right]_{y_0} + \int_{y_0-\varepsilon}^{y_0+\varepsilon} \hat{\psi}_n \left[-\frac{d^2U_n}{dy^2} - (-1)^n \frac{f^2}{g'H_n}(U_1 - U_2)\right] dy = 0. \tag{2.58}$$

Once again, using $\hat{\psi}_n$ and $U_n$ are continuous, the equation reduces to,

$$\left[(U_n - c)\frac{d\hat{\psi}_n}{dy} - \hat{\psi}_n \frac{dU_n}{dy}\right]_{y_0} = 0. \tag{2.59}$$

The conditions presented in [27] are as follows,

$$\left[\frac{\hat{\psi}_n}{U_n - c}\right]_{y_0} = 0, \tag{2.60a}$$

$$\left[(U_n - c)\frac{d\hat{\psi}_n}{dy} - \hat{\psi}_n \frac{dU_n}{dy}\right]_{y_0} = 0. \tag{2.60b}$$

The first condition presented before (equation (2.55)) is equivalent to the first condition here because $U_n$ is continuous. In an $n$-patch model, these conditions will be applied $(n-1)$ times for each layer.

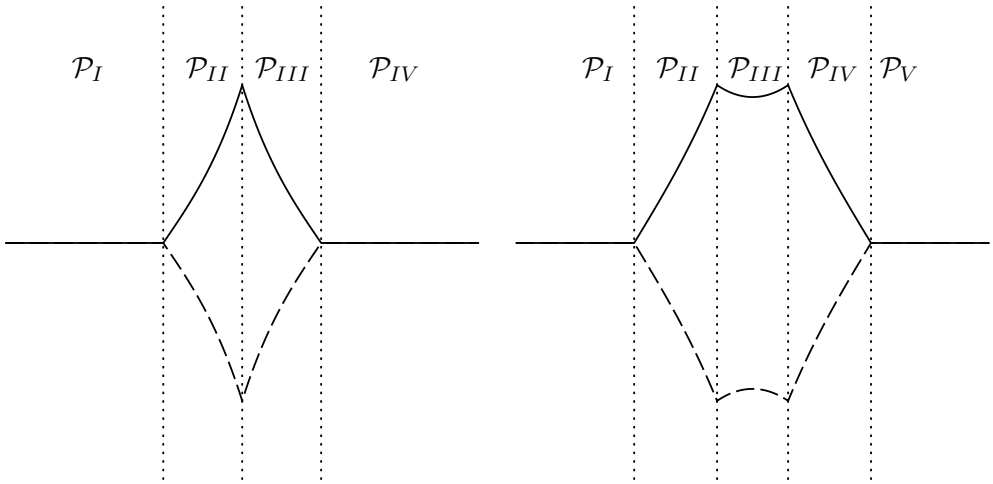


Figure 2.3: Left: the two-layer, four-patch model. Right: the two-layer, five-patch model. The solid and dashed lines represent the zonal velocity profile in the surface and bottom layers (respectively). The dotted lines indicated regions where the potential vorticity value jumps.

**The Five-Patch Problem**

Split the $y$-domain into 5 parts,

$$\mathcal{P}_I = \{y \mid y \in (-\infty, -L)\}, \tag{2.61}$$
$$\mathcal{P}_{II} = \{y \mid y \in [-L, -\alpha L)\}, \tag{2.62}$$
$$\mathcal{P}_{III} = \{y \mid y \in [-\alpha L, \alpha L)\}, \tag{2.63}$$
$$\mathcal{P}_{IV} = \{y \mid y \in [\alpha L, L)\}, \tag{2.64}$$
$$\mathcal{P}_V = \{y \mid y \in [L, \infty)\}. \tag{2.65}$$

For this setup, a thin jet is confined into patches $\mathcal{P}_{II}, \mathcal{P}_{III}$, and $\mathcal{P}_{IV}$. The value of $\alpha$ is physically restricted to the interval $(0, 1)$, and $L$ corresponds to the half-width of the jet. The jump conditions are applied at $-L$, $-\alpha L$, $\alpha L$, and $L$, for each layer, corresponding to a total of 16 conditions.

In each patch, the basic state potential vorticity gradient is identically zero and so the streamfunctions have the form of equations (2.53). Hence there are ten equations and

twenty unknowns, of the form,

$$\hat{\psi}_{(X)(1)} = C_{(X)1}e^{ky} + C_{(X)2}e^{-ky} + C_{(X)3}e^{\kappa y} + C_{(X)4}e^{-\kappa y}, \tag{2.66}$$

$$\hat{\psi}_{(X)(2)} = C_{(X)1}e^{ky} + C_{(X)2}e^{-ky} - \frac{H_2}{H_1}C_{(X)3}e^{\kappa y} - \frac{H_2}{H_1}C_{(X)4}e^{-\kappa y}, \tag{2.67}$$

where $X$ indicates the corresponding patch, $X = I, II, III, IV, V$.

With 16 conditions on 20 unknowns, there are 4 undetermined constants. These undetermined constants are accounted for if it is assumed that as $y \to \pm\infty$, the perturbations tend to zero. This means that in $\mathcal{P}_I$, $C_{(I)2} = 0$ and $C_{(I)4} = 0$, and in $\mathcal{P}_V$, $C_{(V)1} = 0$ and $C_{(V)3} = 0$.

The system is now linear with 16 equations and 16 unknowns, and the system can be posed in terms of a generalized eigenvalue problem. If $c$ is the unknown eigenvalue of the problem, the corresponding phase speed, and the vector,

$$\vec{x} = [C_{(I)1}, C_{(I)3}, C_{(II)1}, C_{(II)2}, \ldots, C_{(V)4}], \tag{2.68}$$

is the eigenvector, then the problem can be stated as,

$$A\vec{x} = cB\vec{x}. \tag{2.69}$$

Here $A$ and $B$ are $16 \times 16$ matrices with constant coefficients. This problem can be solved accurately using MATLAB's `eig` command. The efficiency of this model is superior to the shallow water stability analysis because the system is much smaller, and it does not require approximating any derivatives. However, a shortcoming of the model is that it is even more idealized than the RSW model.

The author has explored $n$-patch models for $n = 3 \ldots 7$. The three- and four-patch models were unable to recover the stability details of jets represented by RSW, and the six- and seven-patch models did not introduce any additional details. Thus the author concludes that the five-patch model is sufficiently simple and accurate to describe the previous results in a concise manner.

## 2.2 Stability

Hydrodynamic instabilities are often classified into different categories depending on the primary mechanism from which the instability evolves. This thesis will focus on barotropic and baroclinic instabilities due to their prevalence in the mesoscale of the world's oceans.

### 2.2.1 Barotropic Instability

Barotropic instability is a mechanism through which perturbations extract energy from the kinetic energy associated with horizontal shear of the mean flow. Recall that in a single layer RSW model, the conservation of PV equation is,

$$\frac{\mathrm{D}}{\mathrm{D}t}\left[\frac{\zeta+f}{h}\right]=0. \tag{2.70}$$

Consider a mean zonal flow, $U(y)$ and a flat bottom, $\eta_b=0$, and further assume that the flow is in geostrophic balance,

$$fU=-g\frac{\partial\eta}{\partial y}. \tag{2.71}$$

In order to make mathematical simplifications it is important to determine which parameters are significant and which are small/not significant. This can be done by applying a dimensional analysis to the equations. Begin by non-dimensionalizing the geostrophic balance equation to find the approximate magnitude of $\eta$,

$$\frac{fU_0}{g}U^*=-\frac{\Delta\eta}{L}\frac{\partial\eta^*}{\partial y^*}. \tag{2.72}$$

Assuming that the starred terms are $\sim\mathcal{O}(1)$, then the following relationship exists,

$$\frac{\Delta\eta}{L}\sim\frac{fU_0}{g}. \tag{2.73}$$

For typical mid-latitude mesoscale values,[1]

$$\Delta\eta\sim 10^{-1}\mathrm{m}. \tag{2.74}$$

This is significantly smaller than the mean depth of the fluid (a range typical of the oceans is between 100m and 1km), and so interface displacements can be ignored. This yields what is known as the rigid-lid approximation.

If the interfacial deviations are assumed to be negligible and the vertical velocity is assumed to be nil, then assume that the geostrophic flow is perturbed. The potential vorticity equation may be rewritten as follows,

$$\frac{\mathrm{D}}{\mathrm{D}t}\left[-\frac{dU}{dy}+\frac{\partial v'}{\partial x}-\frac{\partial u'}{\partial y}+f\right]=0. \tag{2.75}$$

[1] $U_0=1\mathrm{m/s}$, $L=10\mathrm{km}$, $g=10\mathrm{m/s}^2$

A perturbation streamfunction can be introduced, $u' = -\frac{\partial \psi}{\partial y}$ and $v' = \frac{\partial \psi}{\partial x}$. The previous equation can be expanded and linearized, yielding,[2]

$$\frac{\partial}{\partial t}\nabla^2\psi + U\frac{\partial}{\partial x}\nabla^2\psi - \frac{d^2U}{dy}\frac{\partial \psi}{\partial x} = 0. \tag{2.76}$$

A normal mode decomposition is applied to the streamfunction, $\psi = \hat{\psi}(y)e^{ik(x-ct)}$, and substituted into the previous equation to yield,

$$(U-c)\left[\frac{d^2\hat{\psi}}{dy^2} - k^2\hat{\psi}\right] - \hat{\psi}\frac{d^2U}{dy^2} = 0. \tag{2.77}$$

This is the Rayleigh equation. Two important criterion are deduced from this equation, the first being *Rayleigh's inflection point criterion*, and the second being *Fjørtoft's theorem*. To derive these criterion, the previous equation is multiplied through by the complex conjugate of $\hat{\psi}$, and integrated over $y \in \mathcal{D}$, where $\mathcal{D}$ is the domain.

$$\int_{\mathcal{D}} \hat{\psi}^* \left[\frac{d^2\hat{\psi}}{dy^2} - k^2\hat{\psi}\right] dy - \int_{\mathcal{D}} \frac{|\hat{\psi}|^2}{(c-U)}\frac{d^2U}{dy^2}\, dy = 0, \tag{2.78}$$

$$\text{integrate by parts} \Rightarrow \int_{\mathcal{D}} \left|\frac{d\hat{\psi}}{dy}\right|^2 + k^2|\hat{\psi}|^2\, dy - \int_{\mathcal{D}} \frac{|\hat{\psi}|^2}{c-U}\frac{d^2U}{dy^2}\, dy = 0. \tag{2.79}$$

Rayleigh's criterion states that a necessary condition for instability is that $\frac{d^2U}{dy^2}$ changes sign in the interior (away from any boundary) of the flow. Fjørtoft's theorem, not derived here, states that $(U-U_*)\frac{d^2U}{dy^2}$ must be negative in the flow (where $U_*$ is the value of $U$ at an inflection point of the flow).

### 2.2.2 Baroclinic Instability

Eady and Charney have been credited as giving the first quantifiable models of baroclinic instability [7], [5]. This mechanism of instability is prevalent in mid-latitudes and is responsible for weather patterns in the atmosphere and the oceans, [30]. For baroclinic instability to occur the system requires stratification and strong rotation. Baroclinic instability is classified by perturbations extracting available potential energy (APE) from the background flow that is typically in thermal wind balance, [18].

[2] using $\nabla^2\psi = -\frac{\partial u'}{\partial y} + \frac{\partial v'}{\partial x}$

A two-level configuration that recovers the mechanism of baroclinic instability is that of the Phillips model. In the Phillips model (proposed in 1954 [19] in the context of QG, and modified to a two-layer model in 1978, [8]), each layer has a constant zonal speed: $-U$ in the upper layer and $U$ in the lower layer. Consider the two-layer PV equations for a shallow water system,

$$\frac{\mathrm{D}_i}{\mathrm{D}t}\left[\frac{\zeta_i + f}{h_i}\right] = 0, \qquad i = 1, 2. \tag{2.80}$$

If the interface deformations are relatively small, then the equation can be rewritten,

$$\frac{\mathrm{D}_i}{\mathrm{D}t}\left[\frac{1}{H_i}\left(\zeta_i + f\right)\left(1 - \frac{h_i'}{H_i}\right)\right] \approx 0, \tag{2.81}$$

$$\frac{\mathrm{D}_i}{\mathrm{D}t}\underbrace{\left[f + \zeta_i - f\frac{h_i'}{H_i}\right]}_{q_i} \approx 0, \tag{2.82}$$

where the bracketed term is the QG PV. Following the derivation presented in Vallis, a streamfunction can be introduced by considering the geostrophic balance equations,

$$\left(\vec{f} \times \vec{u}_1\right) = -g\vec{\nabla}\left(h_1' + h_2' + \eta_b\right), \tag{2.83}$$

$$\left(\vec{f} \times \vec{u}_2\right) = -g\vec{\nabla}\left(h_1' + h_2' + \eta_b\right) - g'\vec{\nabla}\left(h_2' + \eta_b\right). \tag{2.84}$$

Note that the prime notation in the layer depths, ($h_n'$ variables), denote perturbations to the mean depths, $h_n$. If streamfunctions of the form $\Psi_1 = g\left(h_1' + h_2' + \eta_b\right)$, $\Psi_2 = g\left(h_1' + h_2' + \eta_b\right) + g'\left(h_2' + \eta_b\right)$ are introduced, then the previous equations reduce to,

$$u_n = -\frac{1}{f}\frac{\partial}{\partial y}\Psi_n, \quad v_n = \frac{1}{f}\frac{\partial}{\partial x}\Psi_n. \tag{2.85}$$

The $h_i'$ terms can be written in terms of the streamfunctions as well,

$$h_1' = \frac{f}{g'}\left(\Psi_1 - \Psi_2\right) + \frac{f}{g}\Psi_1, \quad h_2' = \frac{f}{g'}\left(\Psi_2 - \Psi_1\right) - \eta_b. \tag{2.86}$$

Using the streamfunctions introduced here, the QG PV equations can be rewritten,

$$\frac{\mathrm{D}_1}{\mathrm{D}t}\left[\frac{1}{f}\nabla^2\Psi_1 + \frac{f}{g'H_1}\left(\Psi_2 - \Psi_1\right) + \frac{f}{gH_1}\Psi_1\right] = 0, \tag{2.87a}$$

$$\frac{\mathrm{D}_2}{\mathrm{D}t}\left[\frac{1}{f}\nabla^2\Psi_2 + \frac{f}{g'H_2}\left(\Psi_1 - \Psi_2\right) + \frac{f}{H_2}\eta_b\right] = 0. \tag{2.87b}$$

In the case of a flat bottom with a rigid lid, the equations are simpler,

$$\frac{\mathrm{D}_n}{\mathrm{D}t}\left[\frac{1}{f}\nabla^2\Psi_n + (-1)^{n+1}\frac{f}{g'H_n}\left(\Psi_2 - \Psi_1\right)\right] = 0, \quad n = 1, 2. \tag{2.88}$$

A basic state of $\Psi_{0n} = (-1)^n fUy$ is introduced and a perturbation, $\psi_n'$, is superimposed. A doubly periodic domain, and a decomposition of the form $\psi_i' = \mathrm{Re}\left\{\hat{\psi}_i e^{ikx+ily-i\sigma t}\right\}$ are assumed. This yields two linear equations in $\hat{\psi}_i$,

$$\left(K^2\sigma + \frac{\sigma f + Uk}{g'H_1} - \frac{Uk}{f}K^2\right)\hat{\psi}_1 + \left(\frac{Uk - \sigma f}{g'H_1}\right)\hat{\psi}_2 = 0, \tag{2.89}$$

$$\left(\frac{-Uk - \sigma f}{g'H_2}\right)\hat{\psi}_1 + \left(K^2\sigma + \frac{\sigma f - kU}{g'H_2} + \frac{Uk}{f}K^2\right)\hat{\psi}_2 = 0, \tag{2.90}$$

where $K^2 = k^2 + l^2$. For nontrivial solutions to $\hat{\psi}_i$, the determinant must be identically zero. The solutions to this equation yield a relationship for $\sigma$ in terms of the parameters and wavenumbers. Assuming that $H_1 = H_2 = H$ for simplicity, the solution for $\sigma$ becomes,

$$\sigma = \pm\frac{Uk}{2f^2 + K^2g'H}\left[\sqrt{K^4g'^2H^2 - 4f^4}\right]. \tag{2.91}$$

For this simple model of baroclinic instability, there are a few interesting results:

- There exists an unstable wavenumber for any valid parameter values of $H_i$, $g'$, $f$.
- There is no low-wavenumber cutoff, but there is a high-wavenumber cutoff at:

$$K^2 = \frac{2f^2}{g'H}. \tag{2.92}$$

- As found by Eady, the largest growth rates occur for the gravest meridional wavenumber (i.e., $\mathrm{Im}(\sigma)$ is largest when $l = 0$).

### Comparing to the Continuously Stratified Case

The Phillips model is a useful model that describes baroclinic instability, but it assumes specific velocity profiles and does not give general conditions for stratified flows. The

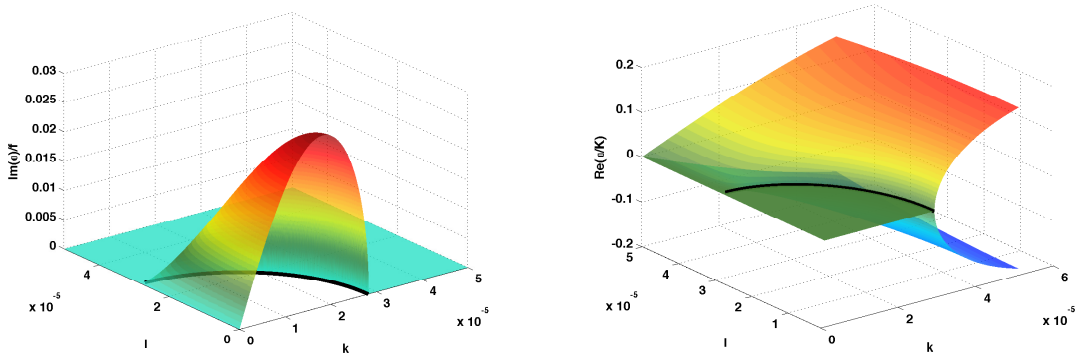


Figure 2.4: Left: growth rates, and right: phase speeds, of the Phillips model of baroclinic instability. The black line represents the short-wave (high wavenumber) cutoff. Parameters used: $U = 0.25\text{m} \cdot \text{s}^{-1}$, $f = 10^{-4}\text{s}^{-1}$, $g' = 10^{-1}\text{m} \cdot \text{s}^{-2}$, $H = 250\text{m}$.

Charney-Stern-Pedlosky criterion for baroclinic instability addresses this issue by considering an arbitrary zonal flow $U(y, z)$ in a continuously stratified fluid. The derivation is similar to deriving the conditions on barotropic instability. The details are not presented here but can be found in [17]. The statement where the Charney-Stern-Pedlosky criterion comes from is:

$$-\text{Im}(c) \int_{y_1}^{y_2} \left\{ \int_0^H \frac{\partial Q}{\partial y} \frac{|\hat{\psi}|^2}{|U-c|^2}\, dz + \left[ \frac{f^2}{N^2} \frac{\partial U}{\partial z} \frac{|\hat{\psi}|^2}{|U-c|^2} \right]_0^H \right\} dy = 0, \tag{2.93}$$

where,

$$Q = -\frac{\partial U}{\partial y} + \frac{\partial}{\partial z}\left[\frac{f^2}{N^2}\frac{\partial \psi_0}{\partial z}\right], \quad \psi = \psi_0 + \text{Re}\left(\hat{\psi}(y,z)e^{ik(x-ct)}\right), \quad \text{and} \quad U = -\frac{\partial \psi_0}{\partial y}. \tag{2.94}$$

In order for this equality to hold, one of the following criteria must be true,

1. $\frac{\partial Q}{\partial y}$ changes sign in the interior.
2. $\frac{\partial Q}{\partial y}$ is the opposite sign to $\frac{\partial U}{\partial z}$ at the upper boundary, $z = H$.
3. $\frac{\partial Q}{\partial y}$ is the same sign as $\frac{\partial U}{\partial z}$ at the lower boundary, $z = 0$.
4. $\frac{\partial U}{\partial z}$ is the same sign at the upper and lower boundaries (applicable when $Q_y = 0$).

To approximate the Phillips model in the continuously stratified regime, assume that the velocity profile is linear in $z$ and independent of $y$, and the Brünt Väisälä frequency, $N(z)$, is constant. This is the *Eady* profile and it satisfies criteria 4 of the Charney-Stern-Pedlosky criteria for baroclinic instability, and therefore, the Eady problem could be baroclinically unstable.

In terms of the Phillips problem, it is seen that $\frac{\partial U}{\partial z} = 0$ at the upper and lower boundaries, and $\frac{\partial Q}{\partial y} = 0$ everywhere (because $U$ is constant). This is seen to clearly satisfy the Charney-Stern-Pedlosky criterion in equation (2.93).

### 2.2.3 Stability of Two-Layer RSW Jets

In the previous two sections simple setups which describe the basic properties of barotropic and baroclinic instabilities have been considered. Now consider a different case: a purely zonal flow in a channel, represented using the two-layer RSW model. The channel walls impose no-normal flow conditions on $v_i$.

Given a basic state zonal velocity $U_i(y)$, the $H_i(y)$ variables are determined by solving the geostrophic balance equations,

$$fU_1 = -g\frac{\partial}{\partial y}\left[H_1(y) + H_2(y) + \eta_b(y)\right], \tag{2.95}$$

$$fU_2 = -g\frac{\partial}{\partial y}\left[H_1(y) + H_2(y) + \eta_b(y)\right] - g'\frac{\partial}{\partial y}\left[H_2(y) + \eta_b(y)\right]. \tag{2.96}$$

Consider a mean flow and its perturbations,

$$u_i(x, y, t) = U_i(y) + u_i'(x, y, t), \tag{2.97}$$

$$v_i(x, y, t) = v_i'(x, y, t), \tag{2.98}$$

$$h_i(x, y, t) = H_i(y) + h_i'(x, y, t). \tag{2.99}$$

Substituting this decomposition into the general equations and linearizing yields the fol-

lowing:

$$\frac{\partial u_1'}{\partial t} = -U_1\frac{\partial u_1'}{\partial x} - v_1'\frac{dU_1}{dy} + fv_1' - g\frac{\partial}{\partial x}\left[h_1' + h_2'\right], \tag{2.100}$$

$$\frac{\partial v_1'}{\partial t} = -U_1\frac{\partial v_1'}{\partial x} - fu_1' - g\frac{\partial}{\partial y}\left[h_1' + h_2'\right], \tag{2.101}$$

$$\frac{\partial h_1'}{\partial t} = -H_1\frac{\partial u_1'}{\partial x} - U_1\frac{\partial h_1'}{\partial x} - H_1\frac{\partial v_1'}{\partial y} - v_1'\frac{dH_1}{dy}, \tag{2.102}$$

$$\frac{\partial u_2'}{\partial t} = -U_2\frac{\partial u_2'}{\partial x} - v_2'\frac{dU_2}{dy} + fv_2' - \frac{\rho_1}{\rho_2}\frac{\partial}{\partial x}\left[g\left(h_1' + h_2'\right) + g'h_2'\right], \tag{2.103}$$

$$\frac{\partial v_2'}{\partial t} = -U_2\frac{\partial v_2'}{\partial x} - fu_2' - \frac{\rho_1}{\rho_2}\frac{\partial}{\partial y}\left[g\left(h_1' + h_2'\right) + g'h_2'\right], \tag{2.104}$$

$$\frac{\partial h_2'}{\partial t} = -H_2\frac{\partial u_2'}{\partial x} - U_2\frac{\partial h_2'}{\partial x} - H_2\frac{\partial v_2'}{\partial y} - v_2'\frac{dH_2}{dy}. \tag{2.105}$$

Note here that the above equations no longer explicitly depend on the topographic variable, $\eta_b$. Instead, the effect of topography is encapsulated in the basic state parameters, $U_i$ and $H_i$.

Assume a normal mode decomposition for the perturbation fields,

$$u_i'(x,y,t) = \mathrm{Re}\left(\hat{u}_i(y)e^{ik(x-ct)}\right), \tag{2.106}$$

$$v_i'(x,y,t) = \mathrm{Re}\left(ik\hat{v}_i(y)e^{ik(x-ct)}\right), \tag{2.107}$$

$$h_i'(x,y,t) = \mathrm{Re}\left(\hat{h}_i(y)e^{ik(x-ct)}\right). \tag{2.108}$$

This decomposition is substituted into the previous system of equations,

$$c\hat{u}_1 = U_1\hat{u}_1 + \frac{dU_1}{dy}\hat{v}_1 - f\hat{v}_1 + g\hat{h}_1 + g\hat{h}_2, \tag{2.109}$$

$$c\hat{v}_1 = -\frac{f}{k^2}\hat{u}_1 + U_1\hat{v}_1 - \frac{g}{k^2}\frac{d}{dy}\hat{h}_1 - \frac{g}{k^2}\frac{d}{dy}\hat{h}_2, \tag{2.110}$$

$$c\hat{h}_1 = H_1\hat{u}_1 + U_1\hat{h}_1 + H_1\frac{d}{dy}\hat{v}_1 + \frac{dH_1}{dy}\hat{v}_1, \tag{2.111}$$

$$c\hat{u}_2 = U_2\hat{u}_2 + \frac{dU_2}{dy}\hat{v}_2 - f\hat{v}_2 + g\frac{\rho_1}{\rho_2}\hat{h}_1 + g\frac{\rho_1}{\rho_2}\hat{h}_2 + g'\frac{\rho_1}{\rho_2}\hat{h}_2, \tag{2.112}$$

$$c\hat{v}_2 = U_2\hat{v}_2 - \frac{f}{k^2}\hat{u}_2 - \frac{g}{k^2}\frac{\rho_1}{\rho_2}\frac{d}{dy}\hat{h}_1 - \frac{g}{k^2}\frac{\rho_1}{\rho_2}\frac{d}{dy}\hat{h}_2 - \frac{g'}{k^2}\frac{\rho_1}{\rho_2}\frac{d}{dy}\hat{h}_2, \tag{2.113}$$

$$c\hat{h}_2 = H_2\hat{u}_2 + U_2\hat{h}_2 + H_2\frac{d}{dy}\hat{v}_2 + \frac{dH_2}{dy}\hat{v}_2. \tag{2.114}$$

This can be written into a linear eigenvalue problem,

$$A\vec{v} = c\vec{v}, \tag{2.115a}$$

where:

$$A = \begin{bmatrix} U_1 & \frac{dU_1}{dy} - f & g & 0 & 0 & g \\ -\frac{f}{k^2} & U_1 & -\frac{g}{k^2}\frac{d}{dy} & 0 & 0 & -\frac{g}{k^2}\frac{d}{dy} \\ H_1 & \frac{dH_1}{dy} + H_1\frac{d}{dy} & U_1 & 0 & 0 & 0 \\ 0 & 0 & g\frac{\rho_1}{\rho_2} & U_2 & \frac{dU_2}{dy} - f & g \\ 0 & 0 & -\frac{g}{k^2}\frac{\rho_1}{\rho_2}\frac{d}{dy} & -\frac{f}{k^2} & U_2 & -\frac{g}{k^2}\frac{d}{dy} \\ 0 & 0 & 0 & H_2 & \frac{dH_2}{dy} + H_2\frac{d}{dy} & U_2 \end{bmatrix}, \tag{2.115b}$$

$$\vec{v} = \begin{bmatrix} \hat{u}_1 & \hat{v}_1 & \hat{h}_1 & \hat{u}_2 & \hat{v}_2 & \hat{h}_2 \end{bmatrix}^T. \tag{2.115c}$$

The solution of this system is found by determining values of $c$ that permit non-trivial solutions of $\vec{v}$. The eigenvalues of this problem are $c$, the phase speeds, and the eigenfunctions are $\vec{v}$. Note that this is not a simple eigenvalue problem, (as $\vec{v}$ depends on $y$ and $A$ contains the differential operator $\frac{d}{dy}$), and it cannot be solved analytically but it can be approximated numerically.

### 2.2.4 Description of Numerical Methods

In order to get approximate solutions to the eigenvalue problem, (2.115), numerical methods must be introduced. A basic method involves discretizing the $y$ domain and defining a Chebyschev differentiation matrix to approximate $\frac{d}{dy}$, [29]. The problem can then be solved using MATLAB's `eig` command, which returns all of the corresponding eigenvalues and eigenvectors of the problem. There are some problems with this method, namely that the `eig` command is computationally expensive for high-resolutions, and that low-resolutions are susceptible to numerical error. Thus, this method is limited by grid size. An alternate method involves using a high-resolution $y$ grid and a sparse low-order finite difference differentiation matrix to approximate $\frac{d}{dy}$. This setup allows the use of MATLAB's built-in `eigs` iterative sparse eigenproblem solver. Unfortunately, low-order finite difference methods are also susceptible to numerical error and the use of `eigs` requires an initial guess. The numerical method used to approximate solutions to the linear eigenvalue problem combines the above two methods to achieve high-numerical accuracy at a reasonable computational cost. The method is described below:

1. Define a low-resolution Chebyschev grid, $y_C$, and Chebyschev differentiation matrix, $Dy_C$.

2. Define a sparse high-resolution, uniformly-spaced grid, $y_F$, and a sparse second-order finite difference differentiation matrix, $Dy_F$.

3. Build the Chebyschev $A$ matrix and solve the eigenvalue problem using MATLAB's `eig` command.

4. Build the high-resolution sparse $A$ matrix and solve the eigenvalue problem with MATLAB's `eigs` command, using the solutions from the Chebyschev case as the initial guess.

5. Store eigenvalues and eigenvectors.

6. Repeat for the next $k$ value until finished.

The advantage of this method is that the numerical errors inherent in the dense matrix solver are not represented in the sparse solver, and vice-versa. This creates an artificial filter which limits the final results to the physical eigen-solutions.

## 2.3 Numerical Methods for Nonlinear Simulations

Code was developed in Fortran by the author to simulate the evolution of the nonlinear multi-layer shallow water equations. The code uses a spectral collocation method to calculate spatial derivatives and uses the Adams-Bashforth 3rd order method to evolve time. In addition to the spatial and temporal derivative solvers, the code uses a hyperviscosity filter defined by Arbic and Flierl, 2004 [1]. The code supports parallelization through standard MPI protocols.

The explicit equations that are approximated are the nonlinear shallow water momentum transport equations. These equations define new variables, $\mathcal{U}_i = u_i h_i$ and $\mathcal{V}_i = v_i h_i$, denoted as the momentum transport variables. This is done to put the equations in conservative form.

The non-dimensional one-layer equations are stated here,

$$\frac{\partial \mathcal{U}}{\partial t} = -\frac{\partial}{\partial x}\left[\frac{\mathcal{U}^2}{h} + \frac{\mathrm{Bu}}{2\mathrm{Ro}^2}h^2\right] - \frac{\partial}{\partial y}\left[\frac{\mathcal{U}\mathcal{V}}{h}\right] + \frac{\mathcal{V}}{\mathrm{Ro}}, \tag{2.116a}$$

$$\frac{\partial \mathcal{V}}{\partial t} = -\frac{\partial}{\partial x}\left[\frac{\mathcal{U}\mathcal{V}}{h}\right] - \frac{\partial}{\partial y}\left[\frac{\mathcal{V}^2}{h} + \frac{\mathrm{Bu}}{2\mathrm{Ro}^2}h^2\right] - \frac{\mathcal{U}}{\mathrm{Ro}}, \tag{2.116b}$$

$$\frac{\partial h}{\partial t} = -\frac{\partial \mathcal{U}}{\partial x} - \frac{\partial \mathcal{V}}{\partial y}. \tag{2.116c}$$

The non-dimensional two-layer momentum transport equations are also stated for completeness,

$$\frac{\partial \mathcal{U}_1}{\partial t} = -\frac{\partial}{\partial x}\left[\frac{\mathcal{U}_1^2}{h_1} + \frac{\mathrm{Bu}_1}{2\mathrm{Ro}^2}h_1^2\right] - \frac{\partial}{\partial y}\left[\frac{\mathcal{U}_1\mathcal{V}_1}{h_1}\right] + \frac{\mathcal{V}_1}{\mathrm{Ro}} - \frac{\mathrm{Bu}_2}{\mathrm{Ro}^2}h_1\frac{\partial h_2}{\partial x}, \tag{2.117a}$$

$$\frac{\partial \mathcal{V}_1}{\partial t} = -\frac{\partial}{\partial x}\left[\frac{\mathcal{U}_1\mathcal{V}_1}{h_1}\right] - \frac{\partial}{\partial y}\left[\frac{\mathcal{V}_1^2}{h_1} + \frac{\mathrm{Bu}_1}{2\mathrm{Ro}^2}h_1^2\right] - \frac{\mathcal{U}_1}{\mathrm{Ro}} - \frac{\mathrm{Bu}_2}{\mathrm{Ro}^2}h_1\frac{\partial h_2}{\partial y}, \tag{2.117b}$$

$$\frac{\partial h_1}{\partial t} = -\frac{\partial \mathcal{U}_1}{\partial x} - \frac{\partial \mathcal{V}_1}{\partial y}, \tag{2.117c}$$

$$\frac{\partial \mathcal{U}_2}{\partial t} = -\frac{\partial}{\partial x}\left[\frac{\mathcal{U}_2^2}{h_2} + \frac{\mathrm{Bu}_2}{2\mathrm{Ro}^2}h_2^2\right] - \frac{\partial}{\partial y}\left[\frac{\mathcal{U}_2\mathcal{V}_2}{h_2}\right] + \frac{\mathcal{V}_2}{\mathrm{Ro}} - \frac{\rho_1}{\rho_2}\frac{\mathrm{Bu}_1}{\mathrm{Ro}^2}h_2\frac{\partial h_1}{\partial x}, \tag{2.117d}$$

$$\frac{\partial \mathcal{V}_2}{\partial t} = -\frac{\partial}{\partial x}\left[\frac{\mathcal{U}_2\mathcal{V}_2}{h_2}\right] - \frac{\partial}{\partial y}\left[\frac{\mathcal{V}_2^2}{h_2} + \frac{\mathrm{Bu}_2}{2\mathrm{Ro}^2}h_2^2\right] - \frac{\mathcal{U}_2}{\mathrm{Ro}} - \frac{\rho_1}{\rho_2}\frac{\mathrm{Bu}_1}{\mathrm{Ro}^2}h_2\frac{\partial h_1}{\partial y}, \tag{2.117e}$$

$$\frac{\partial h_2}{\partial t} = -\frac{\partial \mathcal{U}_2}{\partial x} - \frac{\partial \mathcal{V}_2}{\partial y}. \tag{2.117f}$$

Here, the zonal and meridional variables ($x$ and $y$, respectively) have been scaled by the meridional domain scale, $L_y$, and $\mathcal{U}_i, \mathcal{V}_i$ are scaled by $U_0 H_i$, where $U_0$ is a specified velocity scale (usually determined from the initial conditions), and $H_i$ is the mean depth of layer $i$. The non-dimensional variables $\mathrm{Bu}_i$ and Ro are defined as,

$$\mathrm{Bu}_i = \frac{gH_i}{f_0^2 L_y^2}, \qquad Ro = \frac{U_0}{f_0 L_y}. \tag{2.118}$$

It is important to note that the code used here merely simulates the nonlinear equations, and is itself not *fully* nonlinear. The nonlinear terms of the momentum transport equations cause interactions between all wavenumbers in the domain. In the code used here, the domain and wavenumbers are finitely discretized, and so there are large wavenumbers (corresponding to small length scales) which are not accounted for in the nonlinear simulations. Thus, the code can only approximate the full nonlinearity of the equations.

### 2.3.1 Time-Stepping

The Adams-Bashforth 3rd order (AB3) explicit time-stepping method is used to integrate the momentum transport equations. For an arbitrary differential equation,

$$\frac{d\phi}{dt} = f(\phi, t), \tag{2.119}$$

if the temporal domain is discretized in the standard way ($t_n = t_0 + n\Delta t$), using standard notation ($\Phi$ is the discretized approximation of the continuous variable $\phi$, and $\Phi^n = \Phi|_{t=t_n}$), the AB3 method can be written explicitly as,

$$\Phi^{n+1} = \Phi^n + \frac{\Delta t}{12}\left(5f(\Phi^{n-2}, t_{n-2}) - 16f(\Phi^{n-1}, t_{n-1}) + 23f(\Phi^n, t_n)\right). \tag{2.120}$$

The initial steps are computed using a low-order forward-Euler step followed by the Adams-Bashforth 2nd order,

$$\Phi^1 = \Phi^0 + \Delta t f(\Phi^0, t_0), \tag{2.121}$$

$$\Phi^2 = \Phi^1 + \frac{\Delta t}{2}\left(-f(\Phi^0, t_0) + 3f(\Phi^1, t_1)\right). \tag{2.122}$$

The primary advantage of using this explicit method is that the local truncation error is $\mathcal{O}(\Delta t^4)$, and is thus a 3rd-order method.

### 2.3.2 Spatial Derivatives

A standard spectral collocation method is used to determine spatial derivatives and to handle simple boundary conditions of a periodic channel-like domain. Following [29], the standard one-dimensional truncated discrete Fourier transform (DFT) and truncated inverse discrete Fourier transform (IDFT) are used to convert between wave-space and physical space. These transforms can be performed efficiently in a numerical setting using the Fast Fourier transform (FFT) and Inverse Fast Fourier transform (IFFT). The primary advantage of transforming into Fourier space is that computing spatial derivatives in Fourier space simply consists of algebraic multiplication.

Spectral methods are computationally inexpensive for the accuracy provided, and are also easily parallelized. However, these methods are difficult to adapt to non-regular grids, and care must be taken when using spectral methods in nonlinear systems (like the momentum transport form of the shallow water equations).

The code developed by the author implements this spectral differentiation through the use of the FFTW package.

### Boundary Conditions

For the channel-like domain used in this thesis the boundary conditions used are: no normal flow along the walls and Neumann conditions on the zonal velocity and layer depths. Mathematically, this translates to,

$$v_i = 0, \quad \frac{\partial u_i}{\partial y} = 0, \quad \text{and} \quad \frac{\partial h_i}{\partial y} = 0, \quad \text{for } y = \pm L_y/2. \tag{2.123}$$

These simple boundary conditions can be handled using spectral methods by extending the $y$-domain in either an even or an odd way. Figure 2.5 shows a wave decomposition in an oddly- and evenly-extended domain. The channel-like domain is represented by the left-hand portion of both plots. The solid vertical line and the left vertical axis represent the channel walls. Each wave of the decomposition in the oddly extended domain vanishes at the walls, and thus an oddly extended Fourier-transform is well suited for the Dirichlet conditions of the meridional velocity field. Likewise, each wave of the evenly extended decomposition meets the walls of the domain perpendicularly, meaning that the meridional derivative vanishes at the boundaries, and this method is thus well suited for the Neumann conditions of the zonal velocity and layer-depth fields.

The assumption that $\frac{\partial h_i}{\partial y} = 0$ at the boundaries prohibits the existence of neutral Kelvin waves propagating along the channel walls. The nature of Kelvin waves is such that the amplitude of these waves decay exponentially away from boundaries, and thus it is not expected that these waves will influence interior dynamics of the system.

Numerically, this is simple to implement; when calculating the meridional derivatives of a field, the numerical arrays are extended in the correct way and the FFT is applied to the extended array. If the corresponding field has a Dirichlet (Neumann) condition, then only the imaginary (real) parts of the FFT are kept and the derivative is calculated in the usual way. The IFFT is then applied and the field is truncated back to the standard sized domain in physical space.

### Nonlinear Terms

In a standard spectral method for linear partial differential equations (PDEs) the numerical integration is handled entirely in wave-space for purposes of numerical simplicity and efficiency. The nonlinearity of the momentum transport equations complicates this by introducing a term which is the multiplication of two sums in wave-space. Expanding this multiplication would yield $N^2$ terms in Fourier-space and the numerical efficiency would

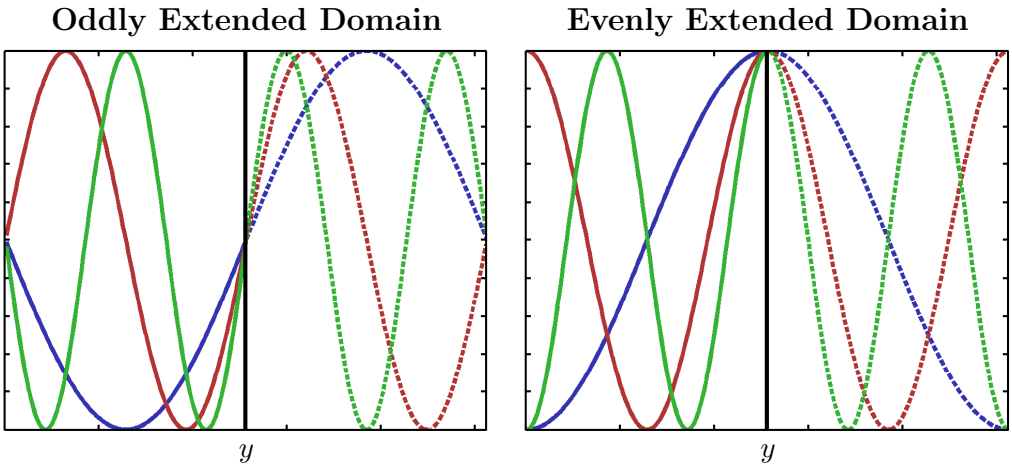


Figure 2.5: Left: a Fourier decomposition consisting of only sine components using an odd extension of the domain. Right: a Fourier decomposition consisting of only cosine components using an even extension of the domain. The solid coloured lines denote physical space, and the dashed lines denote extended space.

be compromised. To avoid this, the spatial derivatives are transformed back to physical space for every time-step, and the time integration is handled completely in physical space. This is known as a collocation method.

### 2.3.3 Hyperviscosity Filter

The filter used in this code is defined in the appendix of [1], and only the result of the derivation will be shown. In general, for a field, $\Phi$, in wave-space with a hyperviscosity term of the form $\nu\vec{\nabla}^{\alpha}\Phi$,

$$\frac{\partial\hat{\Phi}}{\partial t} = \hat{f}(k,l,t) - \nu\left(k^2+l^2\right)^{\alpha}\hat{\Phi}, \tag{2.124}$$

and the numerical integration of this field in the AB3 time-stepping scheme gives,

$$\hat{\Phi}^{n+1} = e^{-\nu(k^2+l^2)^{\alpha}\Delta t}\left[\hat{\Phi}^{n} + \frac{23}{12}\Delta t\hat{f}^{n} - \frac{16}{12}\Delta t\hat{f}^{n-1}e^{-\nu(k^2+l^2)^{\alpha}\Delta t} + \frac{5}{12}\Delta t\hat{f}^{n-2}e^{-2\nu(k^2+l^2)^{\alpha}\Delta t}\right]. \tag{2.125}$$

The results presented in the thesis use values $\alpha = 4$ and $\nu \sim \mathcal{O}(10^{-10})$ for nonlinear simulations.

### 2.3.4 Parameters Used in Nonlinear Numerical Simulations

The nonlinear results shown in this thesis will use similar numerical parameters for each case. In particular, each simulation will be computed on a $256 \times 256$ grid in the $x$ and $y$ directions, respectively. Additionally, time-steps of roughly 30 seconds are used in order to resolve surface gravity waves (which propagate at speed $c = \sqrt{gH}$). The final output time of each simulation varies between $10 - 25$ physical days.

All nonlinear simulations presented here were run on Sharcnet's Orca machines using 32 processors. The run time of each simulation varied, but on average each set of results took approximately 24 hours to compute. Scaling tests were performed using a $64 \times 64$ grid. The efficiency dropped below 70% when using 8 cores. From this it is extrapolated that using a $256 \times 256$ grid is most efficient at 16 cores.

# Chapter 3

# Instabilities of a Mesoscale Jet Without Topography

*Some results of this chapter have been submitted to the* ***Journal of Physical Oceanography*** *in a manuscript co-authored by F.J. Poulin, [10].*

In this chapter the stability characteristics of different flow configurations of a two-layer model will be investigated. The instabilities that are formed will be classified and discussed. The dependence of these instabilities on non-dimensional parameters will be investigated using the RSW model, and then in more detail using the semi-analytic QG model. Finally, the evolution of certain instabilities will be analyzed using a fully nonlinear numerical model.

## 3.1 Description of Cases

For this chapter, the focus will be on determining properties of some oceanographic instabilities that can be represented by two-layer systems. There are four basic configurations that are of interest to this study. For each of these basic states, the two-dimensional parameter space of $Ro$ and $Bu_{BC}$ (to be defined) is varied and explored. The first case is a simple one-layer zonal Bickley jet, and the second case is the two-layer analogue. The third case is a mixed barotropic-baroclinic shear case with zero net transport and the fourth case is a mixed barotropic-baroclinic shear case with net transport. Each case is confined to a

periodic channel-like domain of sufficient meridional span such that the boundaries do not affect the dynamics of the system.

The initial states of each case are calculated from the *geostrophic balance* equations. If $y$ is scaled by the domain width $L_y$, the solution to the one-layer geostrophic balance equations for a zonal Bickley jet are,

$$U(y) = U_0 \text{sech}^2(y/L_j), \quad h_0(y) = H - \frac{fU_0 L_j}{g} \tanh(y/L_j). \tag{3.1}$$

For the two-layer cases,

$$U_1(y) = U_{01} \text{sech}^2(y/L_j), \qquad h_{01}(y) = H_1 + \frac{fL_j}{g}\left(\frac{\rho_2}{\rho_1} U_{02} - U_{01}\right) \tanh(y/L_j), \tag{3.2}$$

$$U_2(y) = U_{02} \text{sech}^2(y/L_j), \qquad h_{02}(y) = H_2 - \frac{\rho_2 f U_{02} L_j}{\rho_1 g} \tanh(y/L_j). \tag{3.3}$$

The rest of this chapter will discuss non-dimensional equations and quantities. The non-dimensional constants are defined in table 3.1.

| Parameter | Definition | Description |
|---|---|---|
| $U_{BT}$ | $\frac{H_1 U_{01} + H_2 U_{02}}{H_1 + H_2}$ | The barotropic zonal velocity |
| $U_{BC}$ | $U_{01} - U_{02}$ | The baroclinic zonal velocity |
| $Ro_{BT}$ | $\frac{U_{BT}}{fL_j}$ | The barotropic Rossby number |
| $Ro_{BC}$ | $\frac{U_{BC}}{fL_j}$ | The baroclinic Rossby number |
| $Bu_{BT}$ | $\frac{g(H_1+H_2)}{f^2 L_j^2}$ | The barotropic Burger number |
| $Bu_{BC}$ | $\frac{g'(H_1+H_2)}{f^2 L_j^2}$ | The baroclinic Burger number |
| $Bu_i$ | $\frac{gH_i}{f^2 L_j^2}$ | The Burger number of layer $i$ |
| $Ro_i$ | $\frac{U_{0i}}{fL_j}$ | The Rossby number of layer $i$ |
| $r_i$ | $\frac{H_i}{H_1+H_2}$ | The ratio of layer depth $i$ to total depth |

Table 3.1: Definitions of basic non-dimensional parameters.

Assuming the domain is scaled by the meridional width, $L_y$, the layer depths $h_i$ are scaled by the mean layer depths, $H_i$, and the layer-wise velocities $(u_i, v_i)$ are scaled by the

maximum magnitude basic state velocity, $U_0$, then the non-dimensional solutions to the two-layer basic states become,

$$u^*_{BT}(y^*) = \frac{Ro_{BT}}{Ro_0}\text{sech}^2\left(L^*_j y^*\right), \tag{3.4}$$

$$h^*_{01}(y^*) = 1 - \frac{r_1 Ro_{BC}Bu_{BC} + Ro_{BC}Bu_{BT} - Ro_{BT}Bu_{BC}}{r_1 Bu^2_{BT}}\tanh\left(Lj^* y^*\right), \tag{3.5}$$

$$u^*_{BC}(y^*) = \frac{Ro_{BC}}{Ro_0}\text{sech}^2\left(L^*_j y^*\right), \tag{3.6}$$

$$h^*_{02}(y^*) = 1 + \frac{r_1 Ro_{BC}Bu_{BC} + r_1 Ro_{BC}Bu_{BT} - Ro_{BT}Bu_{BC} - Ro_{BT}Bu_{BT}}{r_2 Bu^2_{BT}}\tanh\left(Lj^* y^*\right), \tag{3.7}$$

where the $*$ superscripts denote non-dimensional quantities, $Ro_0 = U_0/fL_j$, and $L^*_j = L_y/L_j$.

### One-Layer Barotropic Case

The behaviour of the one-layer barotropic system will be explored over a small range of $Ro$, the Rossby number. A more general study has been conducted that considers a reduced gravity model and explores an additional parameter dependence, Froude number $Fr$, [20]. A thorough investigation of the one-layer case is not the focus of this thesis, and so the analysis will be kept brief. Standard oceanographic parameters will be assumed,

$$Ro = (0.2, 1), \qquad\qquad Bu = 5 \times 10^3. \tag{3.8}$$

This parameter search varies from $Ro = 0.2$, the QG regime, to $Ro = 1$, the intermediate regime. It is referred to as the intermediate regime in literature because it is between the QG ($Ro \ll 1$) and ageostrophic regimes ($Ro \gg 1$). This can be thought of as studying motions that are near the sub-mesoscale.

### Two-Layer Barotropic Shear Case

The two-layer barotropic shear case is similar in nature to the single layer case, however it introduces the potential for baroclinic motions since the flow is stratified. There are now two parameters over which this case is varied: $Ro_{BT}$, representing changes in velocity

scales, and $Bu_{BC}$, representing changes in stratification. The parameter regime is the same as the first case, with the addition of density parameters,

$$Ro_{BT} = (0.2, 1), \qquad Ro_{BC} = 0, \qquad Bu_{BT} = 5 \times 10^3, \qquad Bu_{BC} = (5, 50, 500). \tag{3.9}$$

It is important to note that the *shear* in this case is a purely horizontal shear (as a result of the Bickley jet profile). This differs from other cases where *shear* largely refers to the difference of layer velocities, $U_{01} - U_{02}$, which results in a vertical shear.
The ratio of mean layer depths is of interest to the dynamics of the system, and should not be ignored as a possible parameter regime to explore. However, in the interest of brevity and scope, the author has chosen to keep the individual layer depths equal. See section 3.5 for a brief stability analysis on the effects of modifying the surface layer depth.

#### Mixed Barotropic-Baroclinic Shear with No Net Transport Case

For this case, the barotropic Rossby number is assumed to be nil, and the baroclinic Rossby number is varied. The baroclinic Burger number range is kept the same.

$$Ro_{BT} = 0, \qquad Ro_{BC} = (0.2, 1), \qquad Bu_{BT} = 5 \times 10^3, \qquad Bu_{BC} = (5, 50, 500). \tag{3.10}$$

This case has no net transport because this parameter regime requires that $U_1 = -U_2$ and the jets are equal in size. Hence there is no net volume transport in this basic state.

#### Mixed Barotropic-Baroclinic Shear with Non-Zero Net Transport Case

In this final case, the barotropic Rossby number is kept on the order of the baroclinic Rossby number. The baroclinic Burger number is varied in the same way as before.

$$Ro_{BT} = Ro_{BC} = (0.2, 1), \qquad Bu_{BT} = 5 \times 10^3, \qquad Bu_{BC} = (5, 50, 500). \tag{3.11}$$

This case has a net volume transport because both jets move in the same direction, and hence transport a non-zero volume of fluid.

## 3.2 Linear Stability Results

This section will present the results of the two-layer linear stability analysis code applied to each case. For each flow configuration, growth rates, phase speeds, and modal structures which correspond to growing modes, will be highlighted. The results will be shown in non-dimensional quantities unless otherwise stated.

### 3.2.1 One-Layer Barotropic Cases

Figure 3.1 summarizes the results of the linear stability analysis. As seen in the figure, the differences between the QG and intermediate regime are minor. It is worth noting that all quantities here are non-dimensional, and so the growth rates, phase speeds, and $u$ profiles are all scaled by $Ro$. The primary differences are in the $\eta'$ fields of each modal structure. It can be seen that in the QG regime case, the $\eta'$ structures are largely symmetric about $y = 0$, while in the intermediate regime case, the structures are slightly northern intensified.

The primary unstable mode here is classified as a *sinuous* mode, while the secondary mode is classified as a *varicose* mode. *Sinuous* modes are identified by phase speeds which decrease towards large scales and meridional velocity structures which are symmetric about $y = 0$. *Varicose* modes are identified by phase speeds which tend to increase towards large scales and meridional velocity structures which are anti-symmetric about $y = 0$. These modes will now be shortened in the text as **BTSin** for the barotropic sinuous mode, and **BTVar** for the barotropic varicose mode.

### 3.2.2 Two-Layer Barotropic Shear Case

The parameter space of interest for this case is much larger than the previous case, and only the relevant results will be discussed here. The modal structures of the velocity fields which are shown will be presented in one of two fashions; the first will be a layer-wise decomposition, as is standard for representing modal structures. The second will be a linearized barotropic-baroclinic decomposition which will be calculated as follows,

$$\vec{u}'_{BT} = \frac{H_1\vec{u}'_1 + H_2\vec{u}'_2}{H_1 + H_2}, \qquad \vec{u}'_{BC} = \vec{u}'_1 - \vec{u}'_2. \tag{3.12}$$

These quantities can give an approximate measure of barotropicity or baroclinicity of an instability. The method of choice will be clarified in the caption of each figure of modal structures.

#### Parameter Search: $Ro_{BT}$

The barotropic Rossby number is varied between the QG and intermediate regimes, while the baroclinic Burger number is fixed at 5 - this corresponds to $g' = 0.01m/s^2$ (assuming $fL_j = 1$ and $H_1 + H_2 = 500m$), values typical of weakly stratified regions of the mesoscale

ocean such as the region of the Bransfield current located between the Antarctic Peninsula and the South Shetlands Islands, [22], [24].

Recall that the one-layer barotropic configuration generated two growing modes, BTSin and BTVar. These two modes also appear in the two-layer case, and the growth rates agree to within 0.1%. However, when the jet is weakly stratified, a prominent third mode also appears in both regimes (see figure 3.2). This mode is *sinuous* and *baroclinic* in nature. Hence this mode is now referred to as a *baroclinic sinuous* mode, abbreviated as **BCSin**. The baroclinicity of this mode can be seen in the modal structures in figure 3.3 - the barotropic components of perturbation velocities, $\vec{u}'_{BT}$, are weak, $\mathcal{O}(10^{-5})$, while the baroclinic components of perturbation velocities, $\vec{u}'_{BC}$ are relatively stronger, $\mathcal{O}(10^{-1})$.

The difference between the BTSin and BTVar modes between regimes are not significant. The growth rates tend to the same value and the phase speeds of instability also do not change significantly. The only mode that exhibits dependence on the barotropic Rossby number is the BCSin mode. As the Rossby number is increased from 0.2 to 1, the maximum growth rate of the BCSin mode increases by 23.7%. This implies that as the Rossby number increases, the effects of stratification become more important. The modal structures do not change significantly (see figure 3.3).

When the Rossby number enters the ageostrophic regime the BCSin instability becomes the primary instability and the one-layer model is insufficient in describing the dynamics of the system, [3]. In addition to the BCSin mode becoming dominant, a fourth unstable mode is introduced (around $Ro_{BT} \approx 4$). This unstable mode has a varicose structure in the meridional velocity fields, but has a new type of structure in the zonal velocity fields. This type of instability is known as an inertial instability and is due to the PV changing signs somewhere in the interior of the flow. However, this is beyond the scope of this parameter search, and so it will not be analyzed further. More details may be found in [3].

### Parameter Search: $Bu_{BC}$

The barotropic Rossby number is fixed at $Ro_{BT} = 1$ for these cases, and the baroclinic Burger number, $Bu_{BC}$, varies. The baroclinic Burger number is a measure of reduced gravity at the interior interface. This quantity will be varied between weak stratification ($Bu_{BC} \sim 5$) to very strong stratification ($Bu_{BC} \sim 500$). The intermediate regime is chosen because stratification affects growth rates in a more dramatic sense than in the QG regime.

In figure 3.4, the effects of stratification on growth rates and phase speeds are shown. In the weak stratification case there are only three modes present: BTSin, BCSin and BTVar (as seen before). As the stratification becomes stronger, a weak fourth mode emerges. The

modal structure of this mode is varicose and baroclinic in nature and will be known as BCVar. In the limit of large $Bu_{BC}$ (not shown) the growth rates and phase speeds of the baroclinic modes tend to those of the barotropic modes. The BCSin mode was first studied in [3], but there was no evidence of the BCVar mode because the stratification used was too weak. This investigation is perhaps the first time both of these instabilities have been observed.

### 3.2.3 Mixed Barotropic-Baroclinic Shear with No Net Transport Cases

In this mixed BT-BC shear with no net transport set of results the modal structures will be presented in a *layer-wise* fashion as opposed to the BT-BC decomposition presented previously.

#### Parameter Search: $Ro_{BC}$

In the barotropic case the barotropic Rossby number was varied from the QG regime to the intermediate and ageostrophic regimes while the baroclinic Rossby number remained fixed and nil. In this section the baroclinic Rossby number will be varied across these regimes and the barotropic Rossby number will be fixed and nil. The baroclinic Burger number is fixed in the weakly stratified regime, $Bu_{BC} = 5$.

In figure 3.5, the growth rates and phase speeds of the QG and intermediate regime cases are shown. There are five modes in each case - the BTSin and BTVar modes are of multiplicity two, as each mode appears in both layers. The fifth mode which appears corresponds to the classic Phillips mode, as was seen in section 2.2.2, and will be abbreviated as **BCPhil**. In the two-layer barotropic shear case the resonances were confined into each layer, but in the BCPhil instability, the resonance occurs between layers.

The primary differences between regimes are in the barotropic sinuous modes - both in structure and growth rate. In the QG regime the barotropic modes are more pronounced, but are still much weaker than the BCPhil mode. In the intermediate regime, the BTSin modes become even weaker. The BTVar modes persist in strength between regimes, however the phase speed of this mode increases slightly in the intermediate regime. The modal structures of both sets of barotropic modes are symmetric in magnitude about $y = 0$ in the QG regime, however they become slightly asymmetric in the intermediate regime.

In the case of a mixed BT-BC shear configuration with no net transport, the baroclinic Rossby number has small effects on the growth rates of the barotropic modes and the modal structures of each mode.

**Parameter Search:** $Bu_{BC}$

The Rossby number is fixed in the intermediate regime, $Ro_{BC} = 1$, for these cases. As in the barotropic case, the baroclinic Burger number is varied between weak, strong, and very strong stratification regimes.

In the case of weak stratification (presented in previous sub-section), the BCPhil mode was dominant, with the BTSin and BTVar modes being secondary. Figure 3.7 shows that in the case of strong stratification ($Bu_{BC} = 50$), the BTSin mode becomes dominant and the effect of the BCPhil mode becomes much less prominent. In addition to the BTSin mode becoming stronger, the low-wavenumber cutoff decreases, and the peak of the instability moves to smaller wavenumbers (larger length scales). In the case of very strong stratification ($Bu_{BC} = 500$), the modes tend to those of the barotropic case. There are four modes present in this case, two BTSin modes and two BTVar modes, one set of each corresponding to each layer. Figure 3.8 show the modal structure of each mode. There is a sinuous mode and a varicose mode which is intensified in each layer, and a weak BCPhil mode which is equally strong in both layers.

### 3.2.4 Mixed Barotropic-Baroclinic Shear with Net Transport Cases

This configuration is most characteristic of real oceanographic flows, and is more complicated than the previous configurations. The Rossby numbers are fixed to be equal in this case (which sets the basic profile of each layer),

$$Ro_{BT} = \frac{1}{2}U_1 + \frac{1}{2}U_2 = Ro, \tag{3.13}$$

$$Ro_{BC} = U_1 - U_2 = Ro, \tag{3.14}$$

$$\Rightarrow U_1 = \frac{3}{2}Ro, \quad U_2 = \frac{1}{2}Ro, \quad U_1 = 3U_2. \tag{3.15}$$

Thus, the top layer jet is three times stronger than the lower layer jet, and both jets flow in the same direction.

**Parameter Search:** $Ro_{BT}$ & $Ro_{BC}$

The barotropic and baroclinic Rossby numbers are varied in tandem with each other (so as to keep the same type of configuration). The QG and intermediate regime results are presented in figure 3.9. The primary difference between the QG and intermediate regimes is the shape of the BTSin mode. In the intermediate regime, the BTSin mode develops a second local maxima at large scales. The modal structures are not included here for brevity, but the modal structure of this secondary maxima in the primary mode is the same structure as the primary maxima, just shifted in phase. The structures of the other modes could be classified as sinuous or varicose, but the barotropicity and baroclinicity of the modes are not easily identified and so they are simply classified as mixed modes. Hence only the BTSin mode is labeled in figure 3.9.

**Parameter Search:** $Bu_{BC}$

In this case, the Rossby numbers are fixed in the intermediate regime and the stratification parameter is varied. Figure 3.10 shows the growth rates and phase speeds in the weakly stratified and strongly stratified regimes. The differences here are much more pronounced than in the previous parameter search. In the weakly stratified case, the only mode which can be identified is the surface intensified barotropic sinuous mode. The modal structures are presented in figure 3.11. In the strongly stratified case, the modes (in order of decreasing maximum growth rate) are as follows:

1. BTSin1: the surface-layer intensified barotropic sinuous mode.
2. BTSin2: the bottom-layer intensified barotropic sinuous mode.
3. BTVar1: the surface-layer intensified barotropic varicose mode.
4. BTVar2: the bottom-layer intensified barotropic varicose mode.

It is clear that the coupling effects of the two-layer model are not important in the strongly stratified case, and thus the model decouples well into two one-layer models. When the stratification is strengthened further there are no significant changes and thus the growth rates and phase speeds are not shown.

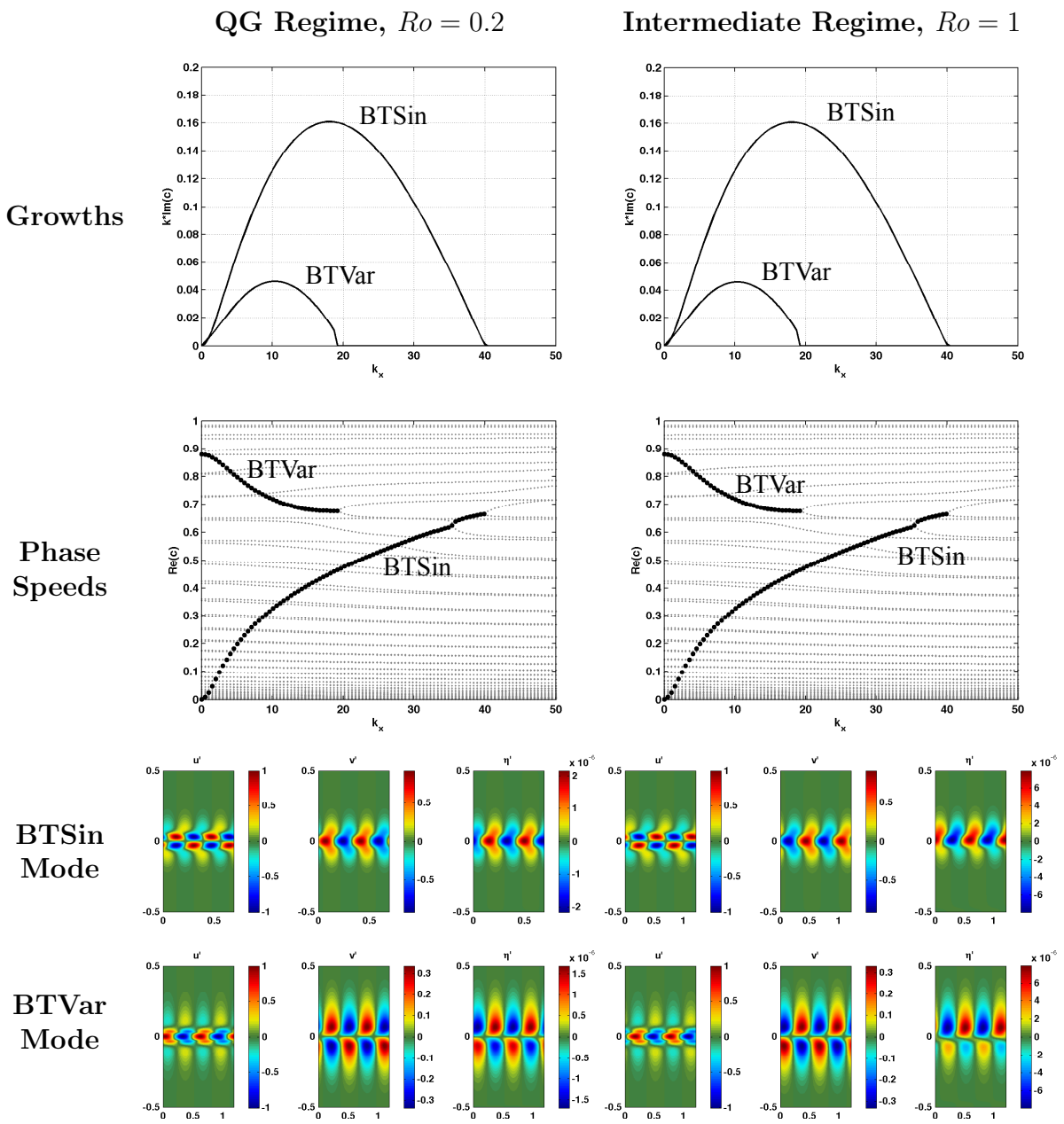


Figure 3.1: Comparing the growth rates, phase speeds, and modal structures of the QG and intermediate regime cases. For the phase speed plots, the black dots are unstable points, while the grey dots are stable points.

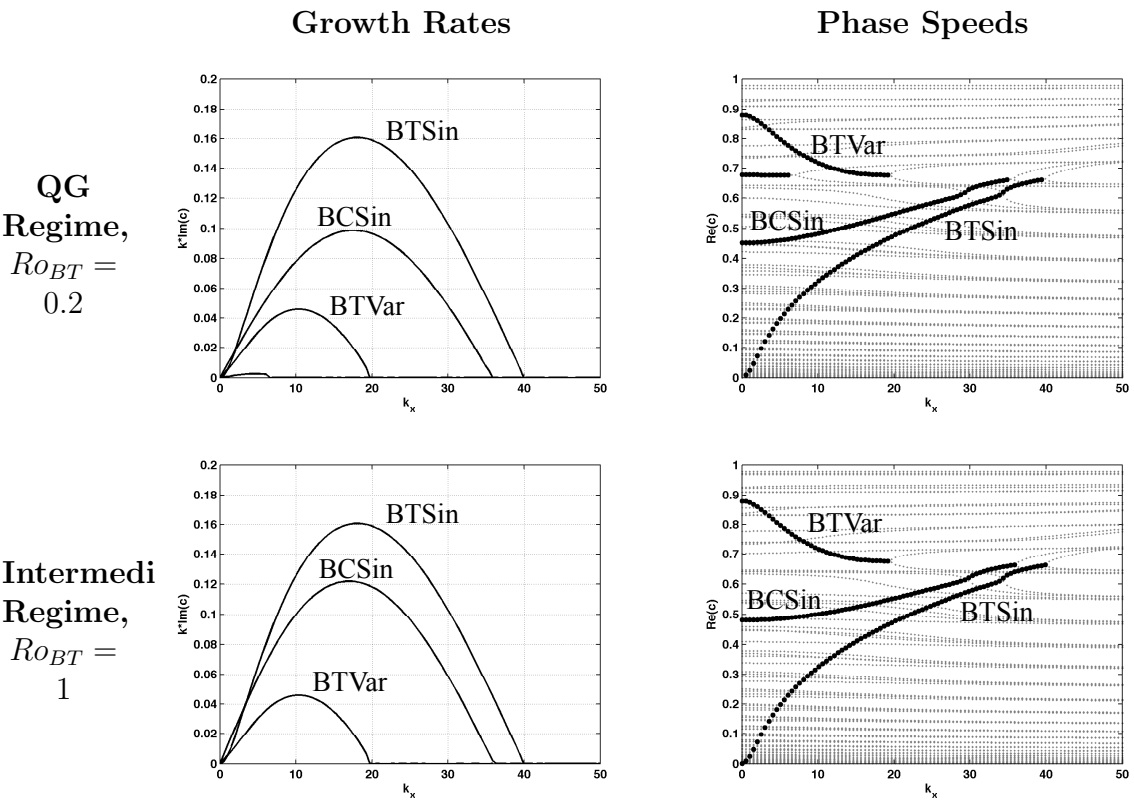


Figure 3.2: The growth rates and phase speeds of the two-layer barotropic shear profile.

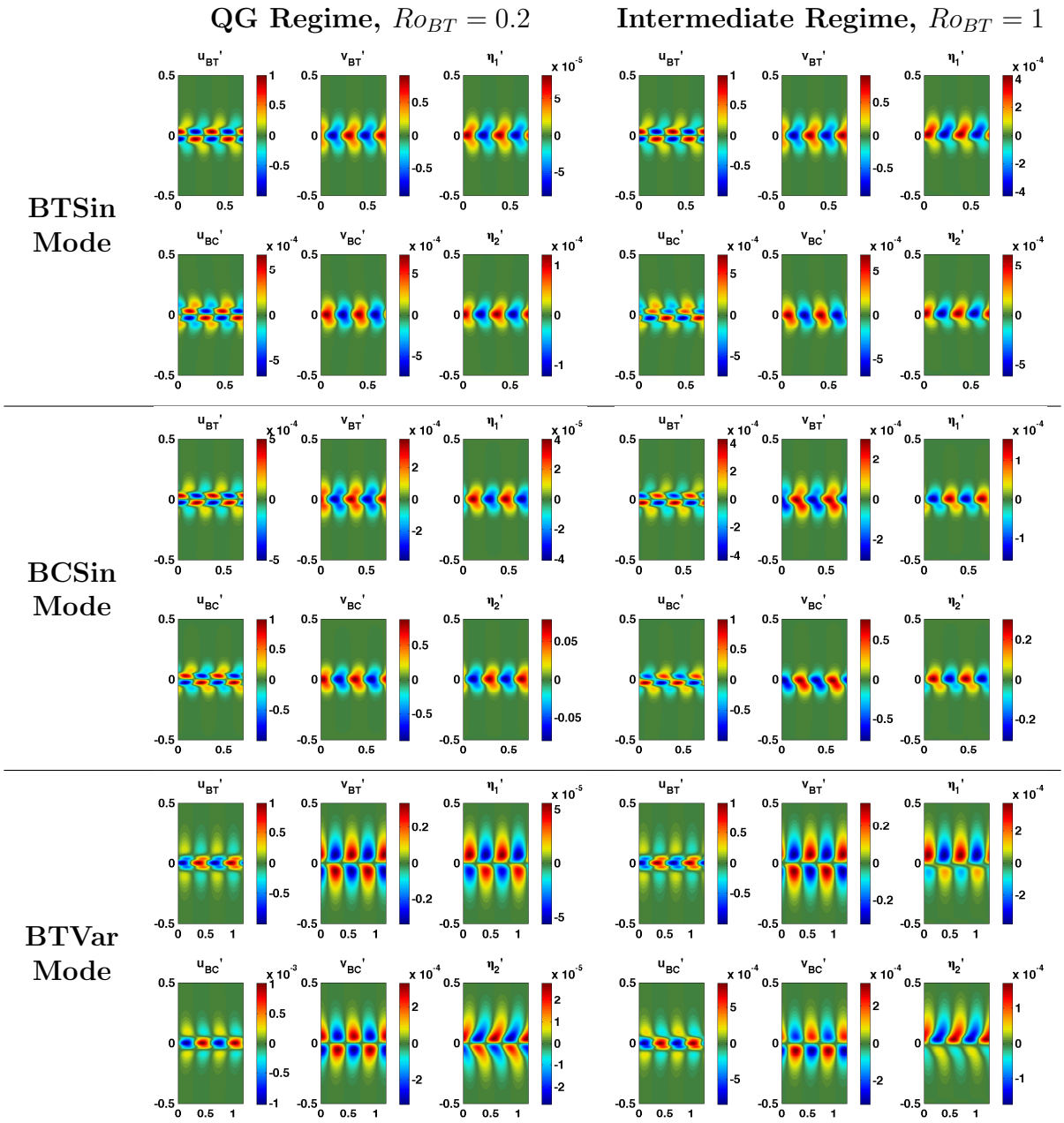


Figure 3.3: The barotropic-baroclinic modal structures of the two-layer barotropic shear profile in the QG and intermediate regimes.

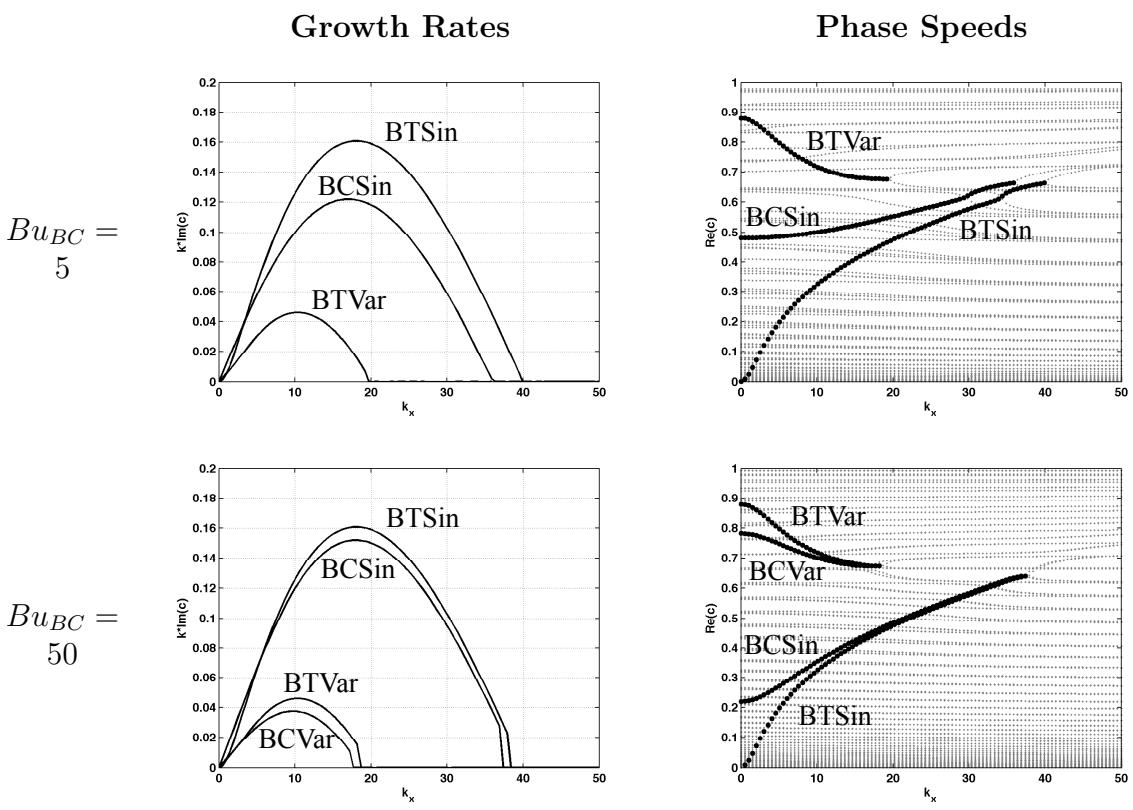


Figure 3.4: The growth rates and phase speeds of the two-layer barotropic shear profile, with weak and strong stratification.

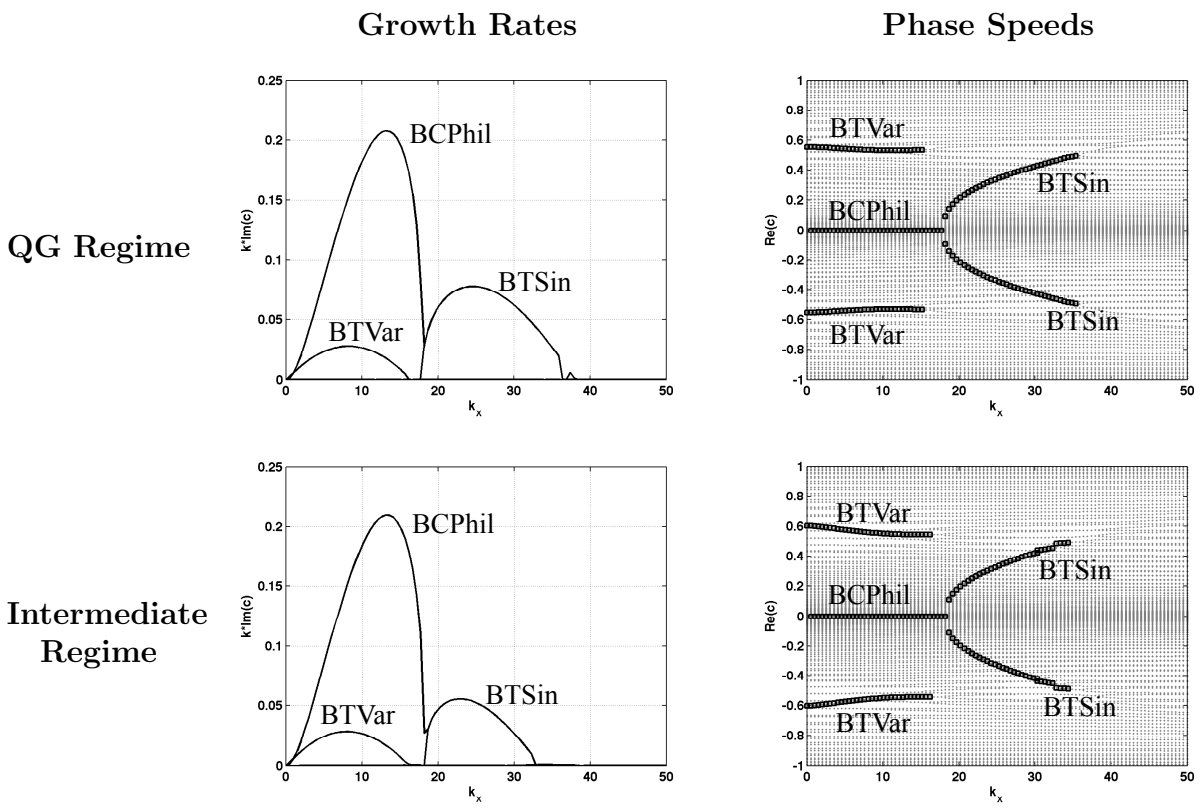


Figure 3.5: The growth rates and phase speeds of the mixed barotropic-baroclinic shear with no transport case, with varying $Ro_{BC}$.

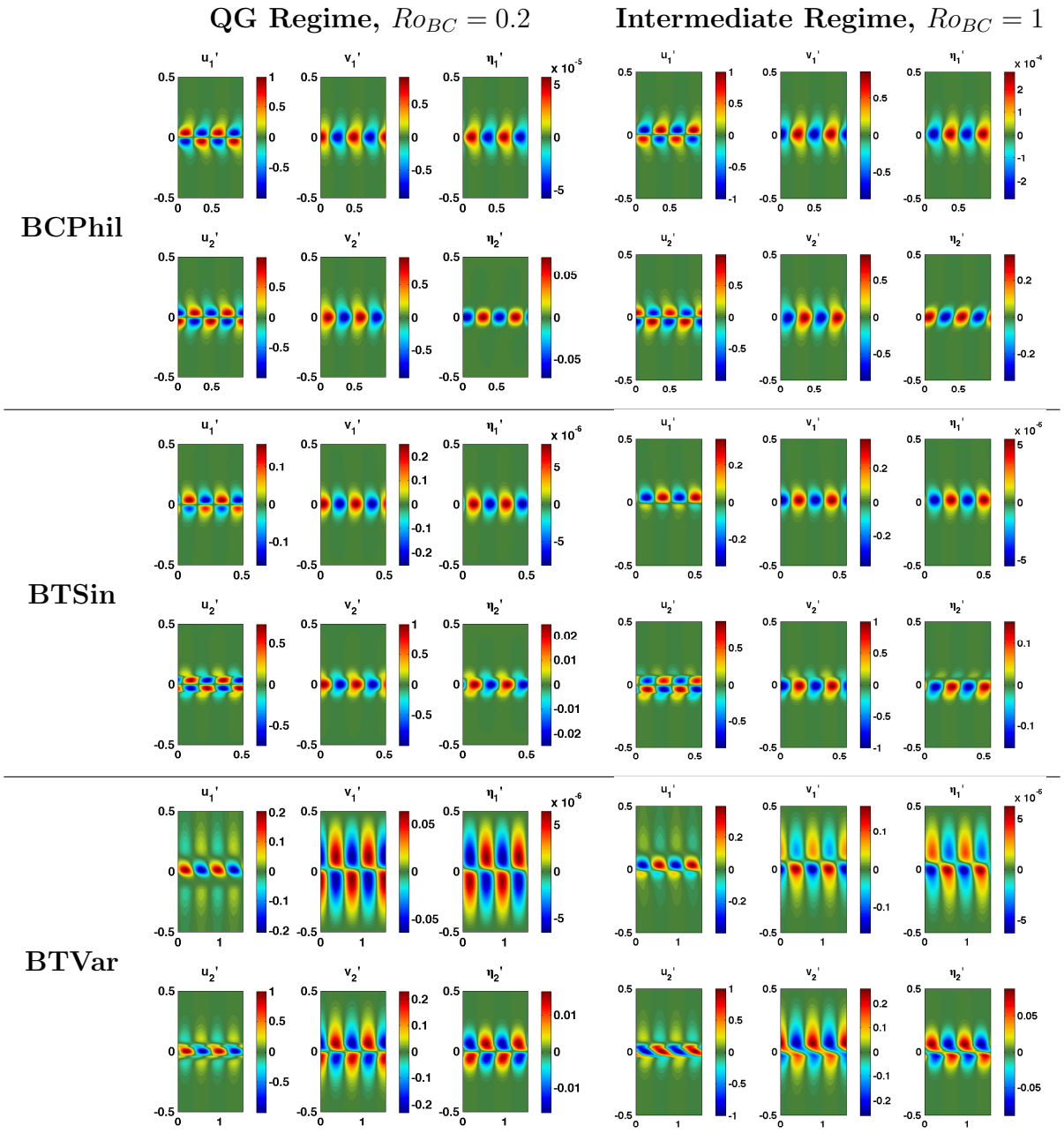


Figure 3.6: The *layer-wise* modal structures of the mixed barotropic-baroclinic with no transport case, with $Ro_{BC} = 0.2$ and $Ro_{BC} = 1$.

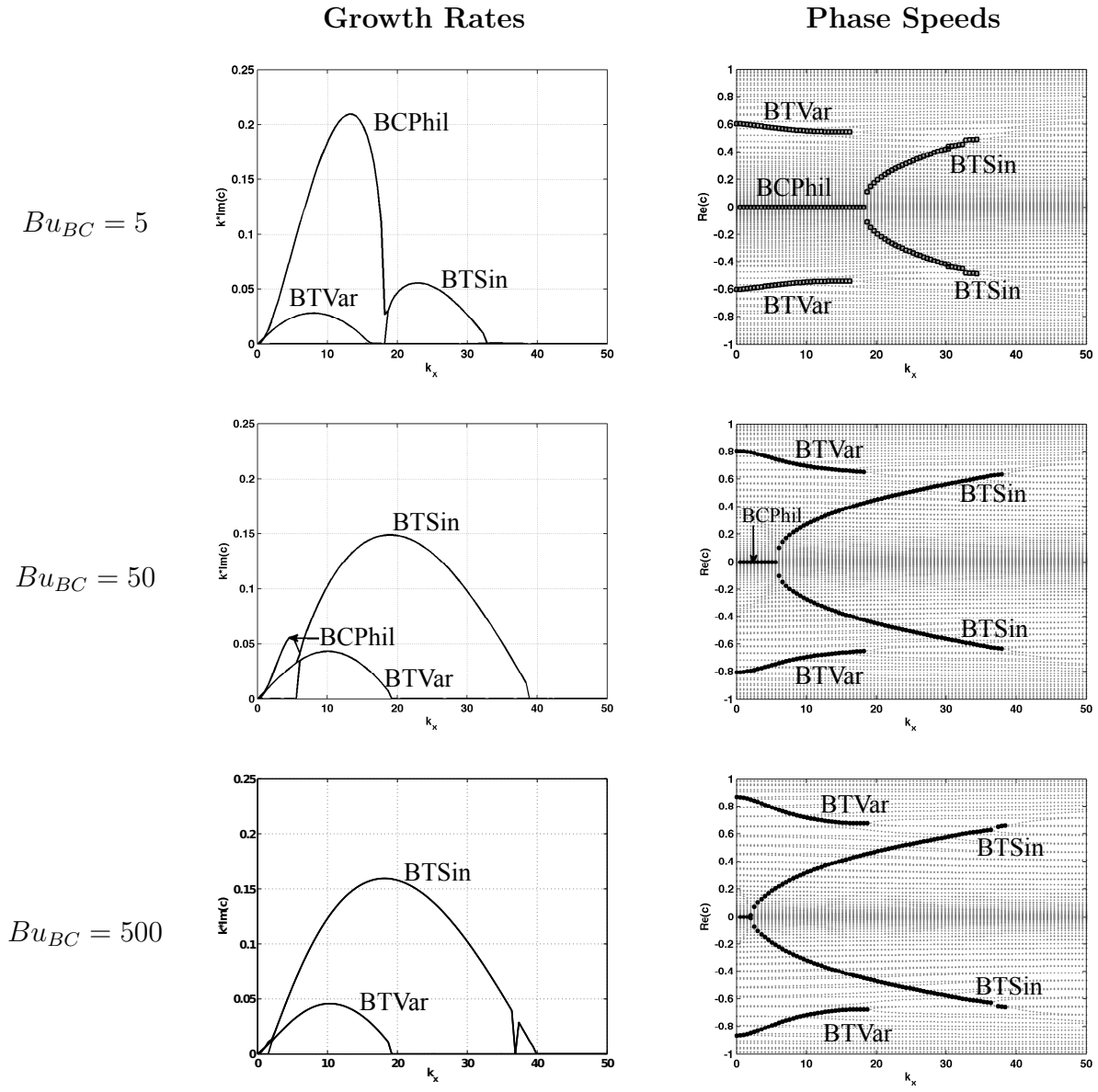


Figure 3.7: Growth rates and phase speeds of weak stratification ($Bu_{BC} = 5$) to very strong stratification ($Bu_{BC} = 500$).

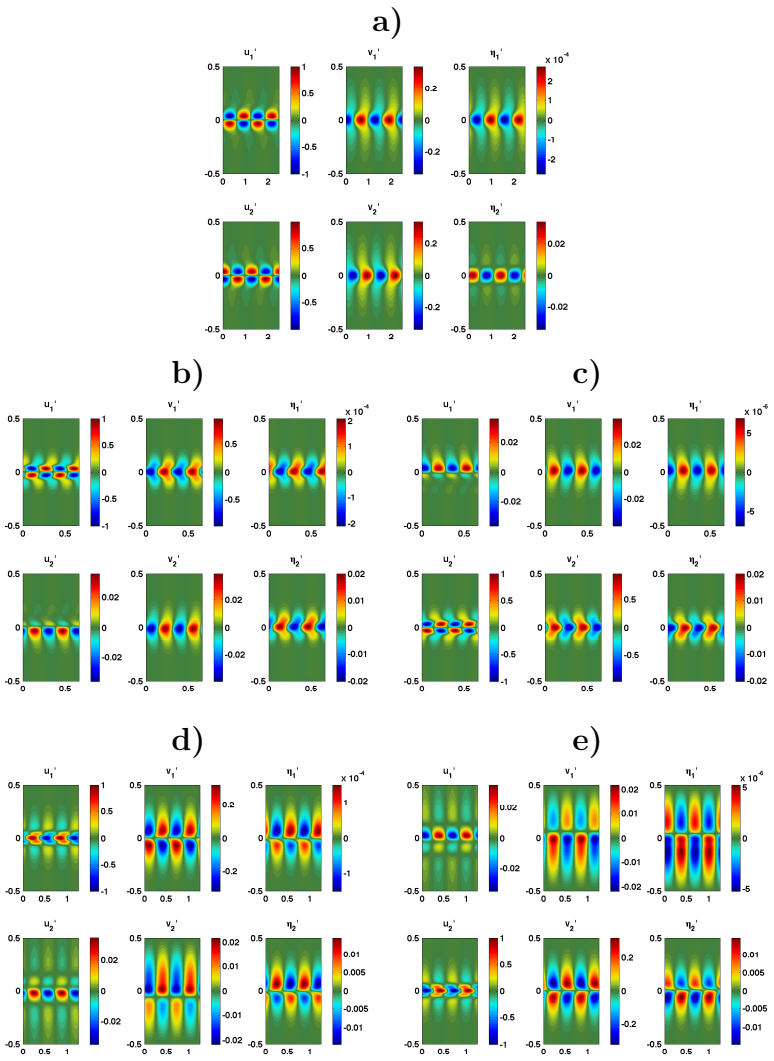


Figure 3.8: The *layer-wise* modal structures of the mixed barotropic-baroclinic shear with no transport case, with $Bu_{BC} = 50$, $Ro_{BT} = 0$, $Ro_{BC} = 1$. **a)** BCPhil mode, **b)** surface-intensified BTSin mode, **c)** bottom-layer intensified BTSin mode, **d)** surface-intensified BTVar mode, **e)** bottom-layer intensified BTVar mode.

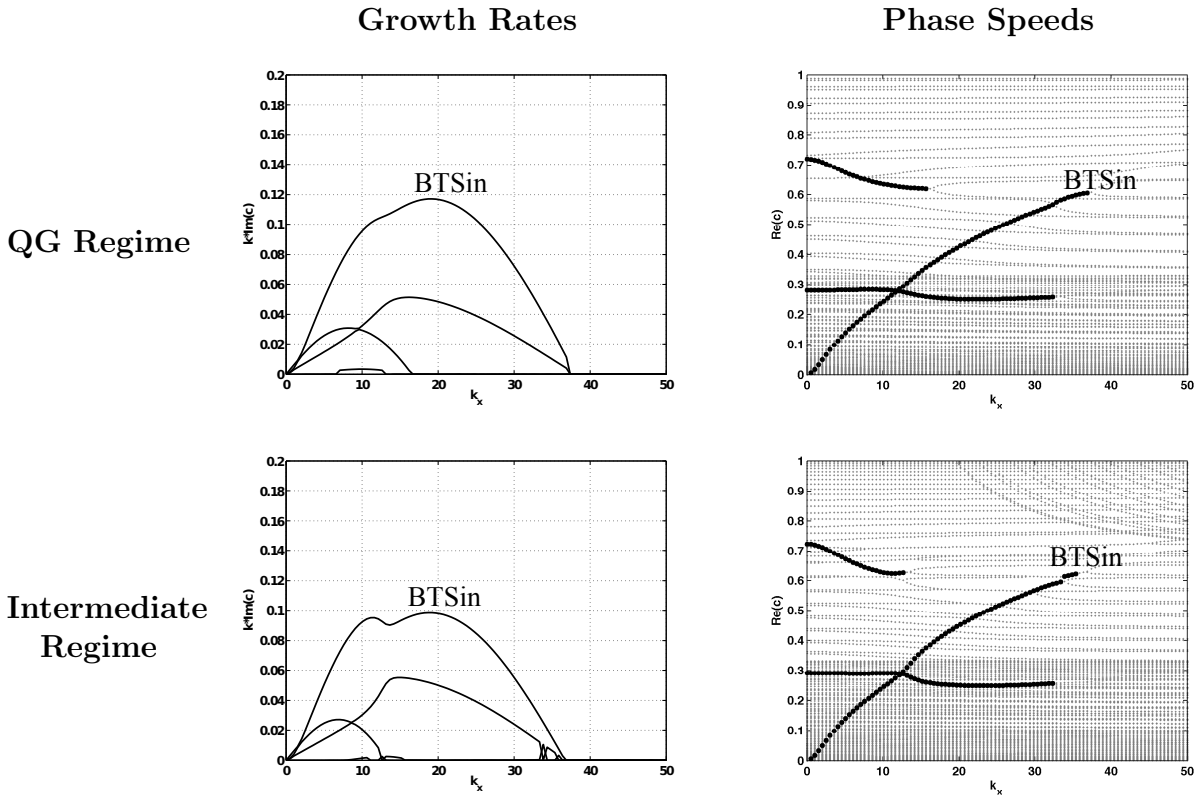


Figure 3.9: Growth rates and phase speeds in the QG ($Ro_{BT} = Ro_{BC} = 0.2$) and intermediate ($Ro_{BT} = Ro_{BC} = 1$) regimes for the mixed barotropic-baroclinic shear with net transport case, and $Bu_{BC} = 5$.

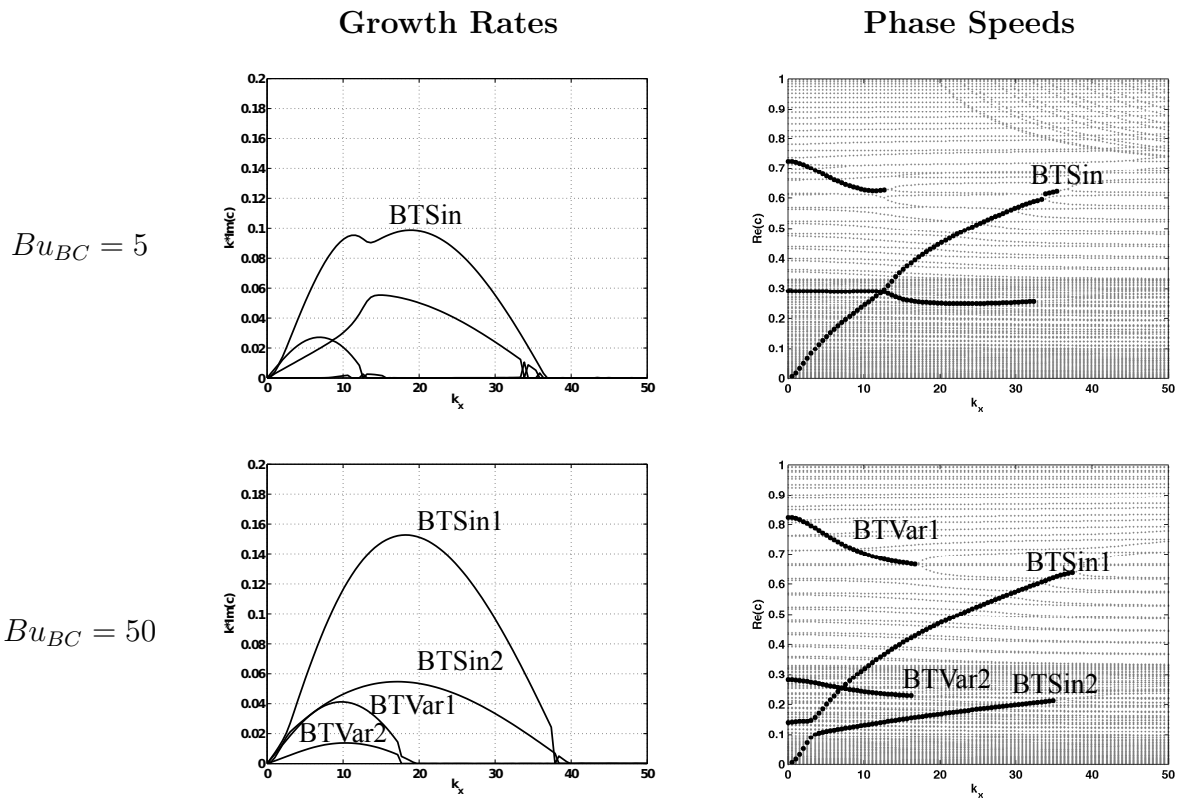


Figure 3.10: Growth rates and phase speeds for the mixed BT-BC shear with net transport case in the intermediate regime, $Ro_{BT} = Ro_{BC} = 1$, varying stratification.

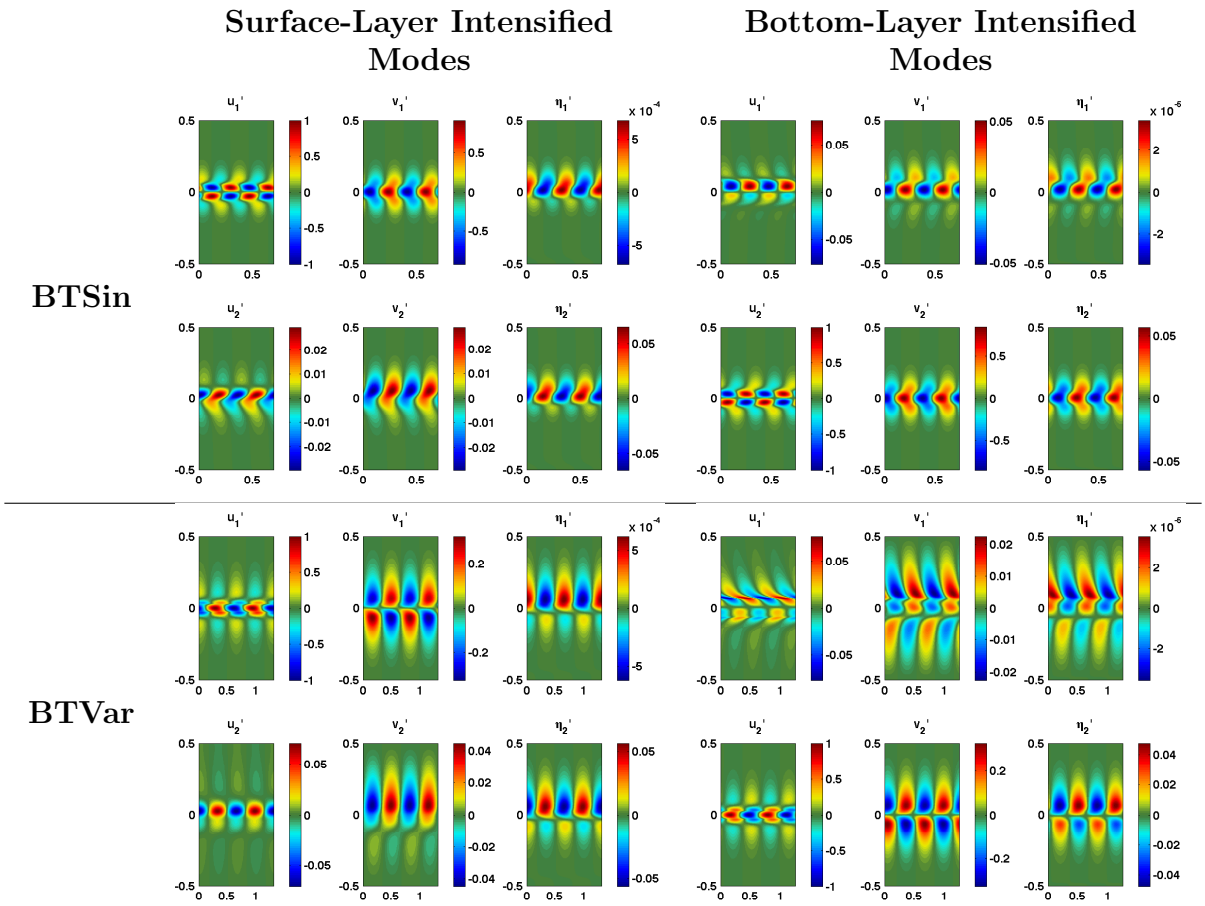


Figure 3.11: The *layer-wise* modal structures for the strongly stratified, $Bu_{BC} = 50$, mixed BT-BC shear with net transport case, in the intermediate regime, $Ro_{BT} = Ro_{BC} = 1$. The top-left plot is the BTSin1 mode, top-right is the BTSin2 mode, bottom-left is the BTVar1 mode, and bottom-right is the BTVar2 mode.

## 3.3 Semi-Analytic Quasi-Geostrophic Model Cases

The previous analysis allowed the consideration of a small set of test cases for each configuration. Due to the computational costs required for numerical accuracy, the exploration of parameter space was limited. The semi-analytic QG model is computationally more efficient than the linear RSW model, and thus it allows for a much broader search of parameter space. Despite the QG model not describing the intermediate regime as accurately, it will be shown that it gives a qualitative representation of how unstable modes vary in parameter space. The effects of modifying $Ro_i$ and $Bu_{BC}$ will be visualized in a continuous manner in this section.

### Verifying the Model

In section 2.1.3, the semi-analytic model was introduced. In this section, the validity of the model will be confirmed by comparing the results of the RSW analysis to the results produced by this model.

In figure 3.13 the growth rates and phase speeds of the models are compared for the intermediate regime cases. In general, the QG model overestimates the growth rates, underestimates the phase speeds, and tends to estimate larger scales of instability. However, individual modes are represented in both models and the modal structures (not shown) agree surprisingly well. The results compare more accurately with cases of stronger stratification because the basic state interface deformations are smaller (one of the assumptions in deriving the QG equations).

Recall that the QG model introduced in 2.1.3 divides the meridional domain into $n$ strips, denoted as "patches". It is important to note here that there are two free parameters which have been chosen by the author, namely the half-width of the patched jet, $Lj_{patch}$ and the break point of the jets, $\alpha$. For these cases values of $Lj_{patch} = 1.5L_j$ and $\alpha = 0.2$ were chosen to represent the profiles of the continuous case accurately.

The parameter $\alpha = 0.2$ was chosen by considering the limiting cases of $\alpha$, and then testing by trial and error. If $\alpha \to 0$ then the 5-patch model tends to the results of the 4-patch model and some modes are lost. If $\alpha \to 1$ then the results tend to a 3-patch model and some modes are lost. Thus an intermediate value of $\alpha = 0.2$ is chosen to recover all relevant modes while still retaining a jet structure similar to that of the continuous Bickley jet.

The choice of $Lj_{patch} = 1.5L_j$ was determined in a similar fashion. If $Lj_{patch} \to L_j$, the relative width of the patch jet is very skinny compared to the continuous jet and the

instabilities are much stronger than the shallow water case (although the length scales are more comparable). If $Lj_{patch} \to 2L_j$ then the patched jet is relatively thick compared to the continuous jet and the scales of instability are much larger (although the growth rates are more comparable). A value of $Lj_{patch} = 1.5L_j$ was chosen to achieve the maximal growth rates with good accuracy and to approximate relative length scales with fair accuracy.

In summary, the semi-analytic QG model resolves the number of modes, relative growth rates of each mode, and modal structures well, while it does not quantify growth rates, phase speeds or length scales exactly.

### 3.3.1 The Effects of $Ro$ and $Bu_{BC}$

In this section, the QG model will be used to investigate how continuously modifying $Ro_{BT}$ and $Ro_{BC}$ (more specifically, modifying $U_{02}$ while holding $U_{01}$ fixed) affects the maximum growth rates, number of modes, layer-wise phase shifts (to be defined), and phase speeds of modes. This analysis will be applied to three regimes of stratification: weakly stratified (corresponding to $Bu_{BC} = 5$), strongly stratified (corresponding to $Bu_{BC} = 50$), and very strongly stratified (corresponding to $Bu_{BC} = 500$).

In figure 3.14, there are nine plots that summarize the results. The $x$-axis of each plot represents the value of $U_{02}$. For these simulations, $U_{01}$ was held fixed at 1 while $U_{02}$ was varied. When $U_{02}$ is $1/-1/\frac{1}{3}$, it corresponds to the barotropic case/mixed BT-BC case with no transport/mixed BT-BC case with transport. The blue and green lines in each figure correspond to *sinuous* modes, the yellow and red lines correspond to *varicose* modes and the cyan line corresponds to a *baroclinic* mode, which represents the Phillips baroclinic mode. These modes were sorted by using projections of eigenvectors and matching based on nearest co-linearity. For the simulations which generated these plots, there were 420 values of $U_{02}$ and 2000 values of $k$. The simulation of all 420 $U_{02}$ values took roughly the same amount of time as a single high-resolution shallow water linear stability simulation with only 100 $k$ values.

#### The Effect on Maximum Growth Rates and Phase Speeds

This section will discuss the plots in the top two rows of figure 3.14. The discussion on the bottom row will be saved for the next section.

Beginning with the very strongly stratified case (left-most plots of figure 3.14), the growth rates are highly symmetric about $U_{02} = 0$. The lone asymmetry occurs near

$U_{02} = -1$ (the mixed BT-BC with no net transport regime), where a fifth mode appears (the cyan line). This fifth mode is much weaker than the other modes, and it corresponds to the BCPhil mode seen in the mixed barotropic-baroclinic shear with no net transport regime (see figure 3.7). There is a sharp cutoff region around $U_{02} = -0.9$ and $U_{02} = -1.1$ where this mode vanishes, suggesting that the mechanism which causes this instability can no longer transfer energy from the mean state to the perturbations. The phase speeds of this mode are much smaller in magnitude than the phase speeds of the other modes.

There are two sinuous modes that are represented by the green and blue lines. The blue line remains constant for all values of $U_{02}$, while the green line displays linear dependence on $U_{02}$. The reason the blue line is constant is because it is the surface-trapped BTSin mode; the strength of the jet in the top layer does not change, and so the growth rate of this mode is unaffected. The green line is linearly dependent on $U_{02}$ because it represents the bottom-layer trapped BTSin mode; the growth rate is proportional to the strength of the jet. The corresponding phase speeds display similar dependence on $U_{02}$.

The two varicose modes are weaker, but display similar behaviour to the sinuous modes; the surface-trapped BTVar mode (red line) is constant in strength, while the strength of the bottom-layer trapped BTVar mode (yellow line) is proportional to $U_{02}$.

In the strongly stratified case (center plots of figure 3.14), the growth rates are still mostly symmetric, however more small asymmetries are apparent. Near $U_{02} = 1$, the two-layer barotropic shear regime, the sinuous modes develop a small "bubble" region while the varicose modes diverge away from each other. The specific mechanism of this asymmetry must be due to wave resonances becoming modified, but the author has not looked into this in detail. Near $U_{02} = -1$, the BCPhil mode is stronger than in the very strongly stratified case, and the range of $U_{02}$ for which this mode persists is larger. The phase speeds of this baroclinic mode show a nearly linear dependence on $U_{02}$, but are still much smaller in magnitude than the phase speeds of other modes.

The behaviours of the sinuous modes in the strongly stratified case are nearly identical to the very strongly stratified case; the blue line corresponds to the surface-trapped BTSin mode, and it is nearly constant in strength for all values of $U_{02}$, while the green line represents the bottom-layer trapped BTSin mode, which displays the same linear dependence on $U_{02}$ as the very strongly stratified case.

The varicose modes in the strongly stratified case display nearly identical behaviour to the varicose modes of the very strongly stratified case for $U_{02} < 0$, however for $U_{02} > 0$, these modes behave differently. In the phase speed plot, the lines are indistinguishable from those of the very strongly stratified case, except that there is a kink for $U_{02} > 1$,

where the yellow line seems to swap places with the red line. It has been verified by the author that to the left of $U_{02} = 1$, the yellow (red) line is bottom (surface) -layer intensified, while to the right of $U_{02} = 1$, the red (yellow) line is bottom (surface) -layer intensified.

In the weakly stratified case, the cyan line represents the most dominant mode for all values of $U_{02}$. It does not directly correspond to the BCPhil mode in this case, as it displays different characteristics than the classic BCPhil mode for certain values of $U_{02}$. The maximum growth rate of this mode is smallest when $U_{02} = 0$, while the largest growth rate occurs for the large magnitudes of $U_{02}$.

The sinuous modes display drastically different features in the case of weak stratification. For $U_{02} < 0$ the bottom-layer trapped sinuous mode (represented by the green line) displays consistent linear behaviour, but it is much weaker than the more strongly stratified cases. The surface-trapped sinuous mode (represented by the blue line) is no longer constant with respect to $U_{02}$; instead it shows an negative linear dependence on $U_{02}$ for $U_{02} < -0.6$ and vanishes for $U_{02} > -0.6$. The phase speeds of the sinuous modes are relatively slower than the stronger stratification cases. For $U_{02} > 0$, the surface-trapped sinuous mode is not present, and the green line now represents the BCSin mode (see figures 3.2, 3.4).

The varicose modes are less affected by weak stratification than the other modes. For $U_{02} < 0$, the bottom-layer trapped varicose mode displays linear dependence on $U_{02}$, while the surface-trapped varicose mode is nearly constant (although it does display a weak positive linear dependence on $U_{02}$). The relative strengths of the modes are weaker than the more strongly stratified cases. For $U_{02} \in (0, 0.8)$, the varicose modes are consistent with the stronger stratification cases (red line is nearly constant, while the yellow line is linearly dependent on $U_{02}$), however there is a sharp transition when the growth rates of these curves become equal near $U_{02} \sim 0.8$. There are only three modes of instability for the interval $U_{02} \in (0.8, 1.3)$ for the weakly stratified case. The red line no longer corresponds to the surface-trapped BTVar mode, but instead corresponds to the BTVar mode depicted in the bottom-right plot of figure 3.3. It is of interest to note that in the phase speed plot for this interval, the varicose modes appear to coalesce and then separate. For $U_{02} > 1.3$, both varicose modes are once again present.

### The Effect on Layer-Wise Zonal Phase Shifts

This section discusses the layer-wise phase shift of modal structures. Layer-wise modal zonal phase shifts measure how much the modal structures "line up" with one another.

This is calculated in the QG model through the eigenvector data, and the bounds on this phase-shift are $0^\circ - 180^\circ$. These bounds are a consequence of the purely sinusoidal structure of the fields, and hence a phase shift of $n^\circ$ may be represented equivalently as a phase shift of $(360 - n)^\circ$ (this is a direct result of the Fourier decomposition applied, see section 2.1.3). In a purely barotropic case (for example, the BTSin and BTVar modes of figure 3.3), the layer-wise modal structures are nearly perfectly in phase (highlighted by the fact that the $\vec{u}_{BC}$ fields are much smaller than the $\vec{u}_{BT}$ fields). The BCSin mode of figure 3.3 depicts layer-wise modal structures which are nearly perfectly out of phase (highlighted by the fact that the $\vec{u}_{BT}$ fields are much smaller than the $\vec{u}_{BC}$ fields). In the Phillips problem, the surface layer of the baroclinic mode is found to be $90^\circ$ out of phase with the bottom layer (a well-known result, [30], sect. 6.8). Hence, a simple classification of these modes can be determined by considering the layer-wise phase shift of the modal structures; barotropic varicose and sinuous modes tend to be in-phase, baroclinic varicose and sinuous modes tend to be out-of-phase, while the baroclinic Phillips mode tends to be $90^\circ$ out of phase.

The bottom row of figure 3.14 depicts the layer-wise zonal phase shift of modes as a function of $U_{02}$. Beginning with the very strongly stratified case (bottom left plot of the figure), the first point of interest is that around $U_{02} = -1$, the BCPhil mode is prominent (thick solid line), and it shows the characteristic strong vertical phase shift, predicted by Eady [7], Charney [5] and Phillips [19]. However, the layer-wise phase shift is not quite $90^\circ$, but closer to $85^\circ$. As $U_{02}$ moves away from $-1$ in either direction, the vertical phase shift decreases until the mode loses the mechanism which allows it to extract energy from the basic state. Also around $U_{02} = -1$, the sinuous modes (thin solid lines) tend to a phase shift of around $20^\circ$ and the varicose modes (dashed lines) tend to a vertical phase shift of around $30^\circ$. This behaviour for the sinuous and varicose modes is consistent for $U_{02} < 0$.

When both flows move in the same direction ($U_{02} > 0$), the phase shifts develop a different behaviour. The bottom-layer trapped BTVar mode (yellow line) tends to a zero phase shift, then quickly "jumps" to a large phase shift around $160^\circ$ over the interval $U_{02} \in (0, 0.5)$. As $U_{02} \to 1^{\pm}$ the sinuous modes tend to $\sim 90^\circ$, and then quickly jump to being entirely in phase or entirely out of phase. This is the distinguishing feature of the BTSin and BCSin modes for the two-layer barotropic shear case, and it is important to note that this behaviour is nearly singular as $U_{02} \to 1$ for the case of very strong stratification. The varicose modes display similar behaviour here, as there is a quick transition to being identically in-phase or identically out-of-phase. The final point of interest around $U_{02}$ for this case is that the modes are not symmetric about $U_{02}$ - the surface- and bottom-layer trapped modes (both sinuous and varicose) seem to switch behaviour as $U_{02}$ crosses 1.

Moving to the case of strong stratification the differences are obvious, but the general behaviour of each mode is similar to the case of very strong stratification. The BCPhil mode has a larger unstable range, and hence the curve is wider here. The phase shift of this mode peaks close to 80° for this case, which is a smaller peak than the case of very strong stratification. The mode persists in a nearly symmetric way around $U_{02} = -1$, but there is more tolerance for this instability for $U_{02} < -1$ (the mode persists for a longer period when $U_{02} < -1$ and a shorter period when $U_{02} > -1$). The decreasing phase-shift response is seen more prominently in this case, with the phase-shift decreasing to around 75° before the mode becomes stabilized. The varicose and sinuous modes are nearly unaffected by the change in stratification for $U_{02} < 0$.

The other differences between cases occurs around $U_{02} = 1$, where the behaviour is no longer singular. The range where the sinuous mode phase-shifts increase abruptly is noticeably larger and the varicose modes are now symmetric across the $U_{02} = 1$ barrier (although, as discussed in the previous section, the yellow line becomes the surface-intensified varicose mode for $U_{02} > 1$).

The weak stratification case displays a different type of behaviour for most modes. The cyan line, which in previous cases represented the BCPhil mode and was only apparent for $U_{02}$ around $-1$, does not vanish for all values of $U_{02}$. Near the mixed, no transport case the phase shift is once again around 90°, and in this region it can be called the BCPhil mode. However, there is a transition region over the interval $U_{02} \in (-0.5, 0.5)$ where the phase-shift decreases and the mode transitions to become the BTSin mode.

The varicose and sinuous modes behave similarly to previous cases for $U_{02} < -0.6$, albeit with smaller phase-shifts. Around $U_{02} = -0.6$, the surface-trapped BTSin mode becomes completely stabilized and does not appear again (the small region around $U_{02} = -0.25$ where the blue line reappears is assumed to be numerical error). The other sinuous mode has a decreasing phase-shift for all $U_{02} < 0$ and the mode becomes stabilized when the phase-shift reaches 0°.

When the flows move in the same direction, there is similar behaviour around $U_{02} = 1$ for the sinuous modes, however there is only one varicose mode in this regime. This is to be expected, as there are only three modes which are seen in the two-layer barotropic shear case with weak stratification (see figure 3.2). The author has performed some low resolution shallow water linear stability analysis for $U_{02} = 0.5, 1.5$, and despite appearing prominently in the QG model, there were only traces of a fourth mode in the shallow water model, so the yellow line may not represent a physical mode in this regime. This implies that the fourth mode is an artifact of either the QG approximation, or the patched model

itself.

### 3.3.2 Calculating Layer-Wise Zonal Phase Shifts in the QG Model

The method of measuring the vertical phase shifts is not obvious, and so it will be explained in detail here. The structure of a specific mode in each layer is calculated as,

$$\psi_n = \mathrm{Re}\left\{\hat{\psi}_n(y)e^{ik(x-ct)}\right\}, \tag{3.16}$$

where $\hat{\psi}_n(y)$ is given by equations (2.53), and the coefficients $C_i$ are given by the eigenvectors. Expanding out the previous written equation explicitly, the structure $\psi_n$ can be written as,

$$\psi_n|_{t=0} = \mathrm{Re}\left\{\hat{\psi}_n(y)\right\}\cos(kx) - \mathrm{Im}\left\{\hat{\psi}_n(y)\right\}\sin(kx). \tag{3.17}$$

The modal structures are shifted in time by the same phase speed, and so the phase shifts are independent of the time variable, $t$, so it is dropped here. Using a simple trigonometric identity,

$$a\cos(x) + b\sin(x) = R\cos(x-\alpha), \tag{3.18}$$

where,

$$R = \sqrt{a^2+b^2}, \quad \text{and} \quad \tan\alpha = \frac{b}{a}, \tag{3.19}$$

equation (3.17) can be rewritten,

$$\Rightarrow \psi_n|_{t=0} = |\hat{\psi}_n|\cos\left(kx-\alpha_n\right). \tag{3.20}$$

The phase shift of each layer is given by,

$$\alpha_n = -\mathrm{atan2}\left(\mathrm{Im}(\hat{\psi}_n), \mathrm{Re}(\hat{\psi}_n)\right), \qquad \alpha_n \in (-\pi, \pi] \tag{3.21}$$

where atan2 is the four quadrant arc-tangent function. This means that the vertical/layer-wise phase shift, $\phi$, is given by

$$\phi = \min\left(|\alpha_2-\alpha_1|, 360^\circ - |\alpha_2-\alpha_1|\right). \tag{3.22}$$

The min function is required here to bound the phase shifts between $0^\circ$ and $180^\circ$.

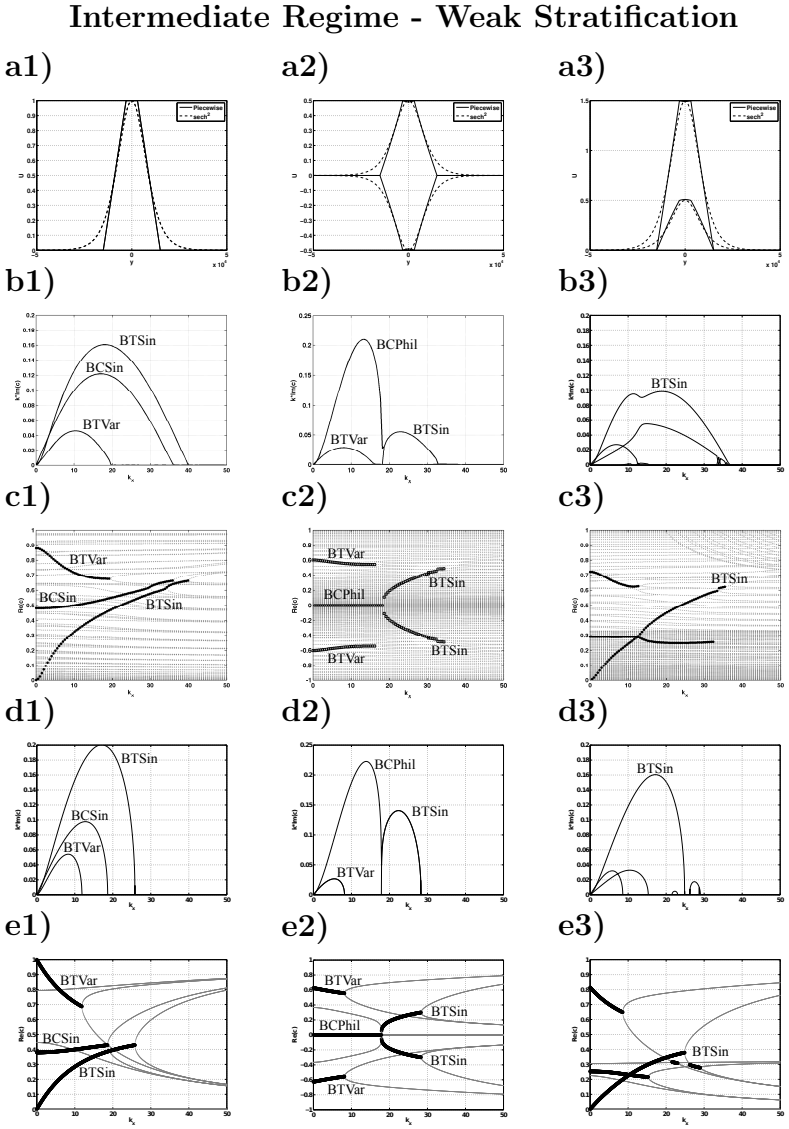


Figure 3.12: Comparing the results of the shallow water linear stability analysis to the QG linear stability analysis for the intermediate regime with weak stratification. Row **a)** compares the profiles of the RSW (dashed line) and QG (solid line) models. Rows **b)** and **c)** show the growth rates and phase speeds as predicted by the RSW model (respectively). Rows **d)** and **e)** show the growth rates and phase speeds as predicted by the QG model (respectively). Column **1)** corresponds to the two-layer barotropic shear case. Column **2)** corresponds to the mixed BT-BC shear with no net transport case, and column **3)** corresponds to the mixed BT-BC shear with net transport case.

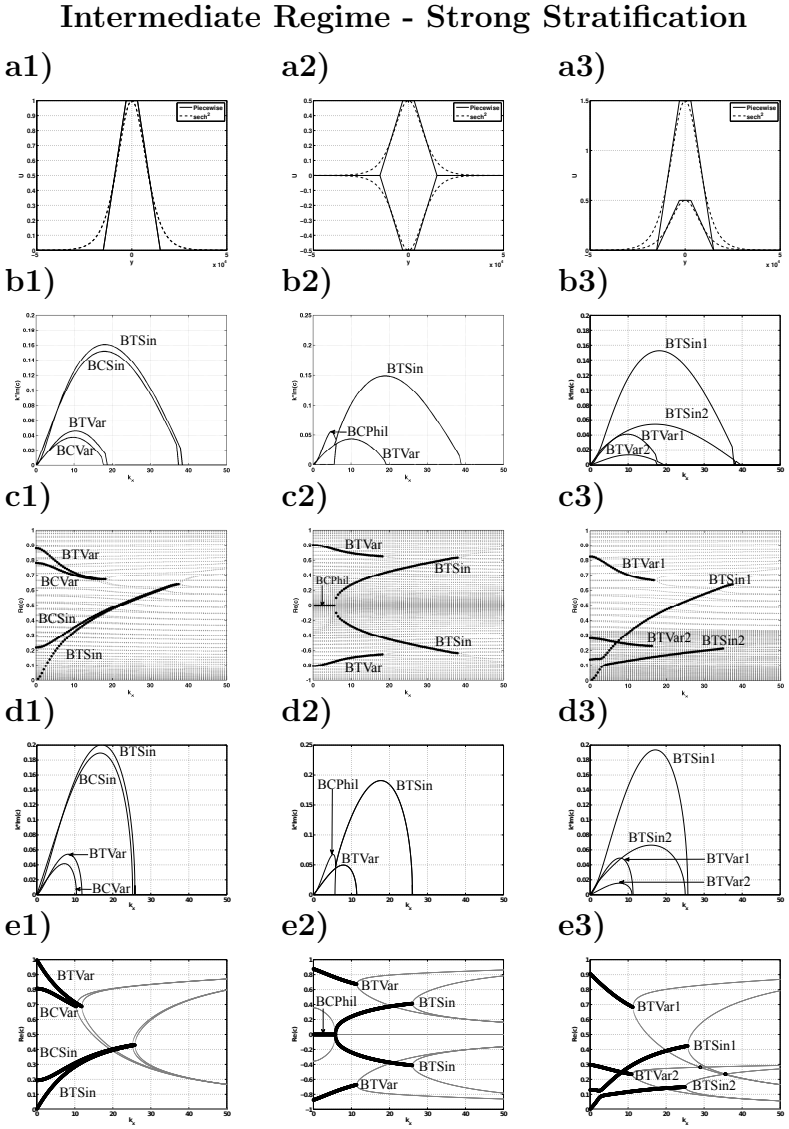


Figure 3.13: Comparing the results of the shallow water linear stability analysis to the QG linear stability analysis for the intermediate regime with strong stratification. Row **a)** compares the profiles of the RSW (dashed line) and QG (solid line) models. Rows **b)** and **c)** show the growth rates and phase speeds as predicted by the RSW model (respectively). Rows **d)** and **e)** show the growth rates and phase speeds as predicted by the QG model (respectively). Column **1)** corresponds to the two-layer barotropic shear case. Column **2)** corresponds to the mixed BT-BC shear with no net transport case, and column **3)** corresponds to the mixed BT-BC shear with net transport case.

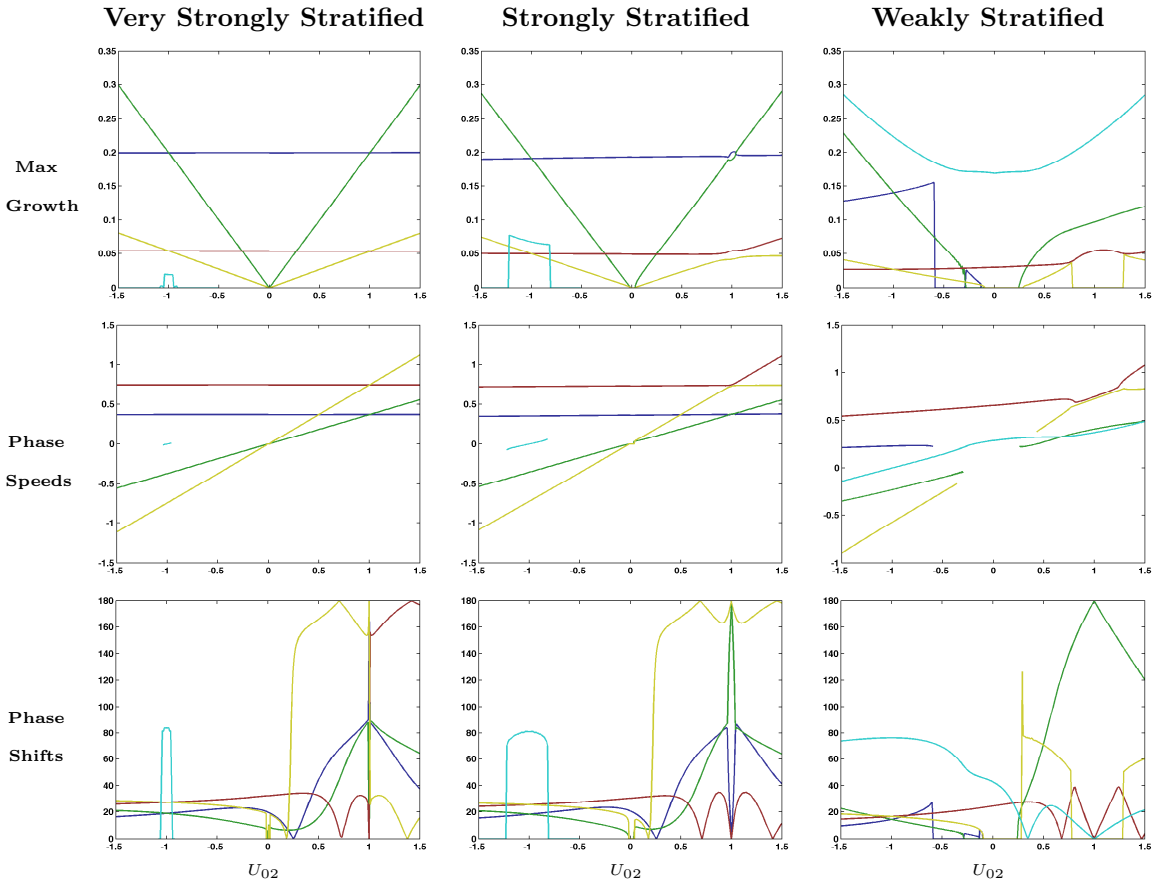


Figure 3.14: The maximum growth rates, corresponding phase speeds, and layer-wise zonal phase shifts presented as functions of the lower layer velocity, $U_{02}$. The vertical line $U_{02} = 1$ corresponds to the two-layer barotropic shear case, $U_{02} = -1$ corresponds to the mixed barotropic-baroclinic shear case with no net transport, and $U_{02} = \frac{1}{3}$ corresponds to the mixed barotropic-baroclinic shear case with net transport. The lines correspond to unstable modes as follows: the green line is the lower-layer BTSin mode, the blue line is the upper-layer BTSin mode, the yellow line is the lower-layer BTVar mode, the red line is the upper-layer BTVar mode, and the cyan line is the BCPhil mode.

## 3.4 Nonlinear Simulations

The results of the previous sections showed how stratification and rotation affects the stability of a variety of two-layer configurations. However, it does not describe the long term evolution of the system, nor does it describe the importance of individual modes to the evolution. In order to investigate this, a numerical code was developed by the author to approximate the solutions, see section 2.3 for more details.

In this section, there will be four nonlinear simulations discussed: a one-layer barotropic case, a two-layer barotropic shear case, and two separate two-layer mixed with no transport cases. The unstable modes of the two-layer mixed BT-BC shear with net transport cases proved to be difficult to classify as sinuous/varicose or BT/BC. This section aims to investigate how specific modes evolve, and so the mixed BT-BC shear with net transport case will not be simulated. Each of the following simulations is run on a $256 \times 256$ grid and integrated sufficiently long enough for each case to enter the nonlinear regime. The meridional domain is chosen to be $L_y = 20L_j$, sufficiently large such that the boundaries do not play a part in the internal dynamics, and the zonal domain is chosen so that the unstable mode of interest has two full wavelengths in the domain.

The goal of this section is not to investigate the dynamics of the nonlinear regime of the system, but to investigate how different modes influence the linear evolution of the system. In [10] the nonlinear simulations included non-primary mode evolution. It was shown that the sub-dominant modes were difficult to realize in general, and it was speculated that the modes were likely unimportant to geophysical fluid evolution.

### 3.4.1 One-Layer Barotropic Case

The nonlinear evolution of the Bickley jet in a one-layer rotating shallow water model has been studied extensively, [20], [9], and the results will only be presented here for completeness.

The parameters of this case correspond to the intermediate regime, (linear stability analysis results are presented in the right hand plots of figure 3.1). The nonlinear run was initialized with small amplitude white noise in the area of the jet, and was evolved over 144 advective time units (1 advective time unit = $L_j/U_0$ seconds), corresponding to roughly 17 dimensional days.

In figure 3.15, the perturbation fields after 65 advective time units are shown. The structure of perturbations clearly corresponds with the BTSin mode in figure 3.1, which

has a corresponding maximum growth rate of 0.161, (yielding an e-folding time of $\sim 6.25$ advective time units). Figure 3.16 shows how the fields grow in time. The slope of the linear regime of this plot corresponds to the nonlinear growth rate, which was estimated to be 0.158. This agrees with the linear theory to within 2%.

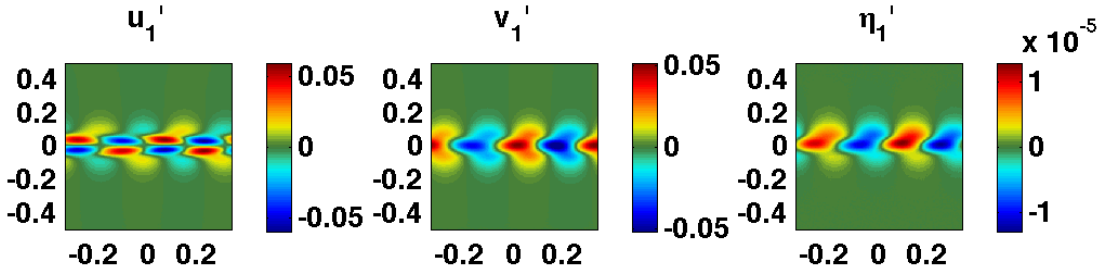


Figure 3.15: The perturbation fields after 90 outputs – corresponding to 64.8 advective time units. Compared to figure 3.1, the structure of these perturbation fields correspond to the BTSin mode. The $x$-axis corresponds to the zonal position and the $y$-axis corresponds to the meridional position.

After roughly 80 advective units, the system evolves into the nonlinear regime. Figure 3.17 shows the nonlinear evolution of the system. The initial jet evolves and creates four distinct vortical structures: two cyclones and two anticyclones. The symmetry persists until nonlinear effects take over around $t = 130$ and the vortices begin interacting with each other.

It is of interest to note that the BTVar mode did not appear in the linear evolution of the system and it is clear that the BTSin mode dominated the dynamics in the early times until the nonlinear effects began.

### 3.4.2 Two-Layer Barotropic Shear Case

This section focuses on the intermediate regime with weak stratification case. The reason for this is that the dominant mode does not change with varying stratification or $Ro_{BT}$, and thus it is not expected that the dynamics will change. This simulation ran for 200 advective time units.

In figure 3.18, the perturbation fields are shown in the regime of exponential growth. The structures presented in this figure compare to the results of the linear stability analysis, figure 3.3; the barotropic components of the nonlinear perturbation fields, $\vec{u}'_{BT}$ and

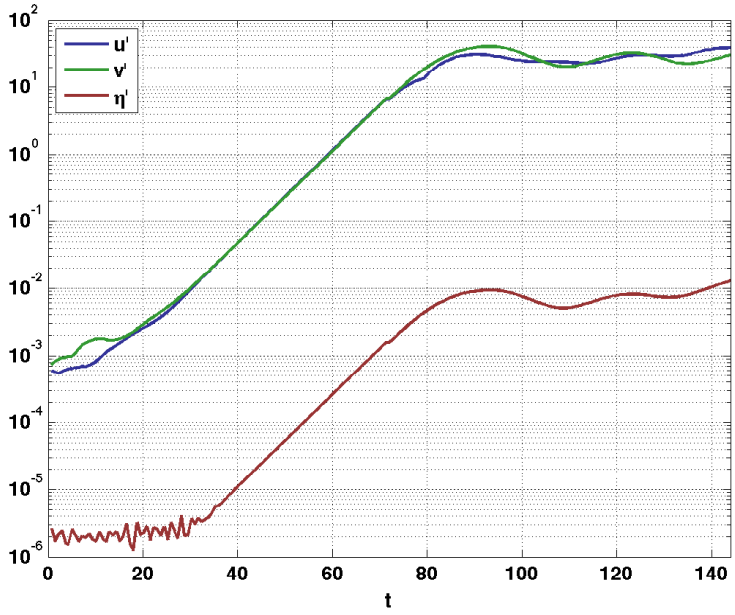


Figure 3.16: The magnitudes of the perturbation fields as a function of elapsed time (measured in advective time units). The linear regime corresponds to exponential growth, $t \in (40, 70)$.

$\eta_1'$ correspond to the barotropic components of the BTSin mode, while the baroclinic components of the perturbation fields correspond to the baroclinic components of the BCSin mode. Unlike in the one-layer BT case, it is seen that the nonlinear evolution of this system has two components of growth in the exponential regime. In figure 3.19, the magnitudes of the perturbation fields are shown. It is clear that the barotropic and baroclinic components evolve at different rates here; the barotropic fields grow at a rate 0.158 (1.8% error compared to the BTSin mode in linear theory), and the baroclinic fields grow at a rate of 0.121 (0.8% error compared to the BCSin mode in linear theory).

Figure 3.20 shows the nonlinear evolution of the barotropic and baroclinic vorticity fields. The barotropic and baroclinic vorticity are calculated as,

$$\zeta_{BT} = \hat{k} \cdot (\vec{\nabla} \times \vec{u}_{BT}), \quad \zeta_{BC} = \hat{k} \cdot (\vec{\nabla} \times \vec{u}_{BC}). \tag{3.23}$$

The barotropic vorticity fields for this case compare with the one-layer barotropic case well - the jet destabilizes and produces symmetric cyclones and anticyclones. However, in the later stages of nonlinear evolution, the two cyclones interact, as opposed to the one-layer case where the two anticyclones interact.

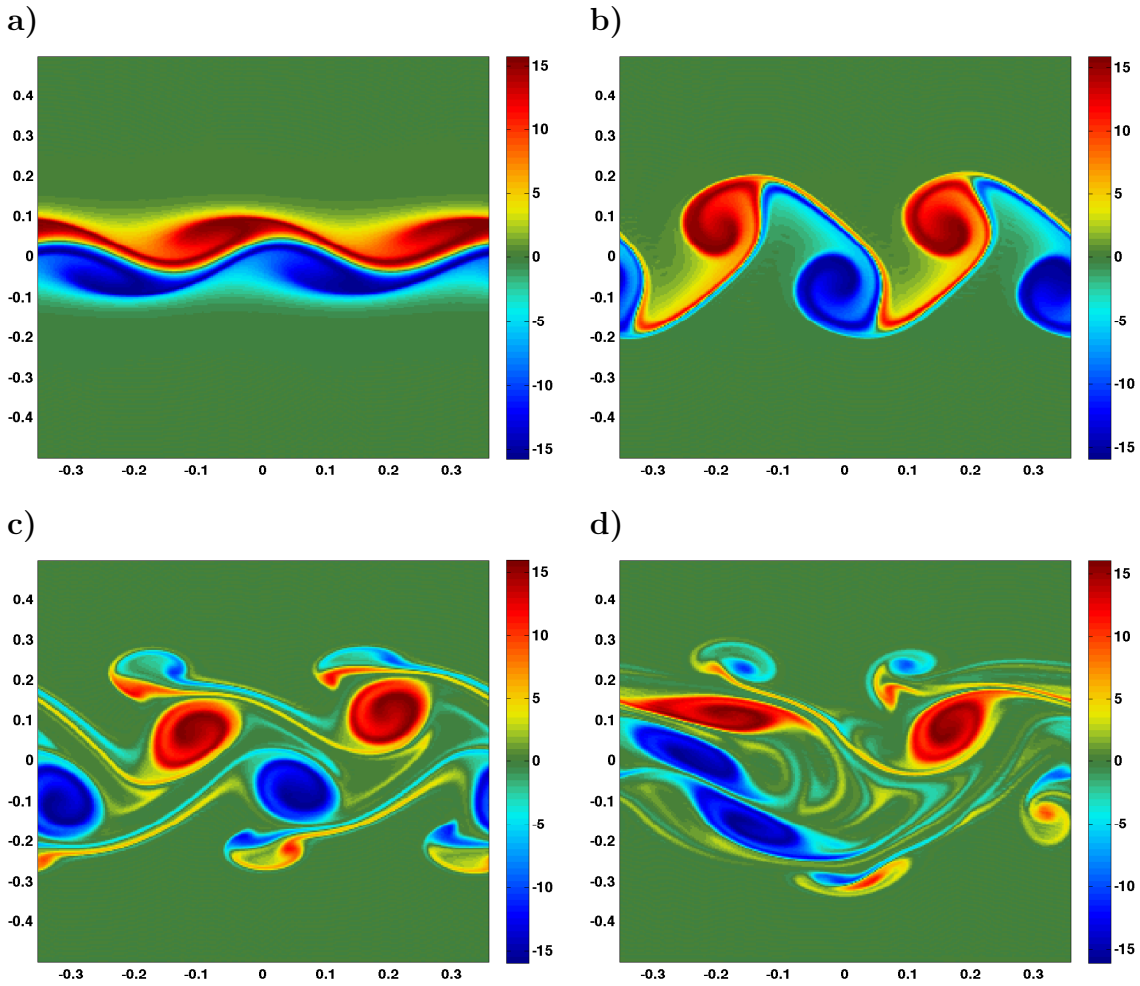


Figure 3.17: The nonlinear evolution of the one-layer barotropic case. The figures here show the vorticity field, $\zeta$ at time **a)** $t = 79$, **b)** $t = 94$, **c)** $t = 122$, **d)** $t = 144$. Times are given in advective units. The $x$-axis corresponds to the zonal position and the $y$-axis corresponds to the meridional position.

The baroclinic vorticity fields are sparser and appear to "trace out" the barotropic vorticity fields. The regions of highest baroclinic vorticity appear in the dipoles ejected from the primary vortices; this is in contrast to the barotropic vorticity fields where the regions of highest vorticity appear in the primary vortices.

The primary difference between the one-layer barotropic case and this two-layer barotropic

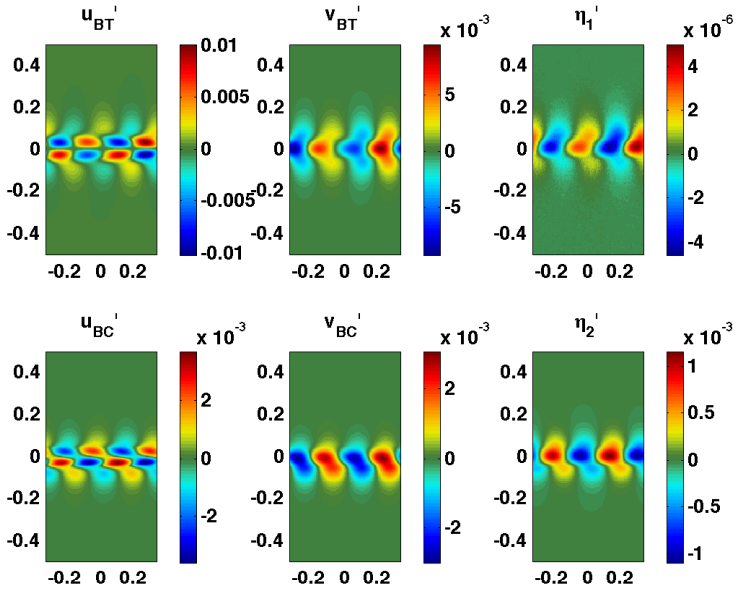


Figure 3.18: The BT-BC perturbation fields for the two-layer BT shear case at advective time $t = 80$.

shear case is that the nonlinear evolution depends on two modes: BTSin and BCSin, as opposed to the one BTSin mode in the single layer case.

### 3.4.3 Mixed Barotropic-Baroclinic with No Net Transport Cases

This section compares the nonlinear evolution of the weakly stratified mixed BT-BC, no transport case to that of the strongly stratified mixed BT-BC, no transport case.

Figure 3.21 shows the magnitudes of the layer-wise variables for both the weak and strong stratification cases. In the strongly stratified case, the $\eta_2'$ perturbation fields display an oscillatory behaviour in the exponential growth regime. The reason for this is that there are two dominant modes, the surface- and bottom-layer intensified BTSin modes. In figure 3.8, the modal structures are shown for the BTSin modes, **b)** and **c)** in the figure, and it can be seen that the $\eta_2'$ structures are identical in structure and magnitude, except flipped along the $y$-axis. The modes propagate in opposite directions at the same speeds, (as evidenced by the phase speed plot for this case in figure 3.7), and the co-dominant modes cause the $\eta_2'$ fields to be superpositions of the modal structures. This superposition

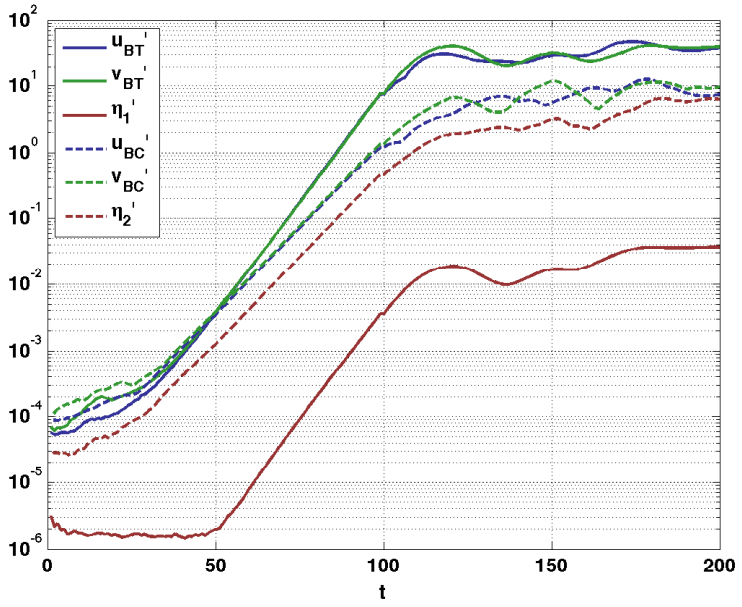


Figure 3.19: The magnitudes of the BT-BC perturbation fields for the two-layer BT shear case as a function of time (measured in advective time units). Notice the distinct difference in slopes of the barotropic and baroclinic fields.

of modes with identical magnitude $\eta_2'$ fields which propagate in opposing directions causes the oscillations in this field.

To show this, the period of oscillation is estimated to be 8 advective time units. The phase speed of each mode is roughly $\pm 0.4$, so a relative speed of 0.8 is taken. In order for two modes moving at 0.8 relative to each other to traverse half the domain[1] it takes 8.02 time units. This shows that the oscillations in the $\eta_2$ field are due to the superposition of two modes moving in opposite directions.

Comparing to the linear stability analysis, the linear theory predicted a growth rate of 0.210 for the weak stratification case while the nonlinear run estimated a growth rate of 0.209 (agreement with the linear theory to within 1% error). For the strong stratification case, the linear theory predicted a growth rate of 0.149, while the nonlinear run measured a growth rate of 0.148 (agreement with the linear theory to within 1% error).

[1]Because there are two full periods of the mode in the domain

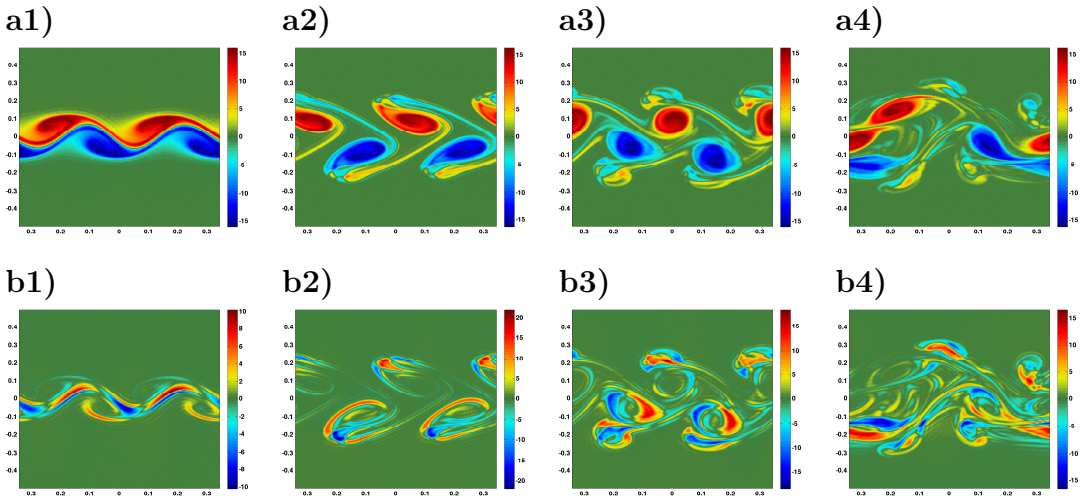


Figure 3.20: The nonlinear evolution of the two-layer barotropic shear case. The figures here show the barotropic vorticity field in row **a)**, and the baroclinic vorticity field in row **b)**. **1)** $t = 110$, **2)** $t = 130$, **3)** $t = 150$, **4)** $t = 170$. Times are given in advective units.

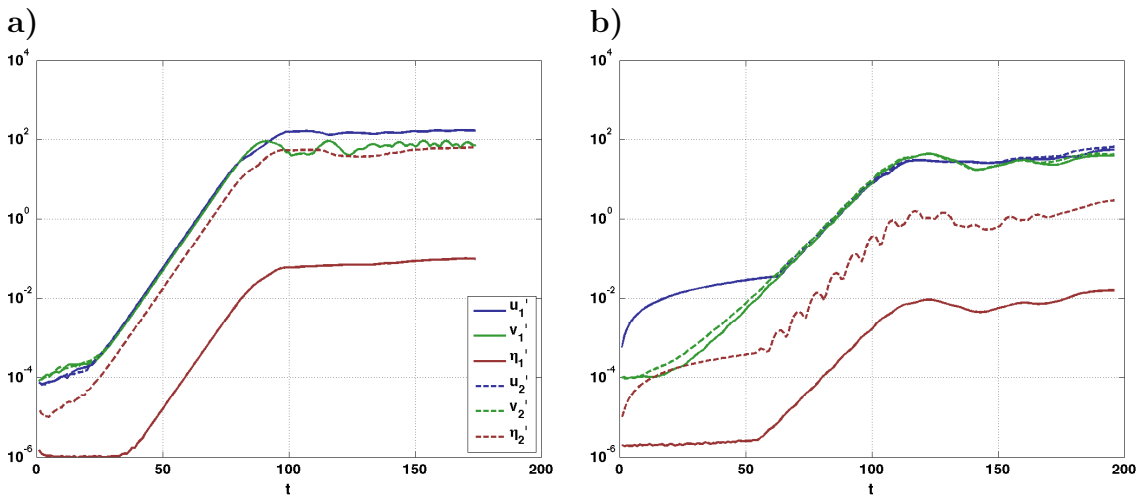


Figure 3.21: Magnitudes of the layer-wise variables as a function of time. **a)** the weakly stratified case, $Bu_{BC} = 5$, **b)** the strongly stratified case, $Bu_{BC} = 50$.

Figure 3.22 shows the perturbation fields of the nonlinear simulations in the exponential growth regimes of both cases. For plot **a)**, the structure clearly corresponds to the

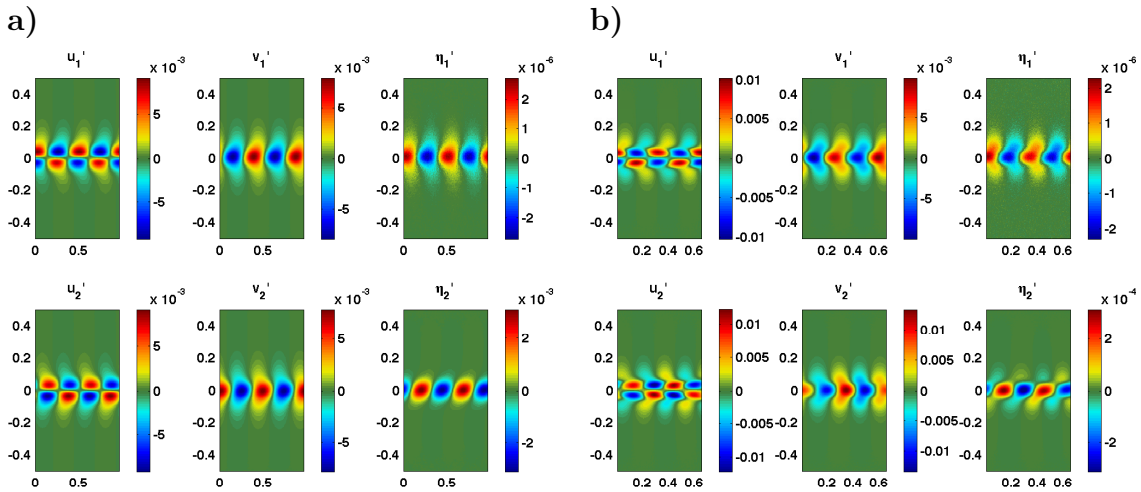


Figure 3.22: Structure of the perturbation fields for the two-layer mixed BT-BC shear with no net transport case with **a)** $Bu_{BC} = 5$, the weakly stratified case at $t = 60$, and **b)** $Bu_{BC} = 50$, the strongly stratified case at $t = 80$.

intermediate regime BCPhil mode presented in figure 3.6. For plot **b)**, the structures of the $\vec{u}_1'$ fields correspond to the structures in plot **b)** of figure 3.8, while the structures of the $\vec{u}_2'$ fields correspond to the structures in plot **c)** of the same figure. The $\eta_2'$ field is a superposition of both modes, and the $\eta_1'$ field corresponds to the $\eta_1'$ field in **b)** of figure 3.8.

Figure 3.23 shows the nonlinear evolution of the barotropic and baroclinic vorticity fields of the weak stratification case. The evolution of this case is noted as being completely different from the two-layer barotropic shear case; there is no vortex street formed and there are no dipoles ejected.

Figure 3.24 shows the nonlinear evolution of the *layer-wise* vorticity fields of the strong stratification case. The evolution for this case is similar to the one-layer barotropic case; the BTSin mode evolves independently in each layer (with the second layer flipped across the $y$-axis).

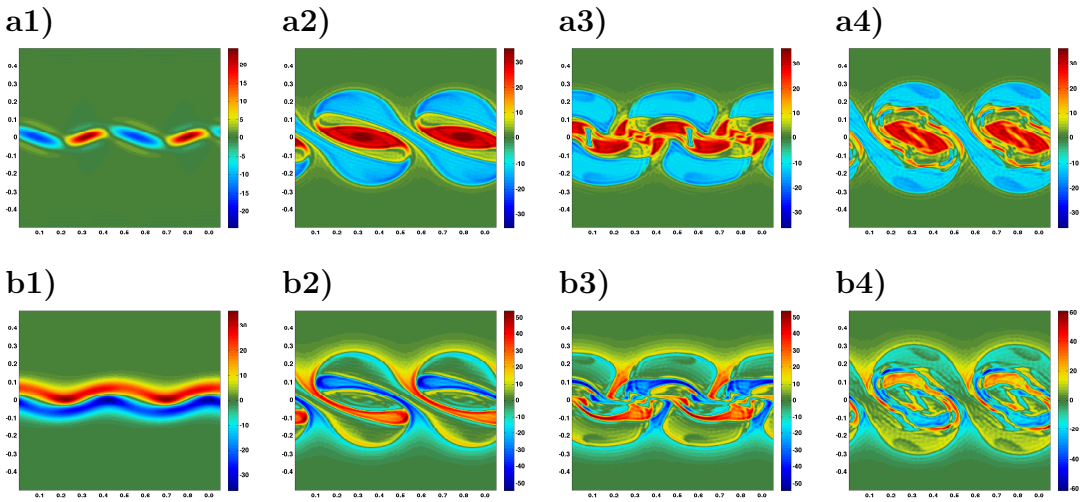


Figure 3.23: The nonlinear evolution of the two-layer mixed, no transport with **weak** stratification. The figures here show the barotropic vorticity field in row **a)**, and the baroclinic vorticity field in **b)**. **1)** $t = 80$, **2)** $t = 100$, **3)** $t = 110$, **4)** $t = 120$. Times are given in advective units. Notice the magnitudes of the baroclinic vorticity fields are much larger than the barotropic vorticity fields.

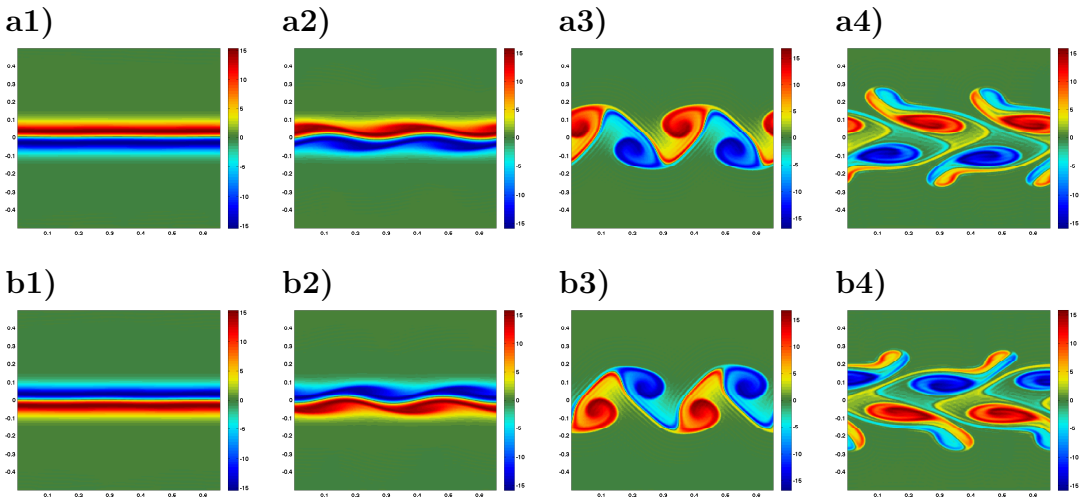


Figure 3.24: The nonlinear evolution of the two-layer mixed, no transport with **strong** stratification. The figures here show the surface-layer vorticity field in row **a)**, and the bottom-layer vorticity field in row **b)**. **1)** $t = 80$, **2)** $t = 100$, **3)** $t = 120$, **4)** $t = 140$. Times are given in advective units. Notice the magnitudes of the baroclinic vorticity fields are much larger than the barotropic vorticity fields.

## 3.5 Varying the Surface Layer Depth

All previous configurations were investigated using equal layer depths. In physical systems, regions of density transition are not limited to half-depths of the system. In this section, the effects of modifying the surface-layer depth in the two-layer barotropic shear configuration are investigated.

When compared to the one-layer case, the stratification introduced a third mode, BCSin, and strong stratification introduced a fourth mode, BCVar. This analysis uses the RSW model and five surface-layer depths corresponding to 2%, 10%, 20%, 30% and 40% total depth. In figure 3.25, the results are shown. In both stratification regimes, the BTSin and BTVar modes (represented by the dark solid and dashed lines respectively) are entirely unaffected by the varying depth. This is not a surprising result, as these modes are not dependent on stratification. However, the BCSin and BCVar modes are stabilized by thin surface layers. Although the BCSin mode is stabilized, even when the surface depth is 2% of the total depth, the growth rate is still larger than that of the BTVar mode, and the dynamics of the early stage evolution of the system are not expected to change significantly.

It is of interest to note that the growth rates of the BC modes do not respond to the effects of stratification until the surface layer is $\sim$ 10% of the total depth. Also shown in figure 3.25 are the wavelengths of maximum instability. As the surface layer depth decreases, the length-scale of BC instability increases.

A quick investigation on the effect of surface-layer depth to the BCPhil mode was conducted using the two-layer mixed with no transport configuration (results not shown). It was found that as $H_1/H$ becomes small, the growth rates increased slightly and the length scales decreased. This is in contrast to the BCSin and BCVar modes, which were shown to have growth rates which decreased, and length scales which increased with decreasing $H_1/H$.

Thus it is expected that the variation of layer depths only affects the evolution of systems when the BCSin or BCVar modes are dominant, and the importance of this variation is only significant when the layer depth becomes a small fraction of the total depth. When the layer depth is $<$ 10% of the total depth, then the BCSin and BCVar modes begin to stabilize and increase in length scale. The importance of surface layer depth is more significant to the mixed with no transport configuration, as the length scales of instability and growth rates are dependent on the ratio of layer depth to total depth.

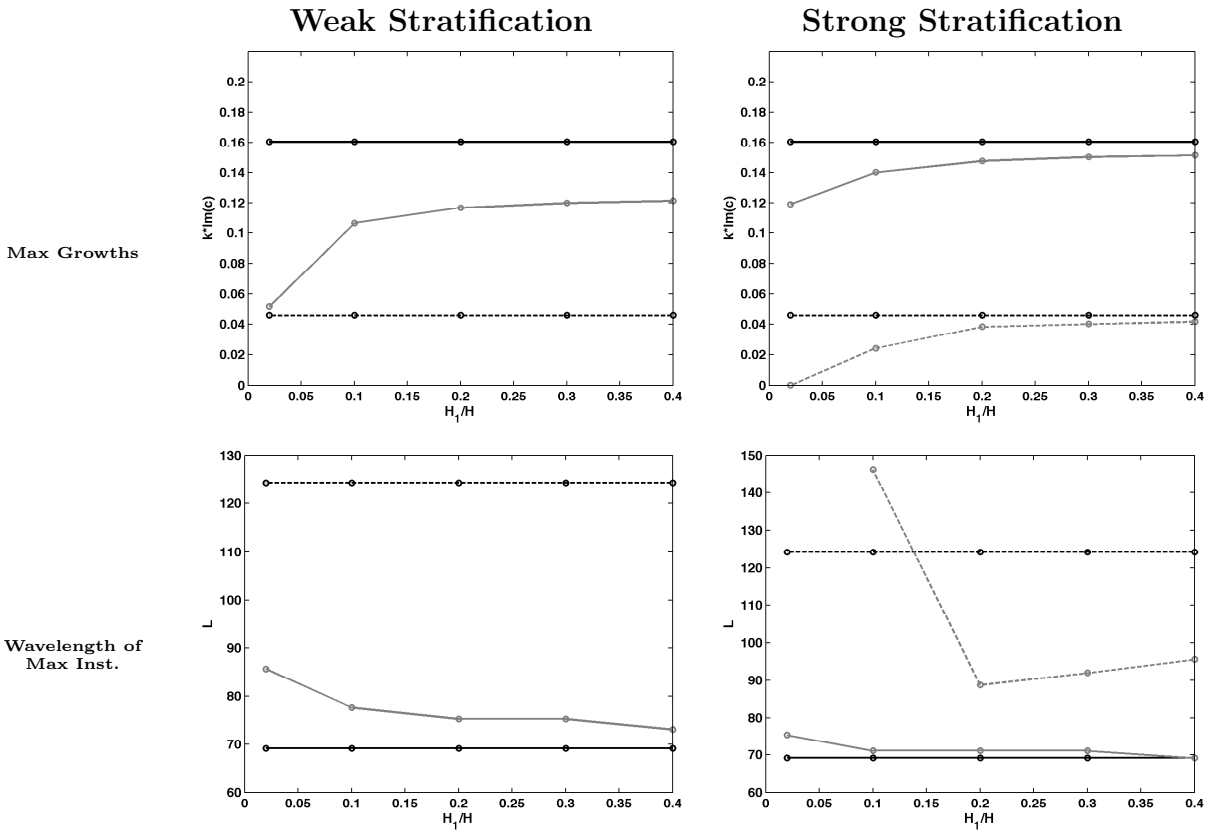


Figure 3.25: The maximum growth rates and corresponding wavelengths, shown as a function of varying surface-layer depth. The left plots are the weakly stratified barotropic case, the right plots are the strong stratified barotropic case.

# Chapter 4

# Instabilities of a Mesoscale Jet Above a Topographic Shelf

In the previous chapter, the effects of stratification and rotation were investigated in the context of two-layer flows. It has been shown in the literature that topography can have both stabilizing and destabilizing effects, [21], but the effects on individual modes have not been studied in depth. This chapter will study the effects of shelflike topography on the stability and early nonlinear evolution of two-layer systems.

The structure of this chapter is similar to the previous one; a set of test cases will be discussed, then analyzed using the rotating shallow water stability code. The parameter search will be broadened in the QG model, and some nonlinear results will also be discussed.

## 4.1 Topographic Rossby Waves

Topography modifies the wave solutions of the RSW equations. Consider a one-layer RSW model with a rigid lid in a zonal channel-like domain with no mean velocity profile, and a linearly sloped bottom, $\eta_B(y) = \alpha y$. The conservation of potential vorticity equation is,

$$\frac{\mathrm{D}}{\mathrm{D}t}\left[\frac{\frac{\partial v'}{\partial x} - \frac{\partial u'}{\partial y} + f}{H - \alpha y}\right] = 0. \tag{4.1}$$

To linearize this equation, assume that the topographic incline is small and use a Taylor expansion in the denominator,

$$\frac{\mathrm{D}}{\mathrm{D}t}\left[\frac{\frac{\partial v'}{\partial x}-\frac{\partial u'}{\partial y}+f}{H\left(1-\frac{\alpha y}{H}\right)}\right]=0, \tag{4.2}$$

$$\frac{1}{H}\frac{\mathrm{D}}{\mathrm{D}t}\left[\left(\frac{\partial v'}{\partial x}-\frac{\partial u'}{\partial y}+f\right)\left(1+\frac{\alpha y}{H}\right)\right]\approx 0, \tag{4.3}$$

$$\left(\frac{\partial}{\partial t}+u'\frac{\partial}{\partial x}+v'\frac{\partial}{\partial y}\right)\left[\frac{\partial v'}{\partial x}-\frac{\partial u'}{\partial y}+f+\frac{\alpha y}{H}\frac{\partial v'}{\partial x}-\frac{\alpha y}{H}\frac{\partial u'}{\partial y}+\frac{f\alpha y}{H}\right]\approx 0. \tag{4.4}$$

The nonlinear contributions are small compared to the linear contributions, and so the nonlinear terms are ignored. This yields the linearized equation,

$$\frac{\partial^2 v'}{\partial t\partial x}-\frac{\partial^2 u'}{\partial t\partial y}+\frac{f\alpha}{H}v'=0. \tag{4.5}$$

Assuming a Fourier decomposition of the form $\vec{u}'=\mathrm{Re}\left(\hat{\vec{u}}(y)e^{ik(x-ct)}\right)$, and substituting into the above equation yields,

$$-ic\frac{d\hat{u}}{dy}+\left(k^2c+\frac{\alpha f}{H}\right)\hat{v}=0. \tag{4.6}$$

Nontrivial solutions to the previous equation are of the form,

$$c=-\frac{\alpha f}{H}\frac{1}{k^2},\quad \frac{d\hat{u}}{dy}=0. \tag{4.7}$$

There are no associated imaginary components for the eigenvalues $c$, and so there are only neutral wave solutions with phase speed $-\frac{\alpha f}{H}\frac{1}{k^2}$, known as *topographic Rossby waves*.

Notice that in the northern hemisphere ($f>0$), the direction of movement is negative (towards the west) when $\alpha>0$ and positive (towards the east) when $\alpha<0$. This is the well known result stating that these waves move with shallow water "to the right" of the moving wave in the northern hemisphere. This result is reversed in the southern hemisphere. In the presence of a background flow, topography which induces waves propagating in the direction of mean flow is denoted as *prograde topography*, while topography which induces waves propagating in the direction opposite the mean flow is denoted as *retrograde topography*. This is summarized in figure 4.1.

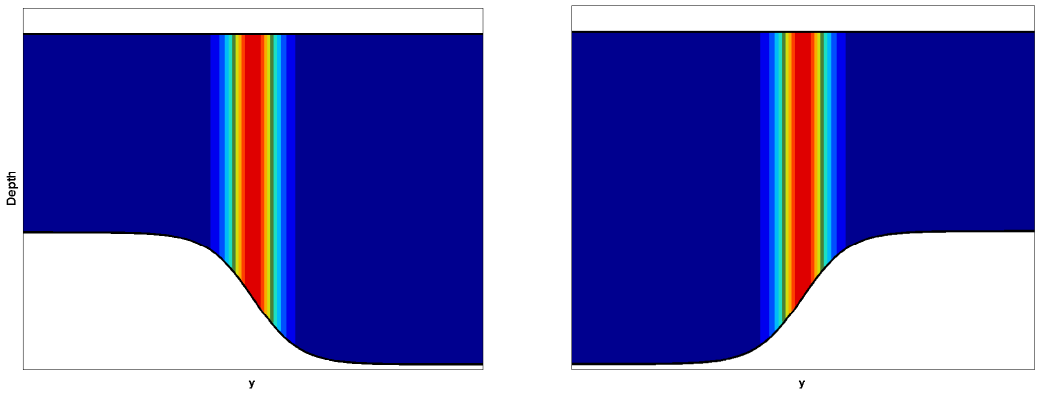


Figure 4.1: Comparing prograde and retrograde topography. The plots show a meridional slice of a barotropic jet which flows "out of the paper". This means that the **left** plot denotes the *prograde* case, as the current has shallow water to the right of the flow, and the **right** plot denotes the *retrograde* case, as the current has the shallow water to the left of the flow.

## 4.2 Modifying the Semi-Analytic Quasi-Geostrophic Model

In section 2.1.3 the semi-analytic model was derived and the $\eta_B$ term was dropped from equation (2.46b). In order to account for topographic effects, this term will be kept. The form of $\eta_B$ will be assumed to be linear and continuous at breaks between patches. Thus, this term will act as a forcing term on the evolution of quasi-geostrophic potential vorticity.

Assume for this model that $\eta_B$ takes on the form,

$$\eta_{BX}(y) = y \cdot s_X + b_X, \tag{4.8}$$

where $X = I, II, III, IV, V$, is the patch of interest. By requiring that the gradient of

potential vorticity is nil, the form of admissible $U_{iX}$ becomes,

$$U_{X1}(y) = C_{X1}\frac{g'H_1H_2}{f^2(H_1+H_2)}e^{-y\sqrt{\frac{f^2(H_1+H_2)}{g'H_1H_2}}} + C_{X2}\frac{g'H_1H_2}{f^2(H_1+H_2)}e^{y\sqrt{\frac{f^2(H_1+H_2)}{g'H_1H_2}}} + C_{X3}y + C_{X4} + \frac{fs_Xy^2}{2(H_1+H_2)}, \tag{4.9a}$$

$$U_{X2}(y) = -C_{X1}\frac{g'H_1^2}{f^2(H_1+H_2)}e^{-y\sqrt{\frac{f^2(H_1+H_2)}{g'H_1H_2}}} - C_{X2}\frac{g'H_1^2}{f^2(H_1+H_2)}e^{y\sqrt{\frac{f^2(H_1+H_2)}{g'H_1H_2}}} + C_{X3}y + C_{X4} + \frac{fs_Xy^2}{2(H_1+H_2)} - \frac{g'fH_1s_X}{f^2(H_1+H_2)}. \tag{4.9b}$$

The only notable differences from the flat-bottom case are the inclusion of quadratic terms at the end of each of these equations, and the additional constant term at the end of $U_{X2}(y)$. The velocity profiles are not as uniform in these cases, as can be seen in figure 4.2. In this figure, three cases of topography are shown — prograde topography, no topography, and retrograde topography. The lower-layer velocity fields are modified significantly in the presence of topography, while the surface-layer velocity fields are only effected slightly.

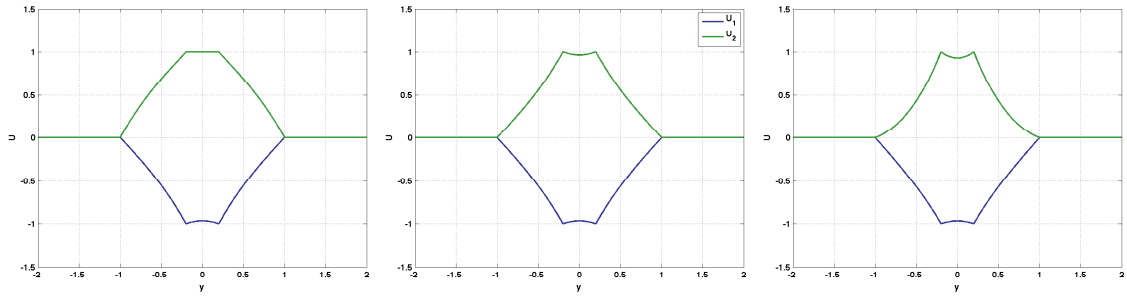


Figure 4.2: Velocity profiles for the semi-analytic QG model mixed BT-BC with no net transport cases with weak stratification. The profiles are exaggerated for effect. Left: the prograde case, Middle: the no topography case, Right: the retrograde case.

Due to the derivatives of $\eta_B$ being constant, the equations for the streamfunction remain the same as equation (2.51). The Talley conditions also remain the same, in particular (2.59) maintains the same form due to the assumed continuous nature of $\eta_B$.

The rest of the stability analysis is derived similarly to section 2.1.3. For the purpose of brevity, this derivation is omitted here.

## 4.3 Description of Cases

The cases discussed here will be similar to the ones of the previous chapter. The topography for these cases will follow the topography used in Poulin and Flierl 2005, it will be along the direction of flow and will use a hyperbolic tangent profile, where the characteristic width of the topography is twice that of the characteristic width of the jet.

The analysis in this section will focus on the intermediate regime and the topography will take one of three forms: *neutral*, *prograde*, or *retrograde*. The neutral case consists of no topography, which has been analyzed in the preceding chapter, and so will not be discussed in great detail here.

In the previous chapter, both weak and strong stratification regimes ($Bu_{BC} = 5$ and $Bu_{BC} = 50$, respectively), showed distinct stability characteristics, and so both regimes will be investigated here.

For the two-layer cases, the initial state is given as,

$$U_i(y) = U_{0i}\text{sech}\left(\frac{y}{L_j}\right)^2, \tag{4.10a}$$

$$h_1(y) = H_1 + \frac{\rho_2 f_0 L_j \left(U_{02} - U_{01}\right)}{g(\rho_2 - \rho_1)} \tanh\left(\frac{y}{L_j}\right), \tag{4.10b}$$

$$h_2(y) = H_2 - \frac{f_0 L_j \left(U_{02}\rho_2 - U_{01}\rho_1\right)}{g\left(\rho_2 - \rho_1\right)} \tanh\left(\frac{y}{L_j}\right) - \eta_B(y), \tag{4.10c}$$

$$\eta_B(y) = \left(H_2 \cdot \Delta\eta_B\right) \tanh\left(\frac{y}{2L_j}\right). \tag{4.10d}$$

Following the conventions of the previous chapter, the layer depths will be assumed equal, $H_1 = H_2$. For the two-layer barotropic shear case, $U_{01} = U_{02}$, and for the two-layer mixed BT-BC with no net transport case, $U_{01} = -U_{02}$. The range of $\Delta\eta_B$ is limited to depth changes of $\pm 25\%$ of the total depth (i.e. $\Delta\eta_B \in [-0.5, 0.5]$) due to the mean state of some cases causing the layer interface to intersect with the topography for larger values of $\Delta\eta_B$.

## 4.4 Linear Stability Analysis

In this section, each case will be investigated using a high-resolution shallow water stability analysis in tandem with a broad parameter space sweep using the semi-analytic QG model.

### 4.4.1 One-Layer Barotropic

The effect of shelflike topography on the stability of a Bickley jet in the RSW model has been investigated by Poulin and Flierl, [21]. The investigation consisted of a linear stability analysis over a range of Rossby numbers and topographic parameters, followed by a series of nonlinear simulations. While the authors looked at the effect of topography on the dominant BTSin mode, the BTVar mode was not discussed at all. In this thesis, the effect of topography on both BTSin and BTVar modes will be considered using the RSW equations and the QG model.

The semi-analytic QG model was introduced in section 2.1.3, but the derivation was for the two-layer problem. For the one-layer case, the velocity profiles are chosen to be piecewise linear and the topography is chosen to be piecewise constant. These choices force the potential vorticity to be piecewise constant. Figure 4.3 compares the one-layer QG model to the continuous one-layer SW model.

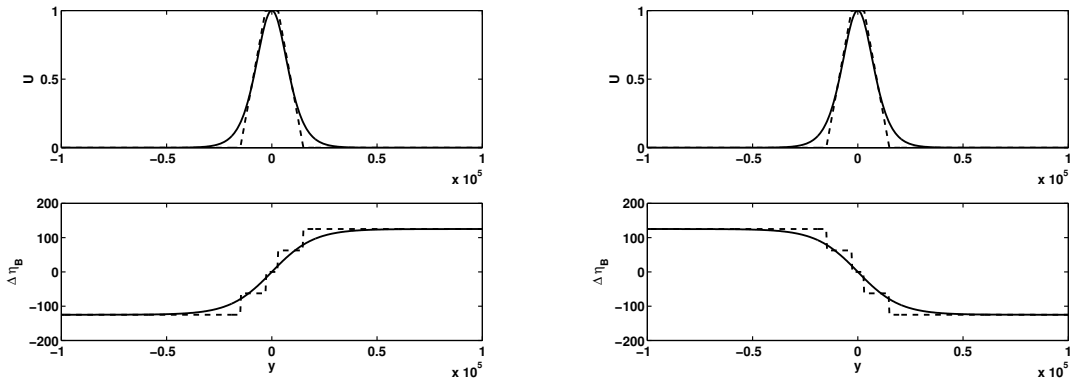


Figure 4.3: Comparing the velocity profile (top) and topography (bottom) of the one-layer five-patch QG model to the continuous model. The patched QG model is shown in the dashed black lines, while the continuous model is shown in the solid black lines. The positive $x$-direction is "coming out of the paper" so the retrograde case is on the left, while the prograde case is on the right.

The basic-state equations for the continuous one-layer SW profile are given here,

$$U(y) = U_0 \text{sech}\left(\frac{y}{L_j}\right)^2, \tag{4.11a}$$

$$h(y) = H - \frac{UfL_j}{g}\tanh\left(\frac{y}{L_j}\right) - \eta_B(y), \tag{4.11b}$$

$$\eta_B(y) = (H \cdot \Delta\eta_B)\tanh\left(\frac{y}{2L_j}\right). \tag{4.11c}$$

The growth rates of this configuration were calculated for both models and figure 4.4 summarizes the results. The $x$-axis of each plot represents the zonal $k$ values, while the $y$-axis represents the topographic deformation. The QG model compares well with the tendencies of the shallow water model, although the high-wavenumber cutoff is shorter for the QG model. The prograde topography corresponds to $\Delta\eta_B < 0$, while the retrograde topography corresponds to $\Delta\eta_B > 0$. Both unstable modes are destabilized for prograde topography, and stabilized for retrograde topography. Between $\Delta\eta_B = -1/4$ and $\Delta\eta_B = 1/4$, the maximum growth rates of each mode decrease monotonically by 12%. The behaviour of the BTSin mode confirms the results of [21].

While the growth rates of both modes are affected by topography, the length scales of maximum instability are affected in opposite ways. The retrograde case stabilizes both BTSin and BTVar modes, but moves the BTSin mode to smaller length scales and the BTVar mode to larger length scales. The prograde case destabilizes both BTSin and BTVar modes, but moves the BTSin mode to larger length scales and the BTVar mode to smaller length scales. Presumably, this behaviour could be derived by doing an analysis of the resonant interactions in the QG model but that is beyond the scope of this work.

### Extending to Large Topography

The topographic parameter was only varied over 25% of the total depth in the previous analysis, while Poulin and Flierl searched over a larger range of $\Delta\eta_B$, [21]. The reason for this restriction in the two-layer context is that the model does not support interfacial intersections. Particularly, in the mixed BT-BC with no net transport case with weak stratification, the interfacial deformations were large and intersected topography with deformations $\sim 30\%$ of the lower layer depth. The one-layer case is not limited by this, and the topographic parameter can be varied over a wider range. To investigate the effect of large topography, the QG model was run over a range of $\Delta\eta_B \in (-0.9, 0.9)$ and the results

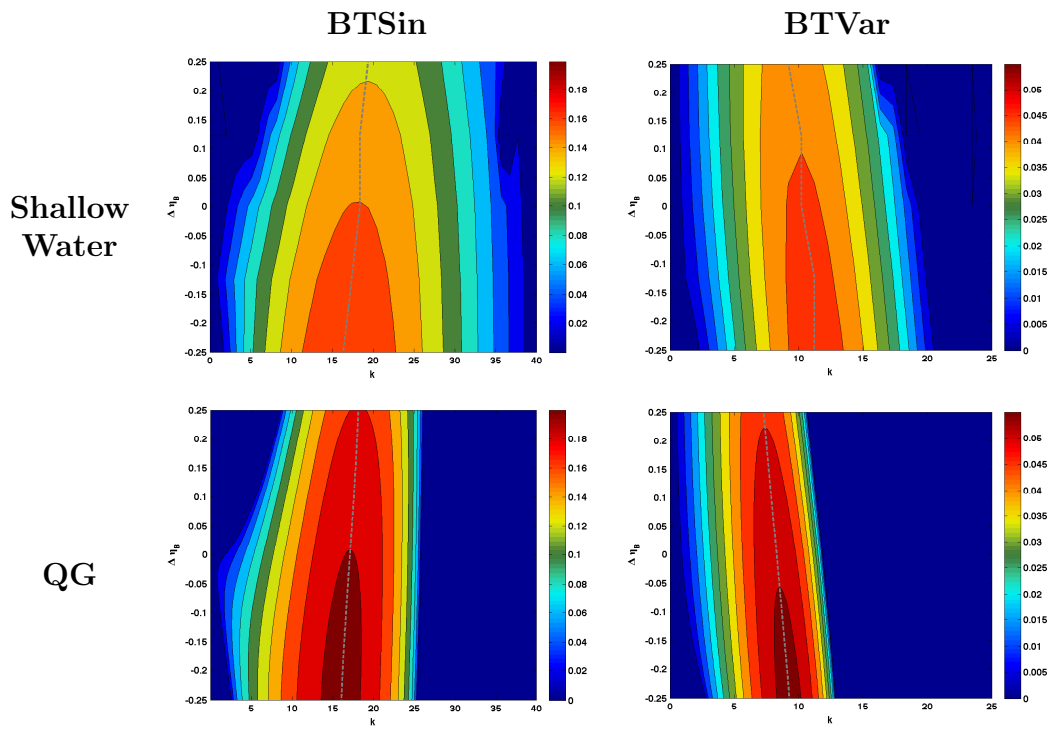


Figure 4.4: The growth rates of the one-layer model as a function of wavenumber and topographic scale for the limited range $\Delta\eta_B \in (-1/4, 1/4)$.

are shown in figure 4.5. However, these results are limited since the QG model does not allow for large deformations in the layer depth.

It is seen for the full range of $\Delta\eta_B$ that the prograde case is not strictly destabilizing. This agrees with the results of [21]. The maximum growth of the BTSin mode jumps to a larger $k$ when $\Delta\eta_B > 0.6H$, suggesting that the temporal evolution of the system will change significantly when the topography is sufficiently retrograde.

The BTVar mode moves sharply to smaller scales for strongly prograde topography and tends to larger scales for retrograde topography. Not shown explicitly in the figures, the growth rates of the BTSin mode are still of greater magnitude than the BTVar mode for all values of $\Delta\eta_B$.

Note that the QG model does not admit large $\Delta\eta_B$ under the assumptions of the model, and so these results are not quantitatively true. This does not mean that these results do not bear any physical meaning however, as it was shown in the previous chapter that the

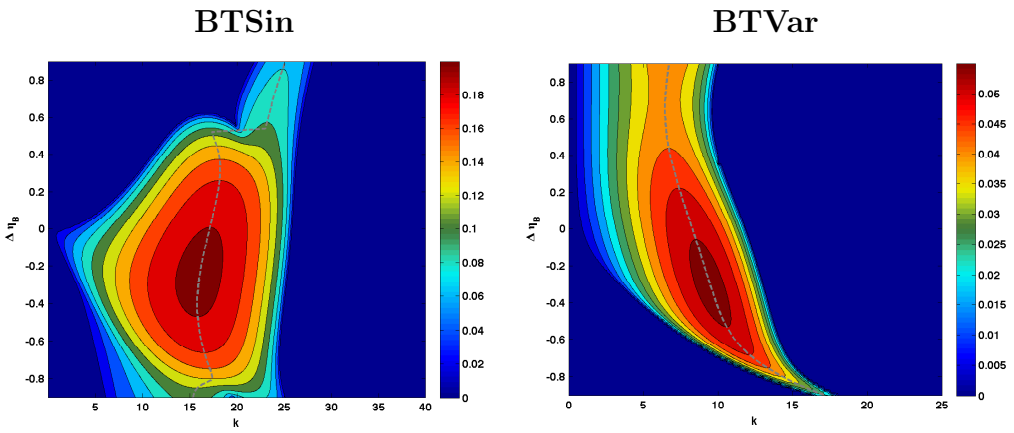


Figure 4.5: The growth rates for the full range of $\Delta\eta_B$ in the semi-analytic QG model. The dashed line indicates the position of maximum growth.

QG model can still be useful outside of the QG regime.

### 4.4.2 Two-Layer Barotropic Shear

In a sense, the one-layer case predicts the behaviour of a two-layer barotropic jet, however the introduction of stratification may modify the evolution of the system. In the previous chapter, it was shown that stratification introduced a third mode into the barotropic configuration, the BCSin mode. In this section, the effect of topography on all three growing modes will be investigated. The BTSin and BTVar modes will be compared to the one-layer analogues, while the BCSin mode will be investigated separately.

#### Weak Stratification

Figure 4.6 shows the growth rates and phase speeds of the two-layer barotropic shear case with weak stratification for prograde topography, retrograde topography, and no topography. There are three unstable modes in this configuration: BTSin, BCSin, and BTVar. In the case of no topography, the BTSin mode is dominant, but it will be shown that this is not always the case. The values of $\Delta\eta_B$ are chosen to show the effect of topography on phase speeds and wavenumber cutoffs on different modes.

In the case of prograde topography, the phase speeds of instability satisfy $\mathrm{Re}(c) > 0.4$ for all values of $k$. This is due to the topographic Rossby waves traveling in the direction

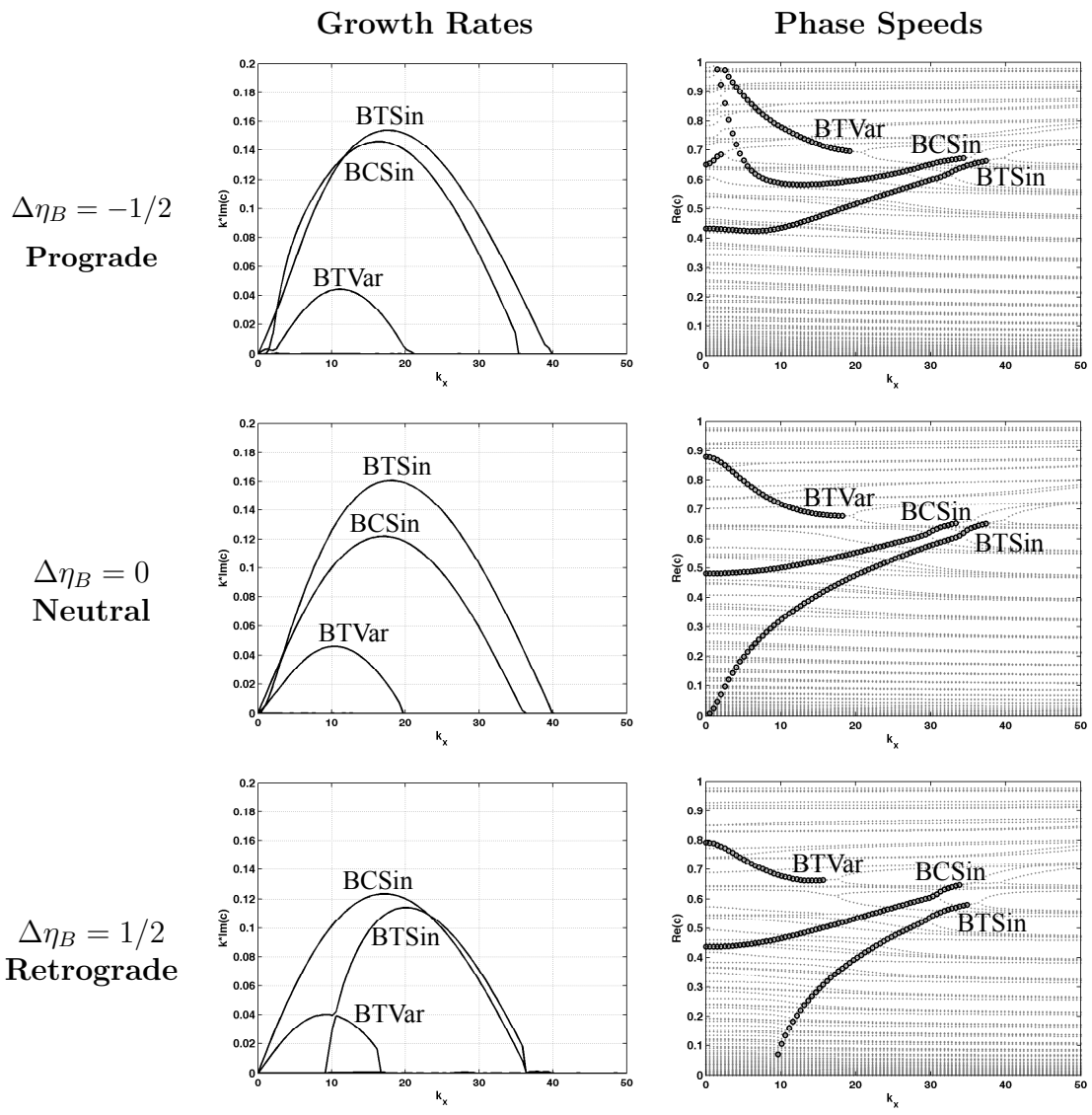


Figure 4.6: Growth rates and phase speeds of the prograde, and retrograde cases for the two-layer barotropic shear case with weak stratification.

of the current, which increases the phase speeds of instability for all values of $k$. Likewise, in the retrograde case, the phase speeds are decreased for all modes and all values of $k$ due to topographic Rossby waves moving against the current.

In the case of prograde topography, the BCSin mode develops a low-wavenumber cutoff around $k \sim 1.5$. Near this cutoff, the phase speeds of instability rapidly increase to $\mathrm{Re}(c) \sim 1$ before the mode is completely stabilized. In the case of retrograde topography, the BTSin mode develops a low-wavenumber cutoff around $k \sim 9$. Around this cutoff, it is seen that the phase speeds of instability decrease steadily to around $\mathrm{Re}(c) \sim 0.05$ before the mode is completely stabilized.

The BTVar mode also has a low-wavenumber cutoff for the prograde case, and seems to show traces of a developing weak fourth mode. While it is interesting that this fourth mode is apparent, the corresponding growth rate is nearly two orders of magnitude less than the maximum growth rate of this system, and it is not clear that it is converged. Near the cutoff value of BTVar, the phase speeds increase to a value around $\mathrm{Re}(c) \sim 1$ before the mode transitions into the weak fourth mode.

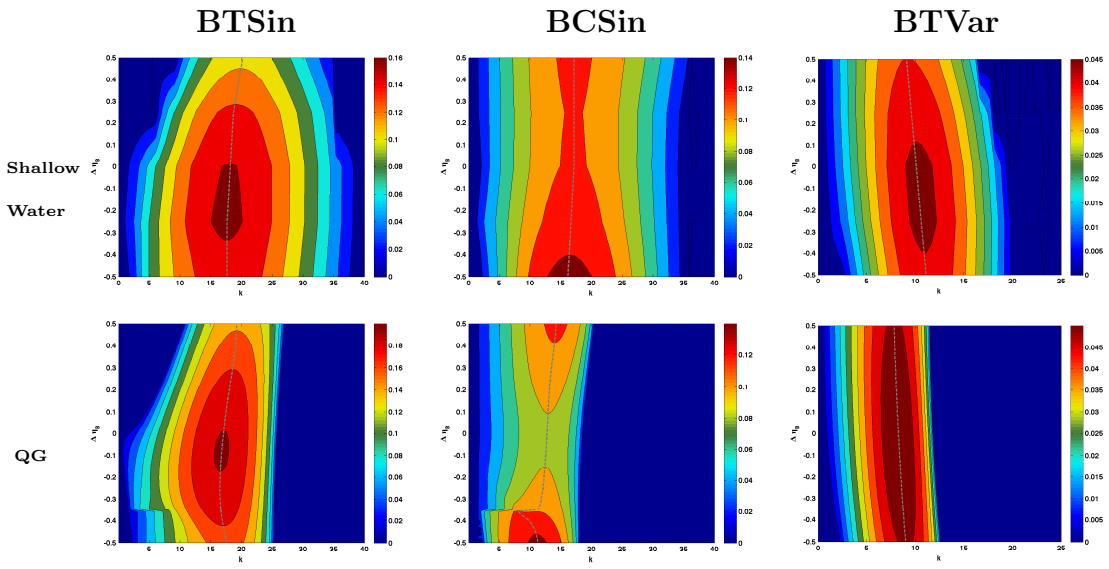


Figure 4.7: The growth rates of each unstable mode in the shallow water model and the QG model. The dashed line represents position of maximum growth.

Figure 4.7 shows contour plots of the growth rates for each growing mode as a function of topographic deformation and wavenumber. The dashed line highlights the position of maximum growth for each mode. It can be seen that the BTSin mode tends to larger scales for weakly prograde topography, and smaller scales for retrograde topography. In the QG model, as the prograde topography grows stronger, the wavenumber of maximum

growth rate recedes to smaller scales. In the BCSin mode, the most unstable wavelength shows little dependence on the topography in the shallow water model. It can be seen that there is a slight shift to larger scales for prograde topography, but the length scale remains constant in retrograde topography. The QG model shows a greater dependence on retrograde topography, and shows that the instability tends to smaller scales.

The most unstable wavenumbers of the BTVar mode agree qualitatively in both models; the wavenumber of maximum instability linearly decreases from strong prograde topography, $\Delta\eta_B = -0.5$, to strong retrograde topography, $\Delta\eta_B = 0.5$.

Figure 4.8 shows the maximum growth rates and vertical phase shifts of five shallow water cases compared to 200 QG cases. The blue line corresponds to the BTSin mode, the green line corresponds to the BCSin mode and the red line corresponds to the BTVar mode. In both maximum growth rate plots (top row of figure 4.8), the BTSin mode is seen to peak in the weakly prograde regime, and is relatively stabilized in the retrograde and strongly prograde regimes. This is consistent with the results from the one-layer case, where it was found that the BTSin mode was destabilized for prograde topography, and relatively stabilized in retrograde topography. However, the one-layer case showed monotonic destabilization as $\Delta\eta_B \to -0.25$, unlike the two-layer case which shows that strong prograde topography has a stabilizing effect. Thus it is concluded that the introduction of stratification has a stabilizing effect on growth rates of the BTSin mode in strong prograde topography.

The vertical phase shifts of the BTSin mode increase linearly away from $\Delta\eta_B = 0$, but remain weak for all cases of topographic deformation. This tendency is reflected in both the QG and RSW, however the QG model predicts a stronger dependence of phase shift on prograde topography. Even though the vertical phase shift increases with topographic deformation, the mode still remains largely barotropic.

Unlike the BTSin mode, the BCSin mode is partially stabilized in the weakly prograde regime, and destabilized in the presence of retrograde, and strong prograde topography. In the RSW model the BCSin mode becomes dominant as $\Delta\eta_B \to 0.5$, the strong retrograde case. The BCSin mode is entirely out of phase with no topography and becomes more in-phase for both retrograde and prograde topography. In the RSW model, the mode shifts to as little as 120° out-of-phase in strongly prograde topography, and so the mode is considered baroclinic in nature. In the case of strong retrograde topography, the mode also shifts towards becoming in-phase, reaching a minimum of 150° in the retrograde regime.

In the QG model, it can be seen that the phase shifts have a noticeable break around

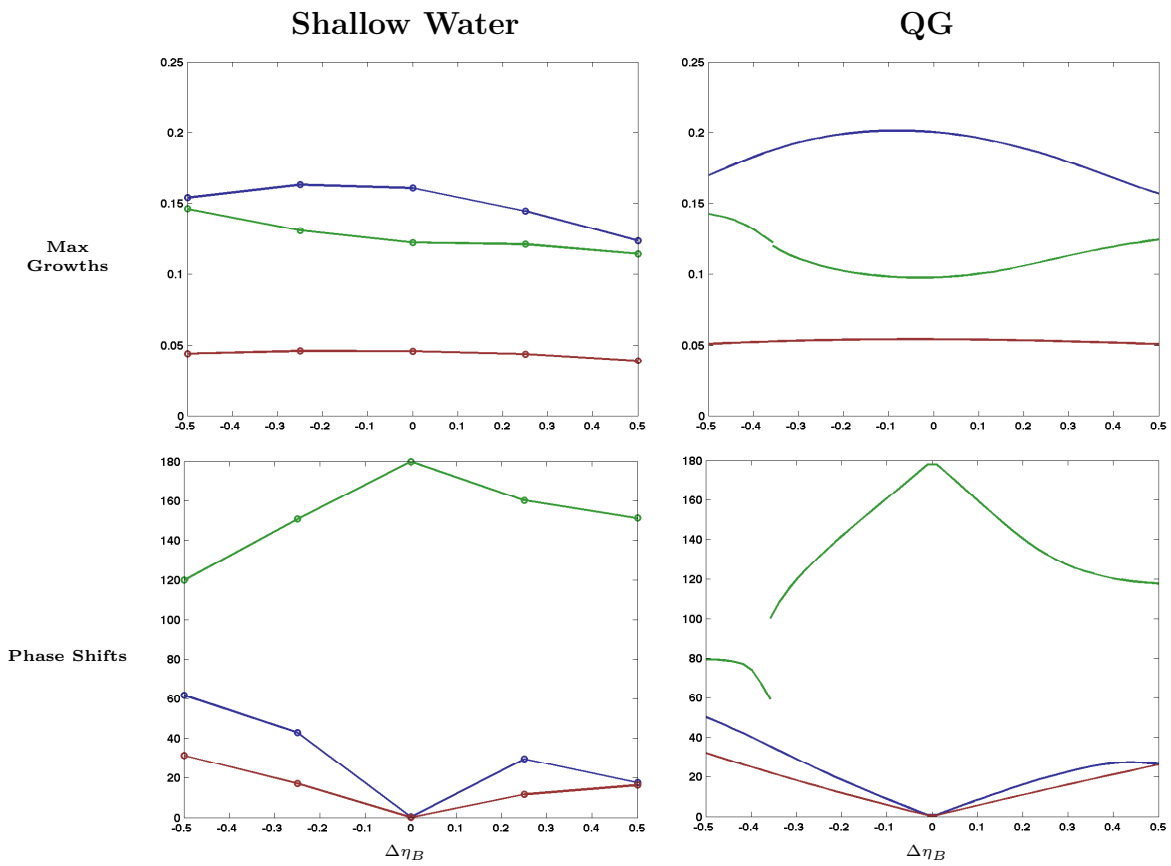


Figure 4.8: Comparing the maximum growth rates, phase speeds of maximum instability, and layer-wise phase shifts of the meridional velocity field for the shallow water stability analysis and the quasi-geostrophic stability analysis for the **weakly stratified two-layer barotropic shear** profile. The blue line is the BTSin mode, the green line is the BCSin mode, and the red line is the BTVar mode.

$\Delta\eta_B \sim -0.35$. Figure 4.9 shows the growth rates of each mode just to the left, and just to the right of the break. The grey line corresponds to the BCSin mode, and the plots show how this mode separates from the BTSin mode (the solid black line). The region around $\Delta\eta_B \sim -0.35$ was not analyzed using the RSW model, and so the author cannot confirm whether this result happens in the RSW model. Despite this break in the QG model, the vertical phase shift tendencies agree well between the two models.

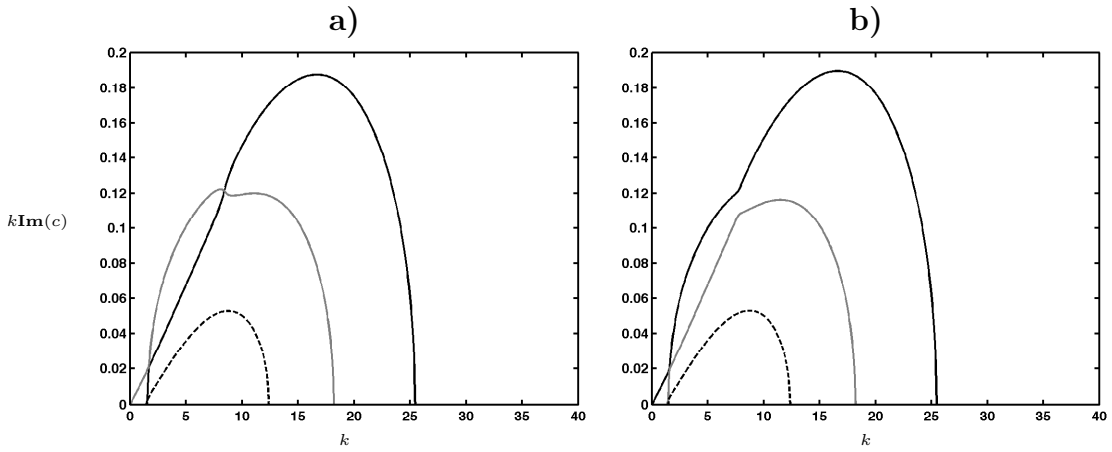


Figure 4.9: The growth rates of the two-layer barotropic shear case in the QG model for to the left, **a)**, and right, **b)**, of the break in the phase shift plot in figure 4.8.

The final mode to be considered is the BTVar mode. It is the weakest mode for all values of topography, and is therefore the least important to the evolution of the system. In figure 4.8, the BTVar mode is represented by the dashed black line. The maximum growth rate is nearly constant in both models, but has a shallow peak near $\Delta\eta_B = 0$. The effect of topography on phase shifts of the BTVar mode is minor. It displays the same qualitative behaviour as the BTSin mode — the phase shifts increase monotonically away from $\Delta\eta_B = 0$ — but the difference in phase shifts is smaller. In the RSW model, the vertical phase shift changes by 10° from the neutral case to the strongly retrograde case, and changes by 7° from the neutral case to the strongly prograde case. The QG model overestimates this measurement, but the model predicts phase shifts less than the BTSin mode, and so the models agree in that sense. Due to the minimal change in phase shifts and growth rates, it is concluded that topography has no significant impact on the BTVar mode.

### Strong Stratification

Figure 4.10 shows the growth rates and phase speeds of the two-layer barotropic shear case with strong stratification for prograde topography, no topography, and retrograde topography. This set of plots will be compared closely to the set of plots presented for the weak stratification case, figure 4.6.

As was found in the previous chapter, the primary difference between the weakly strat-

ified and strongly stratified case without topography is the introduction of a layer-wise out-of-phase varicose mode, denoted as the BCVar mode. Much like the other varicose mode, BTVar, figure 4.10 shows that the topography does not effect the growth rates or phase speeds of the BCVar mode significantly. The only significant change in phase speeds occurs in the strongly retrograde case, where it is seen that the unstable phase speeds decrease evenly from $\mathrm{Re}(c) \sim 0.8$ from $\sim 0.7$.

The behaviours of the phase speeds and wavenumber cutoffs of the other modes (BTSin, BCSin, and BTVar) largely reflect what was seen in the weakly stratified case, seen in figure 4.6. The most obvious difference (apart from the introduction of a fourth mode) is that the BCSin mode is dominant in both the strongly retrograde and strongly prograde regimes. In addition, the relative strength of the BCSin mode is greater in the strongly stratified case for all values of topographic parameter $\Delta\eta_B$.

Figure 4.11 shows the contour plots of unstable growth rates for each individual mode in both the shallow water and QG models. Compared to the weakly stratified case, figure 4.7, the tendencies of the sinuous modes are similar for both shallow water and QG models. The primary difference is that the strongly stratified case shows a more distinct low-wavenumber cutoff for the BCSin mode in the prograde regime. The length scales of maximum instability for both sinuous modes are also in good agreement.

In addition to the sinuous modes, the behaviour of the BTVar mode in the strongly stratified case corresponds to the behaviour of the same mode in the weakly stratified case. The most significant change in this regime is that the growth rates show a stronger dependence on topography, however this dependence is still weak.

Like the BTVar mode, the BCVar mode shows little dependence on topography. The length scale of maximum instability for this mode increases slightly when the topography varies from the strongly prograde regime to the strongly retrograde regime. It can be seen in the shallow water model that the BCVar mode has no low-wavenumber cutoff - the only mode to have this behaviour for all values of topographic deformation. The QG model shows a regime of $\Delta\eta_B \in (-0.4, -0.1)$ where there appears to be a low-wavenumber cutoff, but it has been confirmed by the author that this is a numerical issue involved with modal sorting, and so it is concluded that the BCVar mode experiences no low-wavenumber cutoff in this topographic range.

Figure 4.12 shows the maximum growth rates and corresponding vertical phase shifts of all four modes of instability in the two-layer barotropic shear case with strong stratification. The solid lines represent the sinuous modes, and the dashed lines represent the varicose

modes. The black colouring indicates BT modes, and the grey colouring indicates BC modes.

As was stated before, the BCSin mode is the dominant mode for a large range of $\Delta\eta_B$. Only in the case of no topography or weak topography does the BTSin mode dominate. Recall that the BTSin mode was dominant for most values of topographic parameter in the weakly stratified case. In the phase shifts plots, it can be seen in the case of no topography that the BCSin mode is entirely out of phase. Unlike in weak stratification, the mode moves sharply from 180° to 120° out of phase when the topography is varied in either direction. When the topography is steeper, the change in phase shifts is less significant. In strong prograde topography, the BCSin mode is most in-phase with a phase shift of 100°, compared to the weakly stratified case where the phase shift was 120°. A similar comparison can be made for the strongly retrograde case. Even though topography affects the phase shifts more significantly for strong stratification, the BCSin mode still remains largely out of phase for all values of topographic parameter.

In the QG model, the BTSin mode shows consistency in both stratification regimes by having a maximal value of growth in the weakly prograde regime. It is not obvious from the plot, but the BTSin mode has a peak growth rate when $\Delta\eta_B = -0.01$ in the QG model. The resolution of $\Delta\eta_B$ in the shallow water analysis was too low to confirm this result. The phase shifts for the BTSin mode show a sharp transition in weak topography, similar to the sharp transition seen in the BCSin mode. It is also seen that with steeper topography the phase shifts of the BTSin mode tend to decrease, and become more in-phase. This is not seen in the case of weak stratification. Even though the modes tend to become in-phase with steep topography, the BTSin mode in the strongly stratified case has a larger phase shift in both regimes of strong retrograde and strong prograde topography than the BTSin mode in the weakly stratified case.

The maximum growth rates of the BTVar mode shows a weak dependence on topographic parameter, however there is a shallow peak around $\Delta\eta_B = 0$. In the QG model, the phase shifts of the BTVar mode increase monotonically as $|\Delta\eta_B|$ increases. This agrees with the weakly stratified case, however the RSW model shows a decrease in phase shift as the magnitude of the topographic parameter becomes large. Ultimately, the difference in phase is not significant enough to change the behaviour of the BTVar mode, as the maximum vertical phase shift is only $\sim 30°$.

The growth rates of the BCVar mode shows a weak dependence with topography. Unlike the BTVar mode that reaches a maximum growth rate around $\Delta\eta_B = 0$, the BCVar mode reaches a minimum around $\Delta\eta_B = 0$. The BCVar mode is almost entirely out of phase for all topographic regimes (with a minimum phase shift of $\sim 140°$ in the strongly prograde

regime of the shallow water model). Therefore because the growth rates and phase shifts show only a weak dependence on topography, it is concluded that the effect of topography on the BCVar mode is insignificant to the early stage evolution of the two-layer barotropic system.

### 4.4.3 Measuring Vertical Phase Shifts in the RSW Model

It is worth noting how the vertical phase shifts are measured in the shallow water model. In the QG model the semi-analytic results allow the phase shift to be calculated using the eigenvector data (see section 3.3.2). However, the results of the numerical RSW linear analysis do not yield obvious phase shifts. This is due to the fact that, unlike the five-patch QG model, the RSW model admits modes that are not centered about $y = 0$, and does not have an exact form for the fields $\hat{\vec{u}}_i'(y)$ and $\hat{h}_i'(y)$. Figure 4.13 depicts two ways of measuring phase shift in the RSW model. The blue line calculates the phase shift along $y = 0$, while the red line calculates the phase shift where the modal structures reach local maxima (along $y \sim 0.1$). For the case depicted in the figure, the calculated phase shift along the blue line was 65°, while the calculated phase shift along the red line was 5°. The results presented here will measure vertical phase shift along the line of local maxima for the meridional velocity structures. However, it is important to note that this choice is arbitrary and there are many ways to measure this quantity.

### 4.4.4 Two-Layer Mixed Barotropic-Baroclinic with No Net Transport

This case is analogous to the two-layer mixed barotropic-baroclinic case with no net transport from the previous chapter, however there is one distinction: the flow in the lower layer now moves eastward, (in the positive $x$-direction) and the flow in the surface layer moves westward, (in the negative $x$-direction). This is to keep with the convention of prograde topography corresponding to $\Delta\eta_B < 0$ and retrograde topography corresponding to $\Delta\eta_B > 0$.

#### Weak Stratification

Figure 4.14 shows the growth rates and phase speeds of the two-layer mixed BT-BC case with no net transport in the neutral, prograde and retrograde regimes. The naming convention of each mode is slightly different here:

- modes that are suffixed by a number indicate a surface- (corresponding to 1) or lower-layer (corresponding to 2) intensified mode.
- modes that are suffixed by an asterisk are not unique modes in the sense that they do not have a separate growth rate curve. These modes denote a significant change in behaviour of a modal curve. Figure 4.15 shows how this occurs in the growth curves.

Also important to note is that the topography is prograde and retrograde with respect to the flow in the lower layer. Hence, topography which is labelled "prograde" have retrograde effects on the surface layer, and topography which is labelled "retrograde" has prograde effects on the surface layer. Considering that the topography is going to more strongly affect the dynamics in the lower layer, this naming convention seems to be the reasonable choice.

In the prograde case of figure 4.14 there exist four distinct modes, and one mode that corresponds to an existing mode changing behaviour, BTSin2*. Compared to the neutral case, it is apparent that modes that are lower-layer intensified (appended with a '2') have grown stronger, while the surface-layer intensified modes are slightly weaker. This is the expected behaviour, as it was seen in the two-layer barotropic shear case that prograde topography has a destabilizing effect on the current, while retrograde topography has a stabilizing effect. Further comparing to the neutral case, the phase speeds of instability for the BCPhil mode have drastically increased from $\mathrm{Re}(c) \sim \mathcal{O}(10^{-3})$ to nearly $\mathrm{Re}(c) = 1$, close to the cutoff value of the BCPhil mode. The phase speeds of the lower-layer intensified modes have also increased, while the phase speeds of the surface-layer intensified modes are not changed significantly.

In the retrograde case of figure 4.14 there are only three distinct modes, and one mode that corresponds to an existing mode changing behaviour, BTSin1*. The strong retrograde topography has completely stabilized the lower-layer intensified BTSin mode, and has nearly completely stabilized the lower-layer intensified BTVar mode (BTVar2). The strong retrograde topography only shows a destabilizing effect for the BTVar1 mode, as all other modes have been stabilized compared to the neutral case. Note that the growth rate curve of the BCPhil mode now encapsulates the BTSin1* mode, as opposed to the BTSin2* mode which was encapsulated in the prograde case. This transition occurs when the topographic Rossby waves change direction around $\Delta\eta_B = 0$. When this transition happens, the BCPhil curve "prefers" the mode that moves in the direction of the topographic waves, and the transition can be seen by comparing the phase speed plots of figure

4.14. Also of interest to note is that in both strong topographic regimes, at large scales, $k < 5$, the dominant modes are the varicose modes. This suggests that unlike previous cases where these modes were assumed negligible at all scales, the varicose modes are important at large scales and would dominate the early evolution at length scales where $k < 5$.

In figure 4.16, the contours of growth rates for each mode in the two-layer mixed BT-BC with no net transport cases as a function of $\Delta\eta_B$ and $k$ are shown. The dashed lines show the position of maximum growth. In the left-most plots of the first two rows of the figure, the full mixed BCPhil/BTSin* modes are shown. In these plots there are dashed grey lines that highlight the position of maximum instability for the corresponding BTSin mode (BTSin2 for $\Delta\eta_B < 0$ and BTSin1 for $\Delta\eta_B > 0$). How the growth rates of the BCPhil mode are affected by topography is consistent with what has been computed in the continuously stratified baroclinic Eady mode in the presence of topography, [11].

Beginning with the BTSin mode (top rows, column two of figure 4.16), the shallow water model predicts that the mode is completely stabilized when $\Delta\eta_B > 0$, while the QG mode predicts that the mode is gradually stabilized as $\Delta\eta_B \to 0.5$. The length scale of maximum instability is constant for $\Delta\eta_B < 0$, the regime where this mode represents the surface-intensified sinuous mode. When $\Delta\eta_B > 0$, the mode represents the lower-layer intensified sinuous mode and there is a decline in maximum growth rate and length-scale of maximum instability as $\Delta\eta_B$ increases.

The growth rates of the BTVar1 and BTVar2 modes are shown in the lower two rows of figure 4.16. It can be seen that the growth rates and length-scales of maximum instability react in opposite ways as the topography is varied; the BTVar1 (BTVar2) mode attains maximum peak growth rate when the topography is strongly retrograde (prograde), and attains largest length-scales of instability when the topography is strongly prograde (retrograde). The behaviour of these modes agree well with the behaviour of the BTVar modes in the two-layer barotropic shear cases (see figures 4.7 and 4.11).

The BCPhil mode is seen to have a low-wavenumber cutoff for all $\Delta\eta_B \neq 0$. It can also be seen in figure 4.16 that the wavelength of maximum instability is largest in the strongly prograde regime, and shortest in the strongly retrograde regime. It is important to clarify that the grey dashed line represents the position of maximum instability of the BTSin2 mode when $\Delta\eta_B < 0$ and represented the BTSin1 mode when $\Delta\eta_B > 0$.

Finally, figure 4.17 shows the maximum growth rates and vertical phase shifts as a function of topographic parameter $\Delta\eta_B$ for the weakly stratified mixed BT-BC case with no net transport. The thick solid line represents the BCPhil mode, while the thin solid lines

are the sinuous modes, and the dashed lines are the varicose modes. The black colouring of the thin lines denotes a surface-intensified mode and the grey colouring indicates a lower-layer intensified mode.

The first point of note is that the dominant mode for all values of $\Delta\eta_B$ is the BCPhil mode, and it is concluded that this mode is most important to the early time evolution of the system, regardless of the type of topography. In both the shallow water and QG models, the maximum growth rates of the BCPhil mode show a weak dependence on topography — there is a shallow peak in the intermediate prograde topography regime, and the mode is stabilized to a small degree for both types of strong topography. The phase shifts of this mode vary between roughly 60° and 80° over the range of topographic parameters.

The surface- and lower-layer intensified sinuous modes are shown to have a cutoff in both the RSW and QG models. This is not a sharp transition, but is instead the point where the curvature of the growth rate curve changes from having two local maxima, to having a single local maxima (representing maximum growth rate of the BCPhil mode). Figure 4.15 shows this transition. Apart from the vanishing maxima, the maximum growth rates of the sinuous modes behave as expected; the lower-layer intensified sinuous mode is destabilized in prograde topography and is stabilized in retrograde topography, while the surface-layer intensified sinuous mode is stabilized in prograde topography and is slightly destabilized in retrograde topography. The phase shifts of both modes remain small for all values of $\Delta\eta_B$, and hence the mode remains mostly barotropic.

The two varicose modes also react to topography in expected ways; the surface-layer (lower-layer) intensified mode destabilizes in the retrograde (prograde) regime and stabilizes in the prograde (retrograde) regime. The phase shifts of these modes also remain small for all $\Delta\eta_B$, however there is some disagreement between the shallow water and QG models regarding the tendencies of phase shift as $|\Delta\eta_B| \to 0.5$. This discrepancy between models is likely due to the method of measuring phase shifts in the shallow water model being prone to error, however this has not been confirmed.

### Strong Stratification

In figure 4.18 the growth rates and phase speeds are shown for the strongly stratified mixed BT-BC case with no net transport for neutral, retrograde and prograde topography. The naming conventions match those of the weakly stratified case, however there are no encapsulated modes in the cases shown.

Beginning with the prograde case, there are four modes that are labelled in the growth rates plot, and there is a weak fifth mode around $k \in (0, 6)$ that is unlabeled. The strongest

four modes are what typically arise in two layer flows with barotropic shear – two sinuous modes and two varicose modes, one of each type of mode corresponds to a surface intensified mode, and the other corresponds to a lower-layer intensified mode – however, the fifth mode has a modal structure that is unlike the previous structures presented. Figure 4.19 shows the layer-wise modal structures of this mode. It is apparent from the magnitudes of each field that the mode is lower-layer intensified. Looking at the meridional fields, it is also seen that the mode is symmetric about $y = 0$, implying by definition that it is sinuous. However, unlike other sinuous modes there are strips of large magnitude perturbation in the meridional velocity fields that extend for nearly 80% of the domain. Despite the interesting structure of this mode, the maximum growth rate is an order of magnitude less than the peak growth rate of the whole system, and so it is not considered to be important to the early stage evolution of the system.

Continuing with the prograde case, it is seen that the surface intensified modes (BTSin1 and BTVar1) remain unchanged from the case of no topography for both the growth rates and phase speeds. The lower-layer intensified modes (BTSin2 and BTVar2) are modified in the expected way; they are destabilized and the unstable phase speeds are increased. In addition, the BTVar2 mode develops a low-wavenumber cutoff around $k = 8$. Around this cutoff, the phase speeds tend to $\mathrm{Re}(c) = 1$ before the mode is completely stabilized.

In the retrograde case, there are only four unstable modes (compared to the five unstable modes of the previous cases). The surface-intensified BTSin1 mode is dominant for most wavenumbers ($k \in (6, 38)$) in the domain. In the largest scales investigated ($k \in (10^{-2}, 5)$), the BTVar1 mode is dominant, with the BTVar2 mode being secondary. Unsurprisingly, the lower-layer intensified modes have been stabilized and the phase speeds have decreased in the presence of retrograde topography. Additionally, the range of instability for the BTSin2 mode has decreased significantly; the low-wavenumber cutoff of this mode is $k = 22$ and the high-wavenumber cutoff is $k = 28$. Due to this mode being weak, the numerical methods are susceptible to error. This error is apparent in the phase speed plot around the unstable region of the BTSin2 mode.

The BCPhil mode is seen to completely stabilize in the presence of strong topography. This will be addressed in figure 4.21.

In figure 4.20, the growth rates of each unstable mode for this case are shown. As was implied by the previous discussion, the growth rates and wavelength of maximum instability are almost completely unaffected by the presence of topography. Thus it is concluded that stratification suppresses the influence of topography on surface flows. This was also seen

in the weakly stratified case to a lesser degree – the stabilizing and destabilizing effects on the surface intensified modes were less prominent than the effects on the lower-layer intensified modes.

As was concluded in the previous chapter, the presence of strong stratification tends to decouple each layer, and minimizes the layer-layer interactions. Thus, it is not surprising that the behaviour of the BTSin2 and BTVar2 modes are similar to the BTSin and BTVar modes in the strongly stratified two-layer barotropic shear case (see figure 4.11).

Figure 4.21 shows the maximum rates of growth and vertical phase shifts for each mode in the strongly stratified two-layer mixed BT-BC with no net transport case. The thick black line represents the BCPhil mode, the thin solid lines represent the sinuous modes, and the dashed lines represent the varicose modes (as per usual). The thin black lines representing a surface intensified mode, and the thin grey lines representing a lower-layer intensified mode. In addition to the standard five lines, there is a thick solid grey line as well, representing the weak fifth mode, as shown in figure 4.19.

The prominent feature of figure 4.21 is that the BCPhil is shown to vanish for relatively weak topography in the QG model. It may be inferred that this also happens for the RSW case, however with only 5 grid points, it is difficult to justify this inference. In the QG model, the BCPhil mode has a sharp cutoff, similar to the very strongly stratified case as presented in figure 3.14. Based on the analysis presented here and in the previous chapter, it is concluded that the baroclinic Phillips-type mode exists preferentially in weakly stratified flows.

Once again, it is seen that both surface intensified modes are largely unaffected by topography, although the vertical phase shift of the BTSin1 grows from 10° to 30° out-of-phase over the entire $\Delta\eta_B$ range in the shallow water model (and from 10° to 60° in the QG model).

The lower-layer intensified modes show expected results, as the BTVar2 and BTSin2 modes are destabilized in the prograde regime, and stabilized in the retrograde regime. However, the shallow water model shows a monotonic increase in the maximum growth rate of the BTSin2 mode as $\Delta\eta_B \to -0.5$, whereas the QG model predicts that the BTSin2 is slightly stabilized in strong prograde topography.

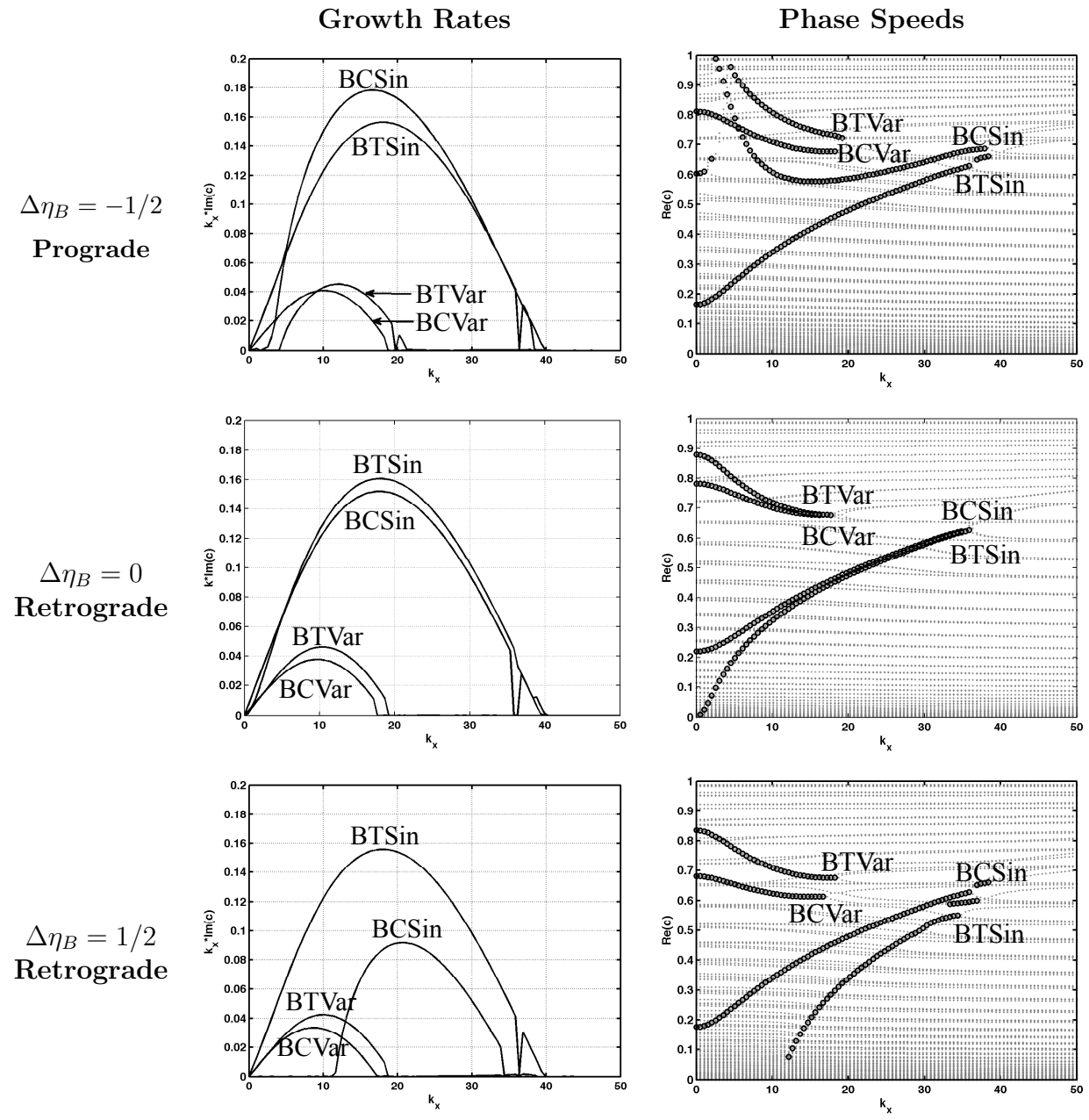


Figure 4.10: Growth rates and phase speeds of the prograde, and retrograde cases for the two-layer barotropic shear case with strong stratification.

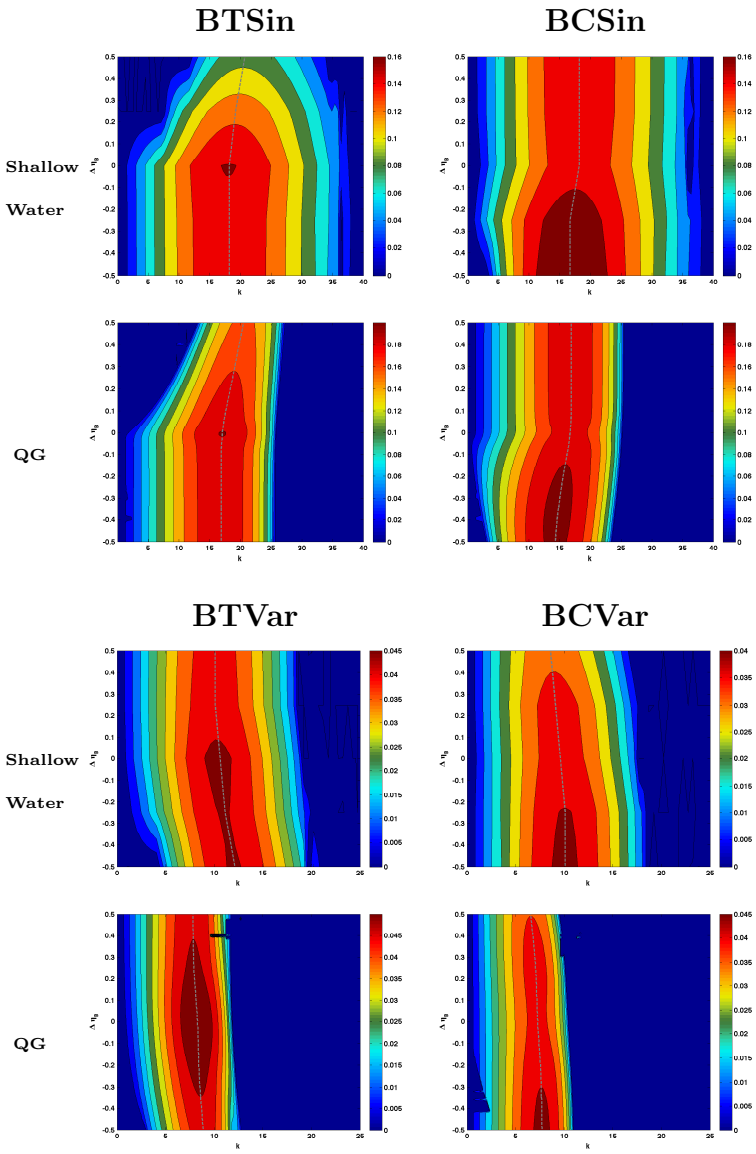


Figure 4.11: The growth rates of each unstable mode in the shallow water model and the QG model for the two-layer BT shear case with strong stratification, $Bu_{BC} = 50$. The dashed line represents position of maximum growth.

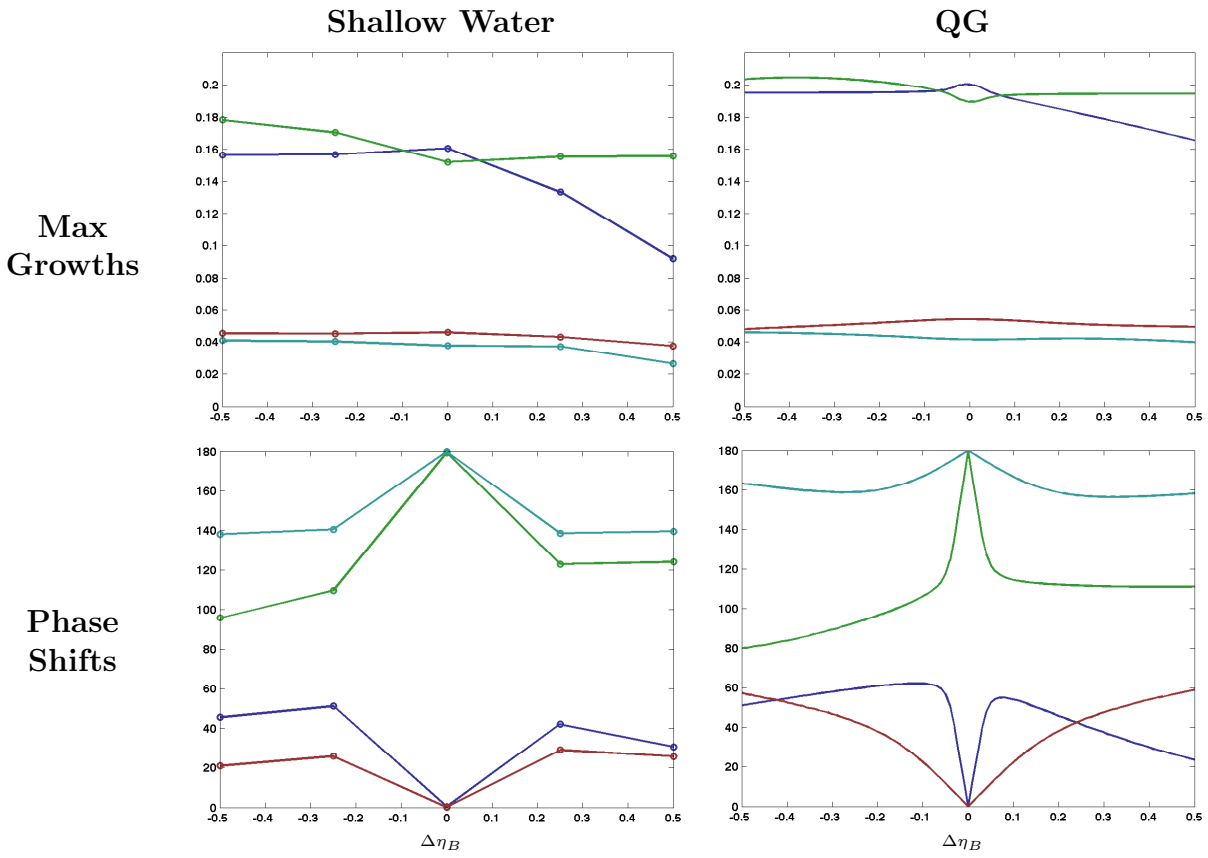


Figure 4.12: Comparing the maximum growth rates, phase speeds of maximum instability, and layer-wise phase shifts of the meridional field for the shallow water stability analysis and the quasi-geostrophic stability analysis for the **strongly stratified two-layer BT shear** profile. The blue line represents the BTSin mode, the green line represents the BCSin mode, the red line represents the BTVar mode and the cyan line represents the BCVar mode.

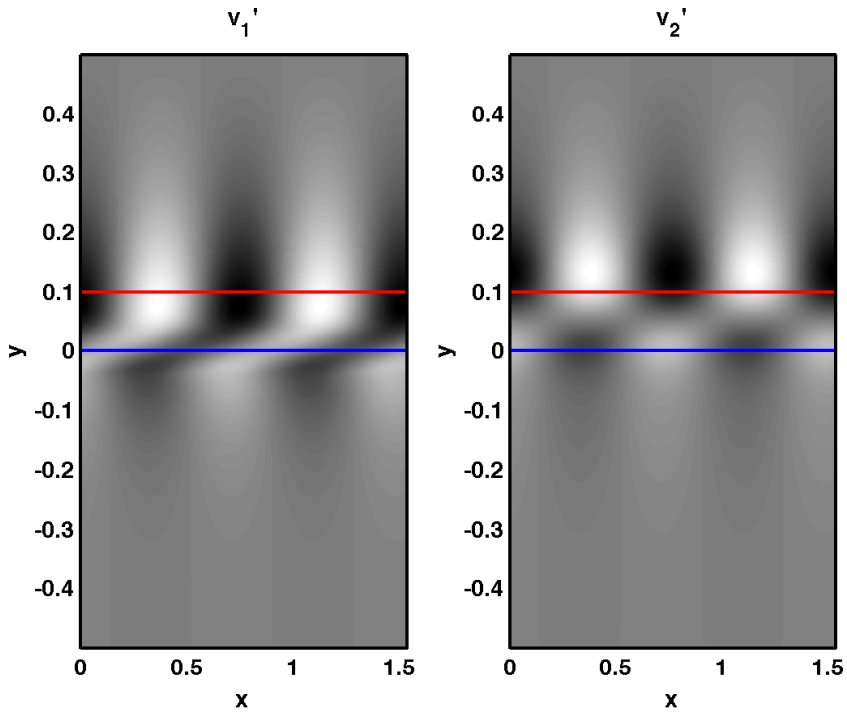


Figure 4.13: The method used for measuring the phase shifts of the modes. The blue line in this image highlights the line $y = 0$, while the red line highlights the $y$ position of maxima for each meridional velocity field.

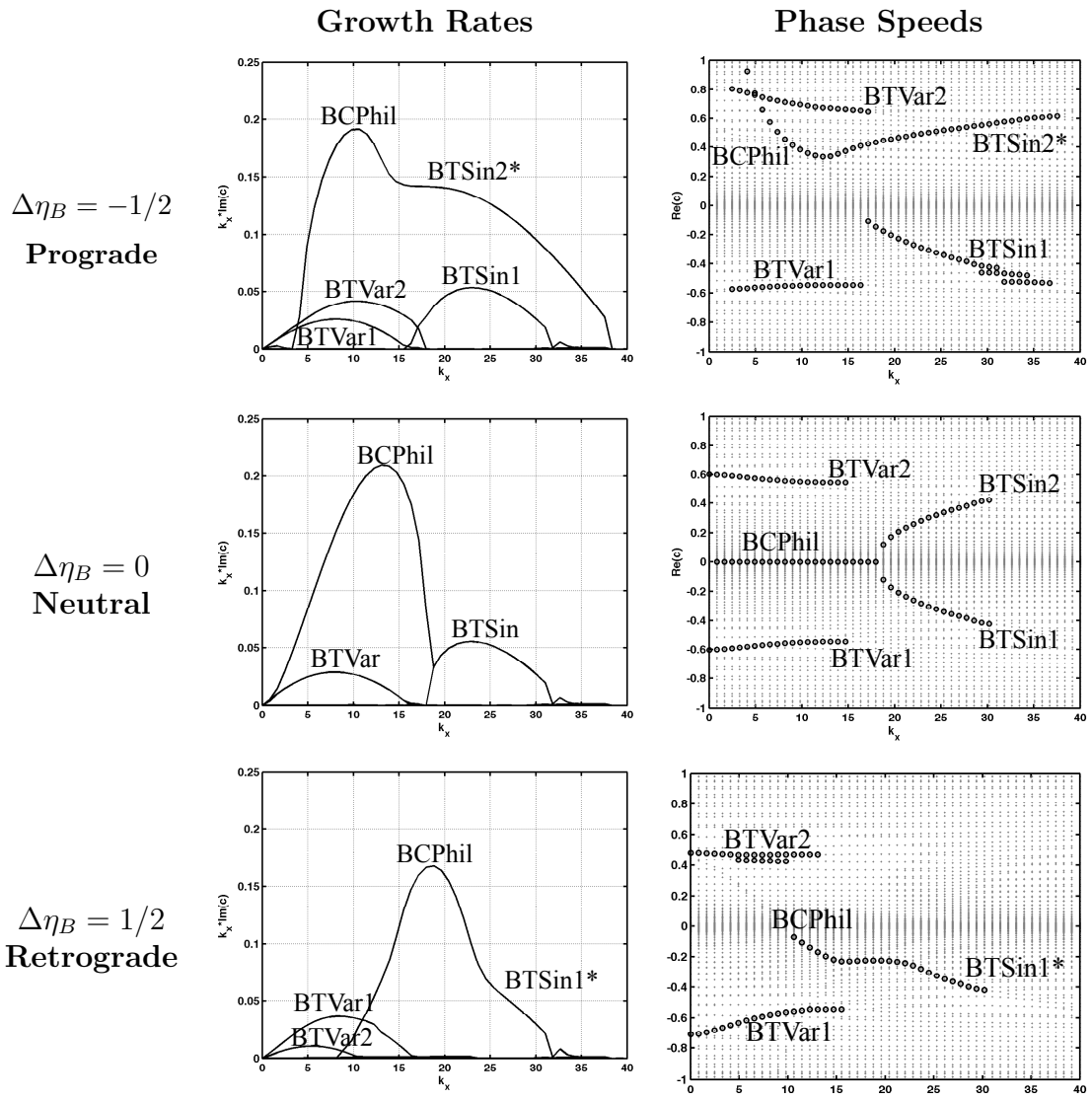


Figure 4.14: Growth rates and phase speeds of the prograde, and retrograde cases for the two-layer mixed BT-BC with no net transport case with weak stratification.

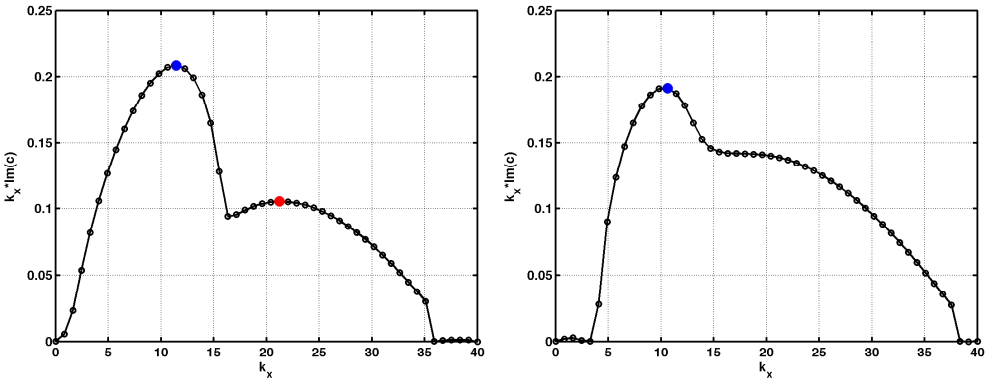


Figure 4.15: The growth rate curves from the shallow water stability analysis for the two-layer mixed BT-BC case with no net transport, corresponding to values of $\Delta\eta_B = -0.25$ (left) and $\Delta\eta_B = -0.50$ (right).

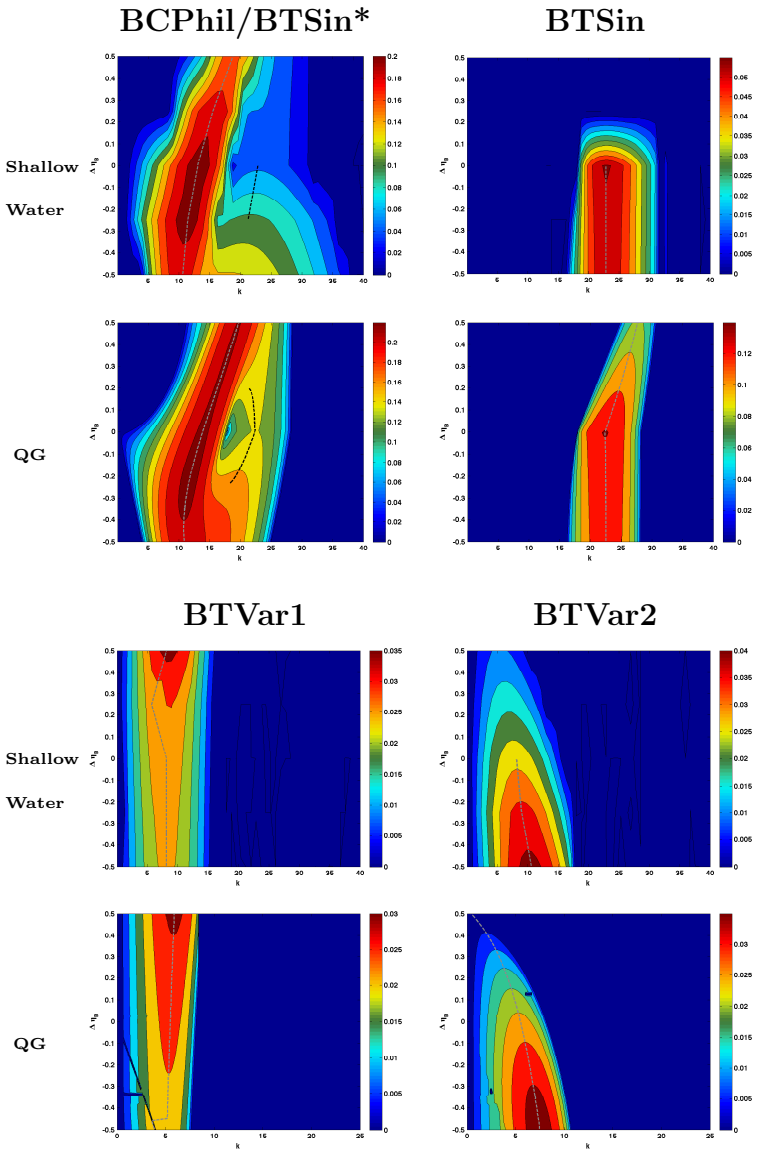


Figure 4.16: The growth rates of each unstable mode in the shallow water model and the QG model for the two-layer mixed BT-BC case with no net transport. The dashed line represents position of maximum growth, the gray dashed line in the left-most plots represents the position of maximum growth for the secondary BTSin mode.

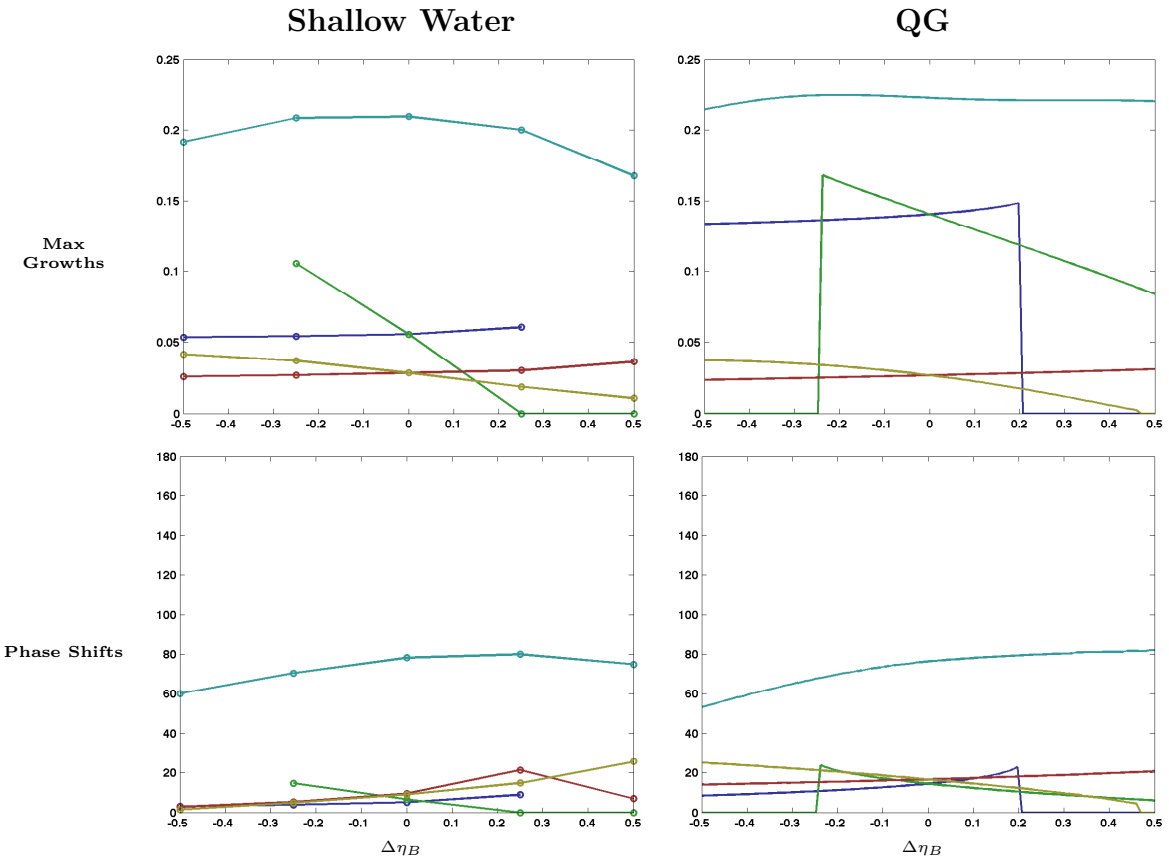


Figure 4.17: The maximum growth rates and vertical phase shifts for the two-layer mixed BT-BC case with no transport with weak stratification. The cyan line represents the BCPhil mode, the blue and green lines represent the sinuous modes, and the red and yellow lines represent the varicose modes.

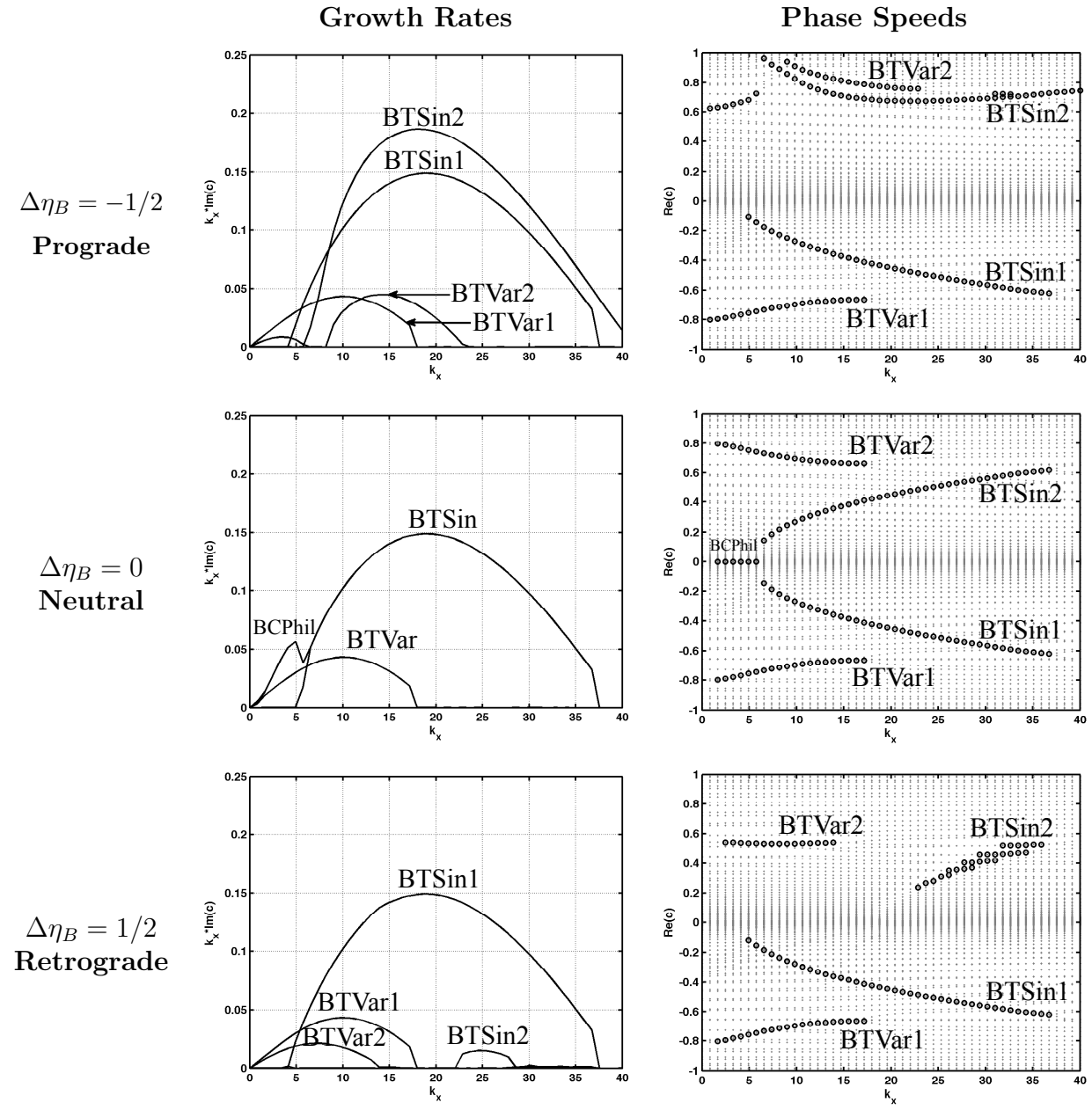


Figure 4.18: Growth rates and phase speeds of the prograde, and retrograde cases for the two-layer mixed BT-BC with no net transport case with strong stratification.

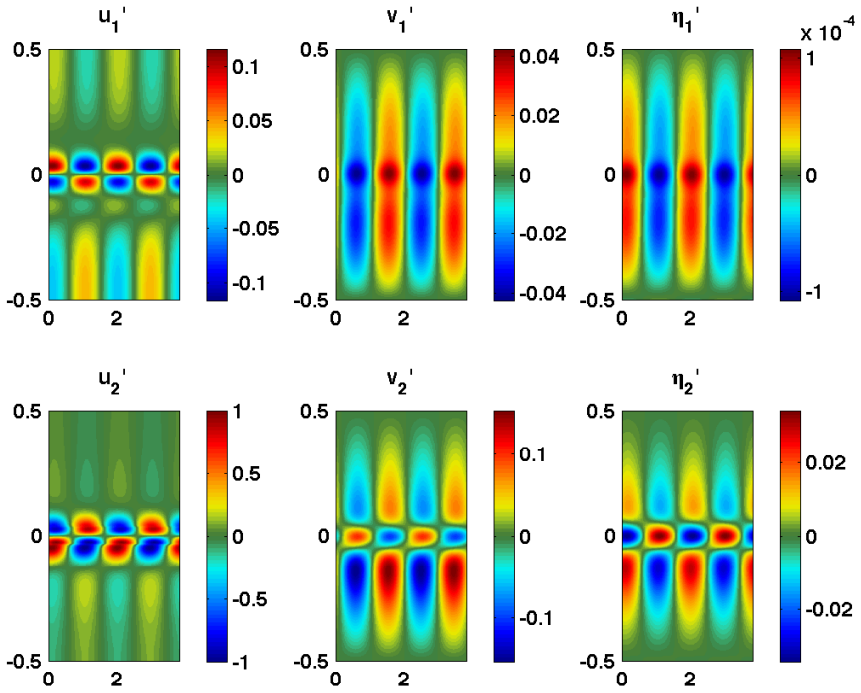


Figure 4.19: The layer-wise modal structure of the weak fifth mode in the strongly prograde regime of the strongly stratified mixed BT-BC with no net transport case.

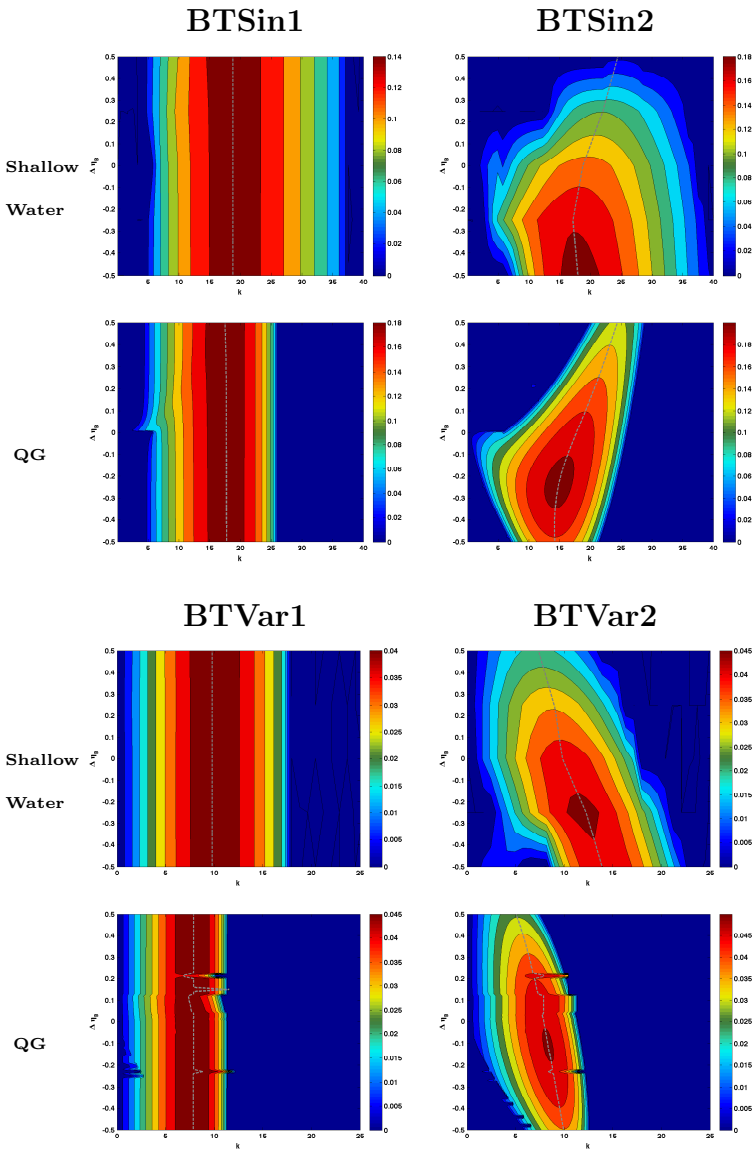


Figure 4.20: The growth rates of each unstable mode in the shallow water model and the QG model for the strongly stratified two-layer mixed BT-BC case with no net transport. The dashed line represents position of maximum growth.

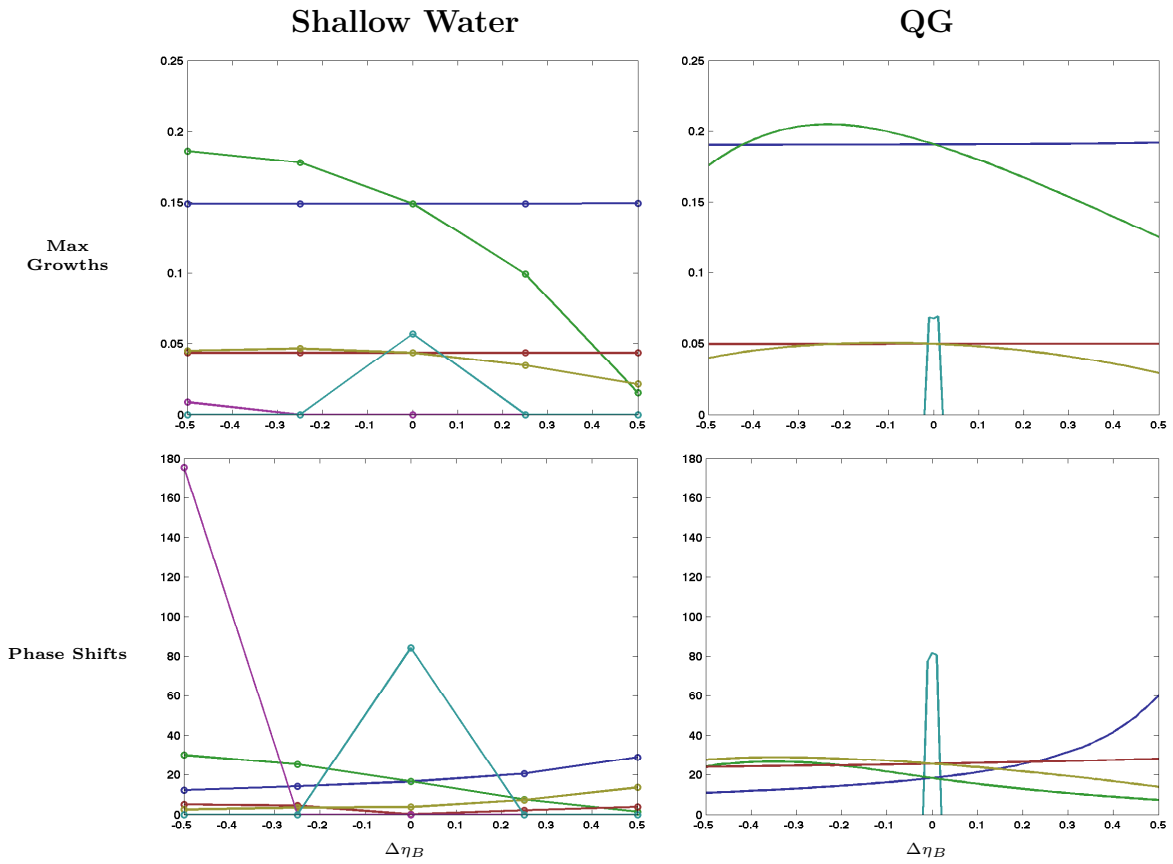


Figure 4.21: The maximum growth rates and vertical phase shifts for the two-layer mixed BT-BC case with no transport with strong stratification. The blue line represents the surface-layer BTSin mode, the green line represents the lower-layer BTSin mode, the red line represents the surface-layer BTVar mode, the yellow line represents the lower-layer BTVar mode, the cyan line represents the BCPhil mode, and the purple line represents the weak fifth mode which is apparent in the strongly prograde regime for the RSW model.

## 4.5 Nonlinear Results

### 4.5.1 Two-Layer Barotropic Shear Flow

The parameters used for these results are $U_{BT} = 1$, and $Bu_{BC} = 5$, corresponding to a weakly stratified, intermediate regime barotropic jet. The cases of prograde, retrograde, and no topography will be shown here.

#### Linear Regime Evolution

Figure 4.22 shows the magnitude of each field as a function of time for each nonlinear run. In the linear stability analysis for the prograde case, it was shown that the dominant mode was the BTSin mode, and the secondary mode was the BCSin mode. Figure 4.23 shows the modal structures of these two modes as predicted by the linear stability analysis, and the output at $t = 50$ from the nonlinear run. It can be seen that the perturbation fields of the nonlinear run appear to tend to the primary BTSin mode. This is unlike the case of no topography, where it was seen that the barotropic and baroclinic fields tended to the BTSin and BCSin modes, respectively. The reason for this is evidenced in the structure of the BTSin mode in figure 4.23. In the case of no topography, it was seen that the primary mode was largely intensified in the barotropic fields, and the secondary mode was largely intensified in the baroclinic fields. For the case of prograde topography, this mode is modified sufficiently such that the barotropic and baroclinic fields are nearly equal in magnitude in the primary mode. The secondary mode is intensified in the baroclinic fields, but only by an order of two, where the neutral case had baroclinic fields larger by an order of $10^4$ (see figure 3.3).

Due to the magnitudes of the BT and BC fields in both modes being similar, the decomposition does not seem to help in quantifying the growth of the distinct modes, and so a layer-wise interpretation is used instead. The layer-wise structures of the linear analysis in figure 4.23 show that the BTSin mode is surface-intensified and the BCSin mode is lower-layer intensified. The mean growth rate for the surface fields was measured to be 0.153, which corresponds to the BTSin mode to within 0.5% difference. The mean growth rate for the lower-layer velocity fields was measured to be 0.140 and corresponds to the BCSin mode to within 3.5% difference. The only field that remains is the $\eta_2'$ field, whose measured growth rate of 0.173 is larger than the growth rates of all modes predicted by linear theory. This is surprising and is presumably due to nonlinear interactions but the author is unable to explain the rationale for this particular behaviour at this time.

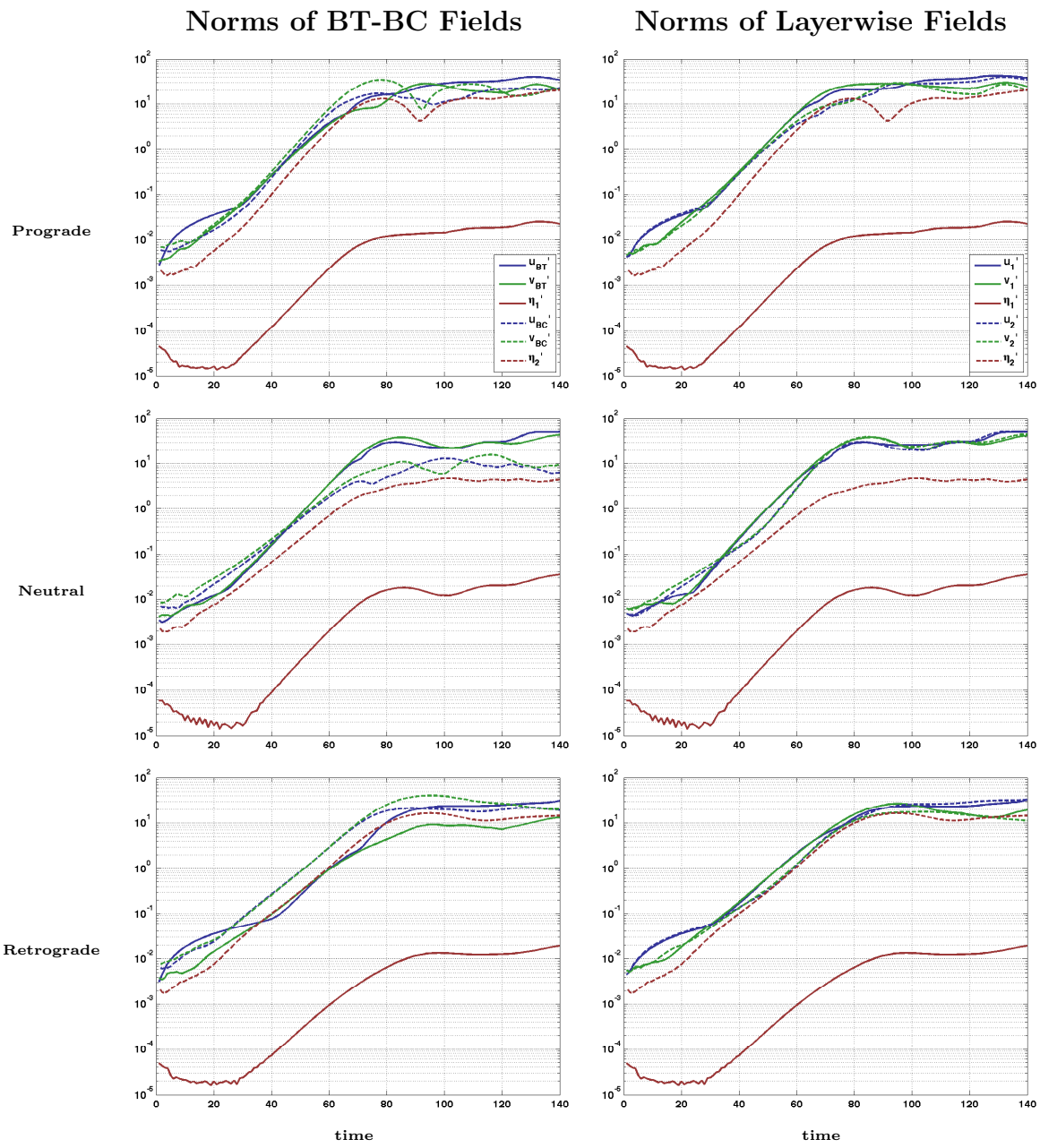


Figure 4.22: The norms of fields for the **two-layer barotropic shear** configuration with prograde topography, no topography and retrograde topography.

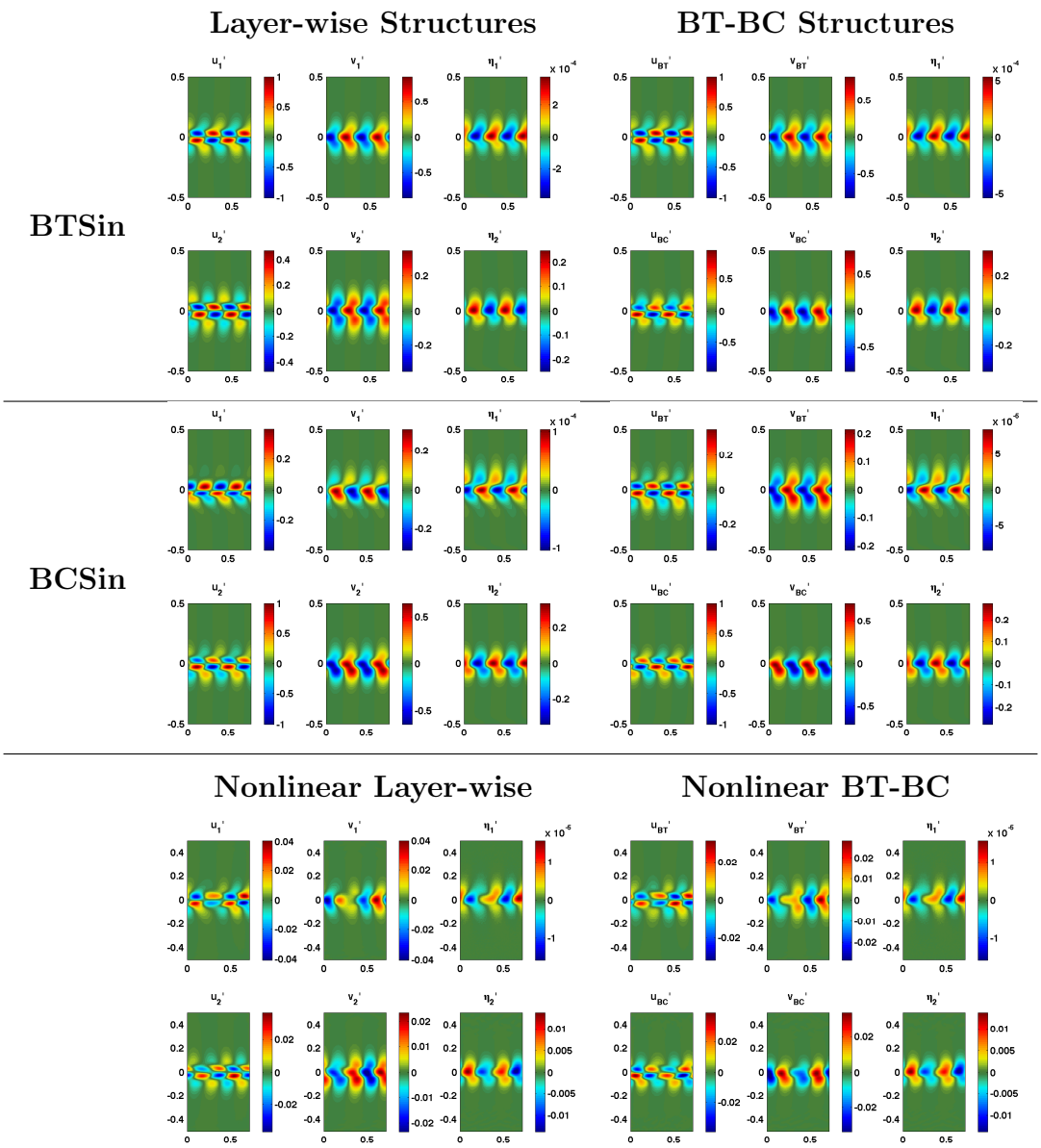


Figure 4.23: The modal structures from the stability analysis for the BTSin mode, and the nonlinear perturbation fields at time $t = 50$ of the **two-layer barotropic shear case with prograde topography**. The $x$- and $y$-axes represents the zonal and meridional positions, respectively.

In the case of no topography, this simulation is analogous to the two-layer mixed BT-BC with no net transport nonlinear simulation of the previous chapter, however the direction of velocity in each layer is reversed. In the center row of figure 4.22, the magnitudes of each BT-BC decomposition field are shown for the case of no topography. It is clear that there are two distinct slopes — the steep slope corresponds to the BT fields, while the shallow slope corresponds to the BC fields. The growth rates for the BT fields agree to within 2.7% of the predicted growth rate of the BTSin mode in linear theory, and the growth rates for the BC fields agree to within 4.9% of the predicted growth rate of the BCSin mode in linear theory.

In the case of retrograde topography, the nonlinear growth rates measured in the regime $t \in (60, 65)$ are measured to be 0.106 for the barotropic fields and 0.126 for the baroclinic fields. In linear theory, the measured maximum growth rate of the primary BTSin mode was 0.109 and the measured maximum growth rate of the BCSin mode was 0.123. The corresponding differences are 2.9% and 1.7%, respectively.

The reason why the specific time regime of $t \in (60, 65)$ was chosen for measuring growth rates was because the $u'_{BT}$ field did not adjust to a growing mode until around $t \sim 55$. This is likely due to the hyperviscosity being too large at the beginning of the simulation. The mean zonal velocity field was slightly dissipated by this term and so the approximation of $u'_{BT}(t) \approx U_0 - u_{BT}(t)$ became inaccurate. In future simulations, the hyperviscosity coefficient will be kept small in the linear regime, and increased in the nonlinear regime where small scale dissipation is more important.

### Nonlinear Adjustment

Figures 4.24 and 4.25 show the layer-wise vorticity fields of the nonlinear simulations. Figure 4.24 shows the fields as the system is entering the nonlinear regime and figure 4.25 shows the fields at the end of the simulations.

The neutral case shows what happens in the absence of topography and will be referred to when comparing the cases with topography. The primary notes of interest for the neutral case are that both layers have similar vorticity fields — implying that the flow has remained largely barotropic in structure. Additionally, it is seen that the structure, strength and size of cyclones and anticyclones is similar. The vorticity field is also centered about $y = 0$.

In the prograde regime (top row of figure 4.24), the topography is oriented such that shallow water occurs when $y < 0$ and deeper water occurs when $y > 0$. It can be seen that the resulting vortices are not as uniform or symmetric about $y = 0$ as in the neutral

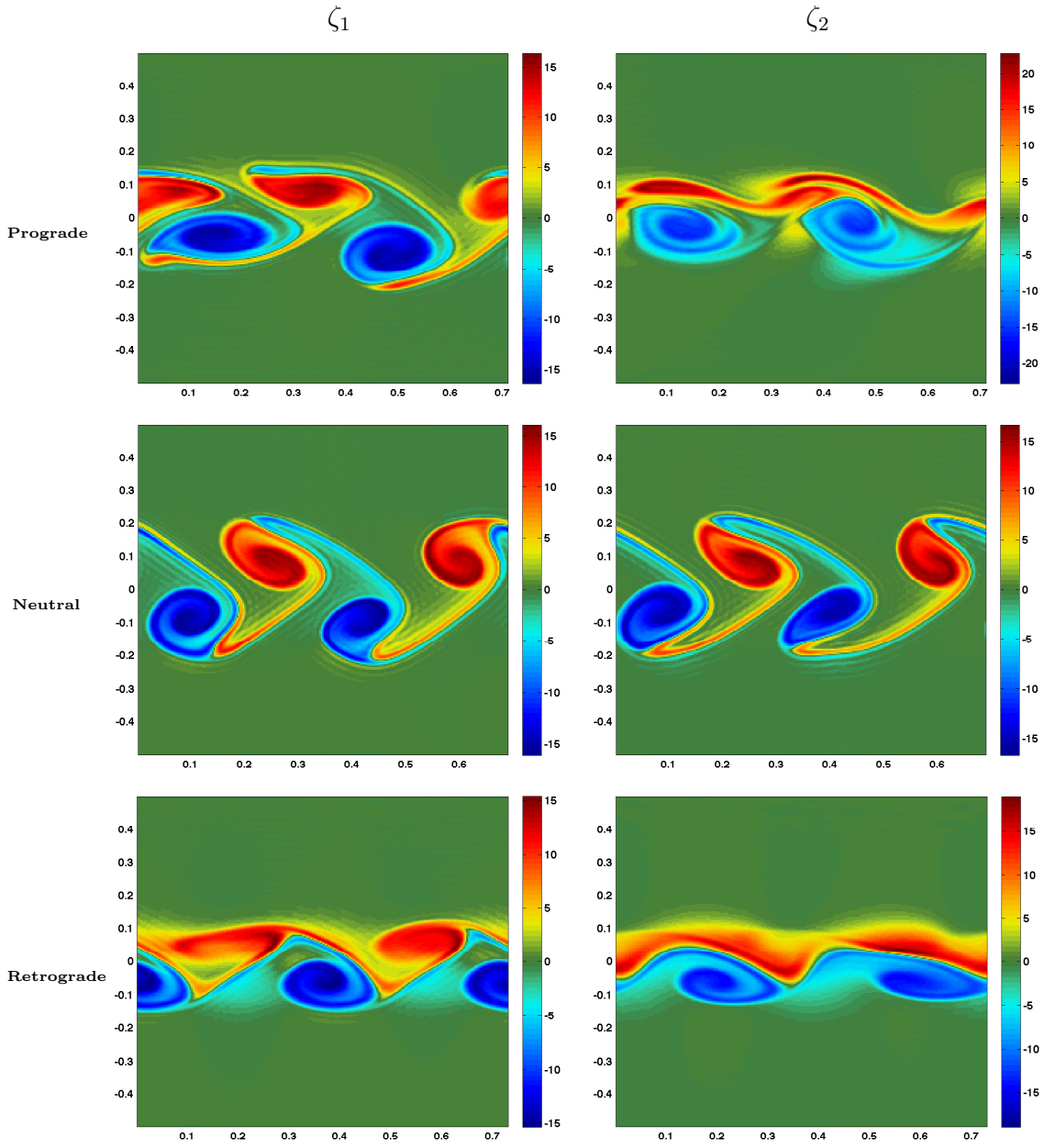


Figure 4.24: The layer wise vorticity fields at $t = 90$ for each two-layer barotropic shear case. The $x$- and $y$-axes represents the zonal and meridional positions, respectively.

case, and that the topography has constrained the extent of the jet. The cyclones are relatively stronger, but much smaller in size than the anticyclones in this regime. This can be explained by the mechanism of vortex stretching, a process that can be understood through the conservation of potential vorticity.
Consider following a vortex tube moving in a flow with vorticity $\zeta_0$. If the vortex tube moves to a different depth by $\Delta h$, it stretches or compresses to maintain mass, as required by the incompressibility requirement. The stretched tube must conserve potential vorticity, meaning that the vorticity $\zeta$ must be modified appropriately. Following [6],

$$PV_2 = PV_1, \tag{4.12}$$

$$\Delta\zeta = \frac{\Delta h}{h_0}(\zeta_0 + f) = \Delta h PV_1. \tag{4.13}$$

Thus if a cyclone in the northern hemisphere ($\zeta_0 + f > 0$) moves to deeper water ($\Delta h > 0$) then the cyclone will increase in strength ($\Delta\zeta > 0$). This is also the cause of the well known cyclone and anti-cyclone asymmetry in the northern hemisphere; for anticyclones with vorticity satisfying $\zeta_0 > -f$, then anticyclones actually become weaker when moving into deep water, [6].
In the context of the top right plot in figure 4.24, the cyclones of the neutral case have "transitioned" into deeper water, effectively stretching out the cyclone's vortex tube, causing it to shrink in horizontal size and increase in relative strength. The anticyclones have transitioned slightly north, causing them to be centered closer to $y = 0$ than $y = -0.1$, as was seen in the case of no topography.

In the retrograde topography case (bottom row of figure 4.24), the jet has been constrained by the presence of topography. The anticyclones have weaker compared to the neutral case, and it is likely the result of the entire system being stabilized by retrograde topography.

In the center row of figure 4.25, the vorticity fields at $t = 140$ of the no topography case are shown. It can be seen that the fields maintain vertical symmetry (both vorticity fields remain similar in structure). The vortices that were seen in the early nonlinear regime have "peeled-off" from each other, and the meridional span of the jet has increased in both layers.

The top row of the figure shows the prograde topography case. The vertical symmetry from the neutral case is not as evident in the prograde case, but it can be seen that the $\zeta_1$ and $\zeta_2$ fields share similar traits — mainly the positions of the largest vortices are similar, suggesting that the flow has remained largely barotropic.

The lower row of figure 4.25 shows the vorticity fields of the retrograde topography case at $t = 140$. Once again, it is obvious that the meridional span of the jet is much

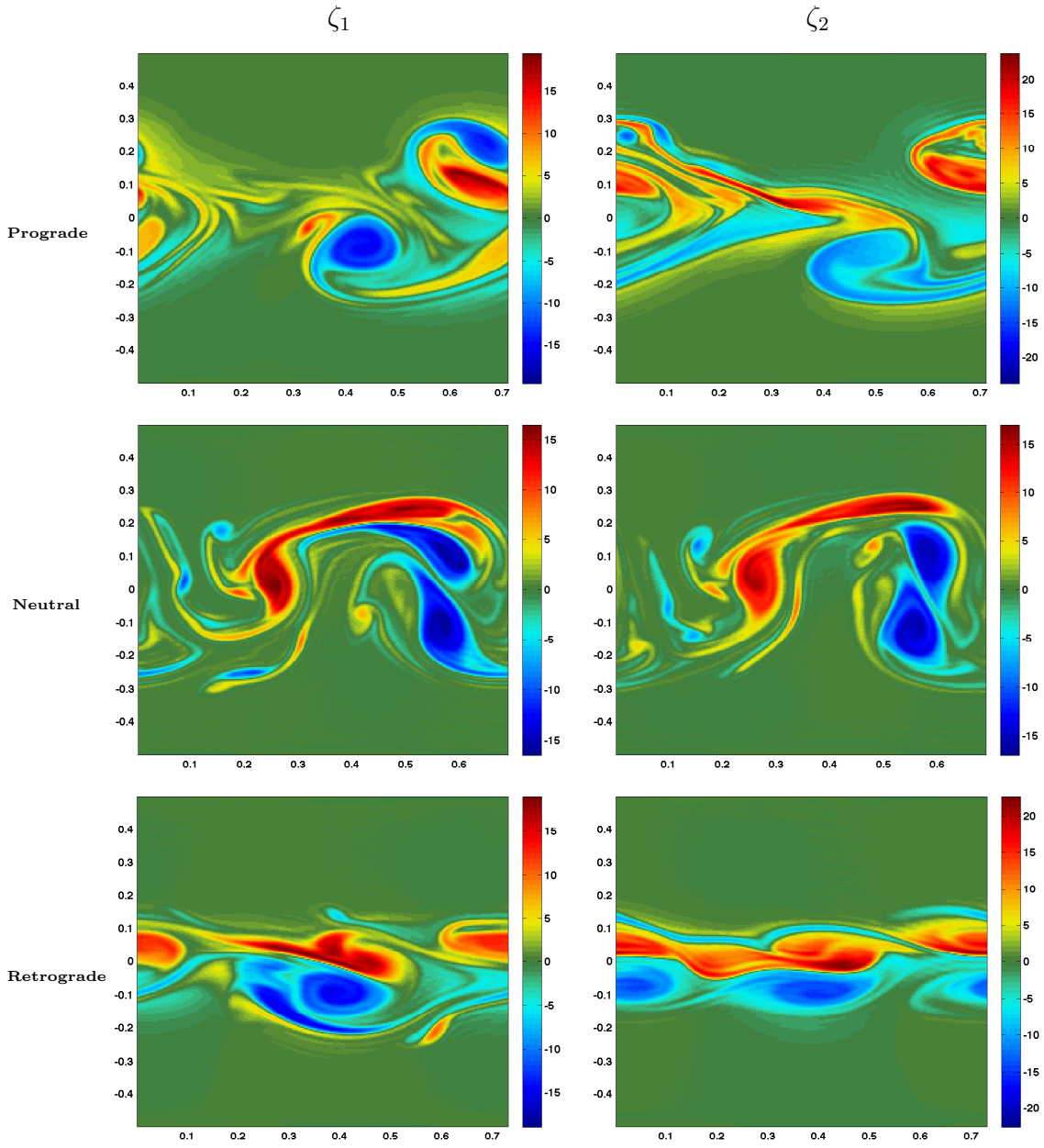


Figure 4.25: The layer wise vorticity fields at $t = 140$ for each two-layer barotropic shear case. The $x$- and $y$-axes represents the zonal and meridional positions, respectively.

smaller than in the prograde and neutral cases. This is consistent with [21] where it was shown that jets in retrograde topography tend to form narrow, coherent vortex streets. The vortical structures are not seen to eject away from the jet, as with the previous cases. This is likely a result of the stabilizing effect of retrograde topography.

### 4.5.2 Two-Layer Mixed Barotropic-Baroclinic with No Net Transport

The parameters used for these results are $U_{BT} = 0$, $U_{BC} = -1$ and $Bu_{BC} = 5$, corresponding to a weakly stratified, intermediate regime mixed BT-BC with no net transport jet.

#### Linear Regime Evolution

Beginning with the case of no topography, it was seen that a linear growth regime occurred for $t \in (40, 60)$. The corresponding growth rates of this regime were measured to be 0.210 in the nonlinear simulation. This compared to a growth rate of 0.209 in the linear stability analysis, resulting in a difference of 1%. Similarly, the prograde case a linear growth regime occurred for $t \in (40, 60)$, with a measured growth rate of 0.189. Compared to the linear stability analysis predicted growth rate of 0.191, this yielded a difference of 1.5%. Finally, in the retrograde case the linear growth regime was seen to be slightly larger, $t \in (40, 65)$. The mean growth rate for all fields in this regime corresponded to 0.167, which compared to the maximum growth rate of the BCPhil mode of 0.168, giving a difference of less than 1%.

#### Nonlinear Adjustment

Figures 4.26 and 4.27 show the layer-wise vorticity fields at $t = 75$ and $t = 100$ (respectively) for each two-layer mixed BT-BC with no net transport case. The case of no topography is used as a reference guide to explain how the flow behaviour changes with topography. The neutral case shows two large-scale structures of cyclonic vorticity begin in each layer. The filaments connecting these structures have a sharp transition between weakly cyclonic and weakly anticyclonic vorticity. Further into the nonlinear regime it is seen that the large-scale structures of positive vorticity are stretched out and deformed about $y = 0$. It is also seen that large-scale anticyclones begin to form away from the

centre of the jet.

The prograde case shows different vorticity fields at $t = 75$. In the surface layer, it appears that the flow is experiencing a meander characteristic of baroclinic instability, [7]. However, in the lower-layer, the instability is drastically different, and appears to be the superposition of a baroclinic meander with a barotropic shear instability. This is consistent with the linear stability analysis, where it was seen that the primary mode was a combined BCPhil/BTVar2 mode. Two cyclones and two anticyclones are formed, with the anticyclones being slightly larger in size, and the cyclones being slightly stronger (this is consistent with the prograde case of two-layer barotropic shear). The filaments connecting these vortical structures show a sharp transition between positive and negative vorticity.

Further into the prograde simulation, at $t = 100$ it is seen that the surface layer has not evolved drastically from the initial onset of nonlinear interactions. The lower-layer has evolved significantly since $t = 75$, and it is seen that the vortical structures are of much smaller scale, and the magnitudes of vorticity are smaller than in the case of no topography.

At $t = 75$, the retrograde case has not evolved past the linear evolution phase, unlike the other two cases. However, it is clear that the horizontal shear instability is beginning in each layer. Near the middle of the jet, there are small-scale strong cyclones — particularly in the lower layer where the peak vorticity is $\sim 3$ times greater than the peak vorticity of the neutral case. Due to these generated cyclones being small, it is noted that sub-mesoscale structures could be formed as a result of this topography. However, the relatively low resolution used may be insufficient to accurately speculate on sub-mesoscale structures.

The final output at $t = 100$ of the retrograde case shows similar structures as the $t = 75$ case in the lower layer, however, there are two distinct positive coherent vortices formed in the upper layer. The peak vorticity in the lower layer is still around $\sim 2.5$ times greater than the peak vorticity in the neutral case.

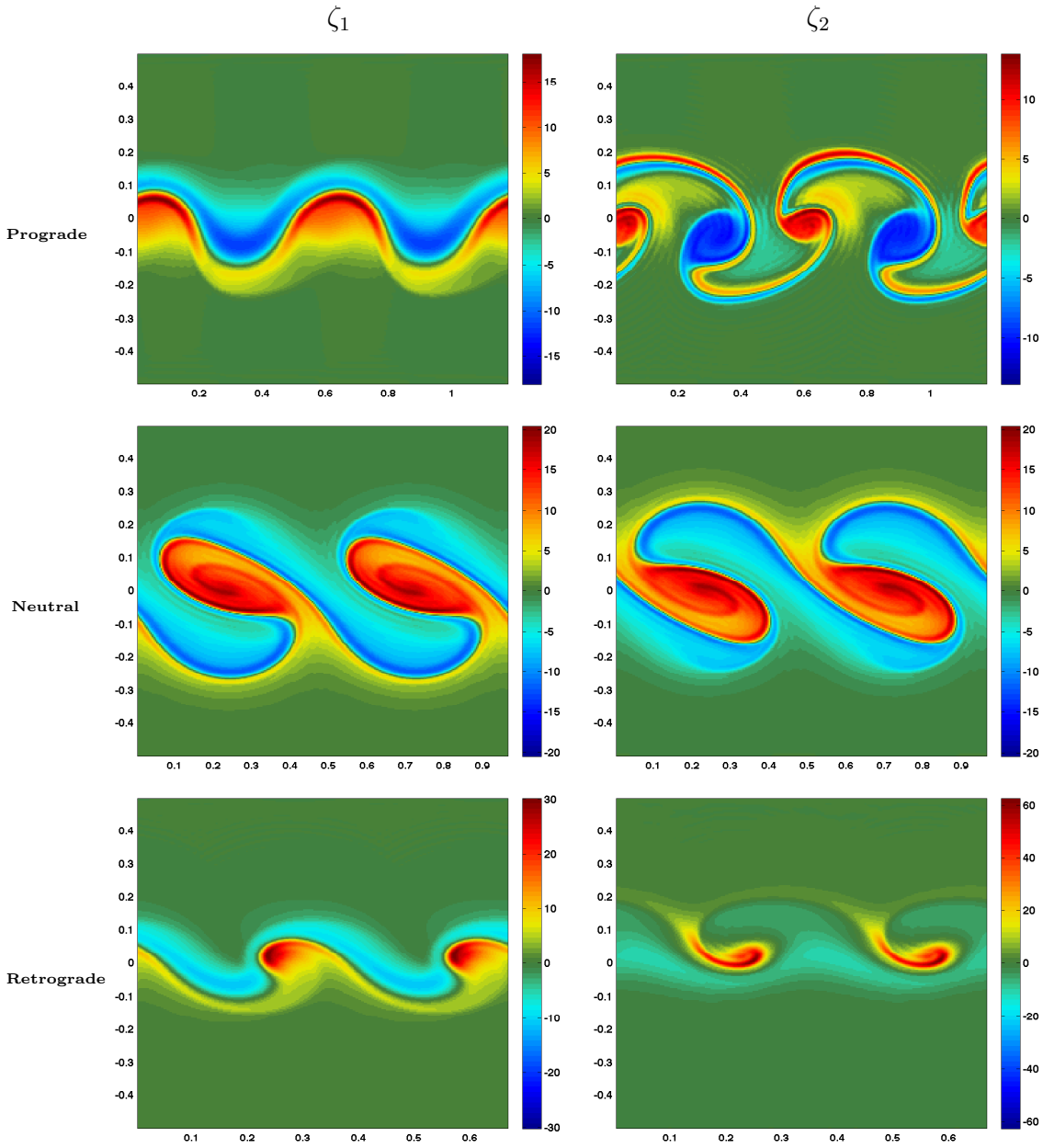


Figure 4.26: The layer wise vorticity fields of the mixed BT-BC with no net transport cases just before the nonlinear phase at $t = 75$. The $x$- and $y$-axes represents the zonal and meridional positions, respectively.

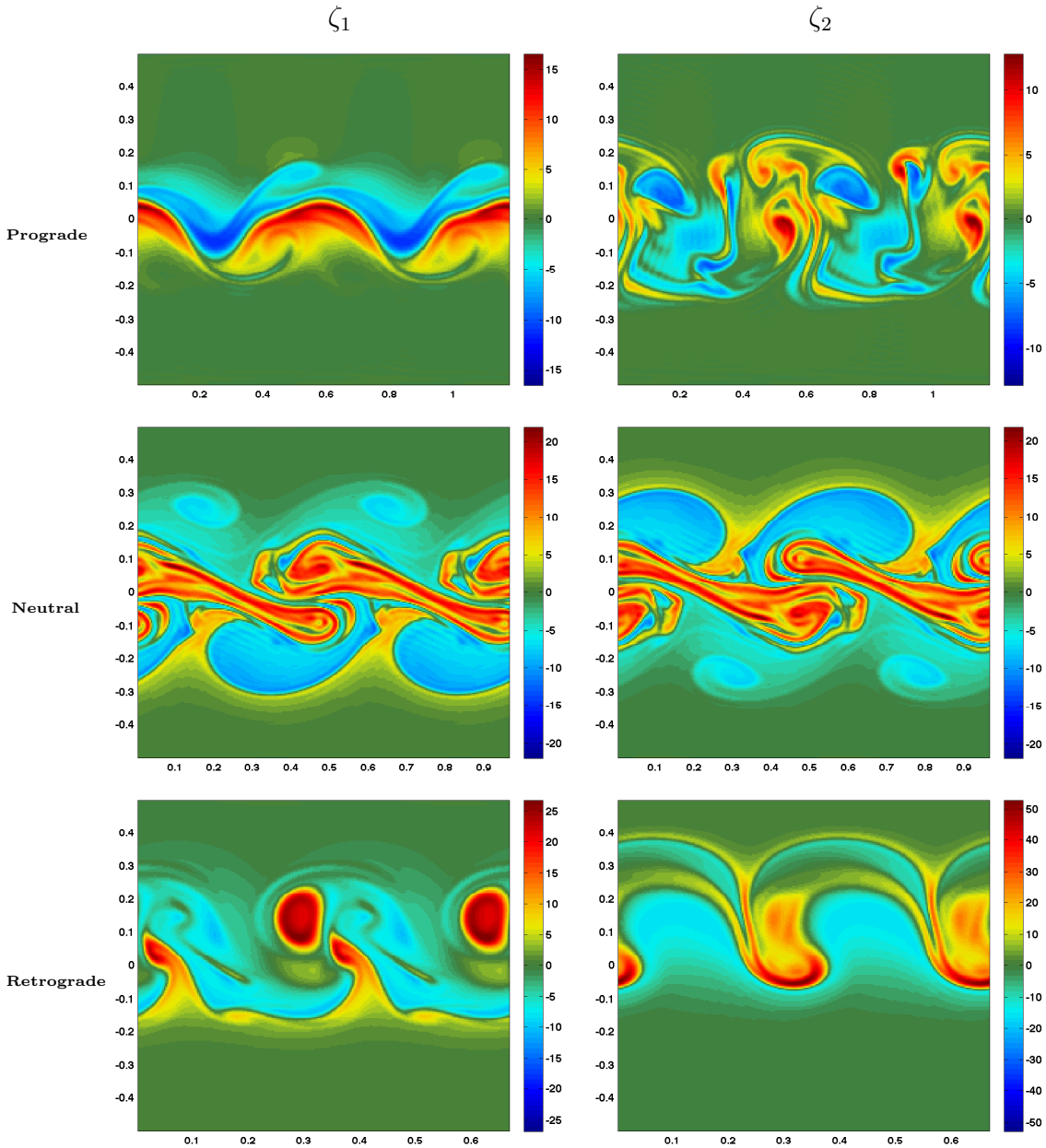


Figure 4.27: The layer wise vorticity fields of the mixed BT-BC with no net transport cases just before the nonlinear phase at $t = 100$. The $x$- and $y$-axes represents the zonal and meridional positions, respectively.

# Chapter 5

# Conclusion

This thesis investigated the stability characteristics and early stage evolution of two-layer mesoscale oceanographic flows. The two-layer RSW and QG models were introduced, and PV was shown to be a material invariant of both models. The concepts of barotropic and baroclinic instability were established using classical models developed by Rayleigh and Kuo, and Phillips. In the following chapters, two-layer flows were subjected to changes in stratification, rotation, and topography. The subsequent effects on the growth rates, phase speeds, and vertical phase shifts were quantified by using numerical solutions of the linearized RSW and QG models. Finally, the fully nonlinear equations were approximated using numerical methods developed in Fortran.

Chapter 3 focused on varying non-dimensional parameters and the effects on stability of different flows. The unstable modes that appeared in the RSW linear stability analysis were classified as *sinuous*, *varicose*, or *Phillips-like* and were further classified as *barotropic* or *baroclinic*. In certain cases, modes were also classified as *surface-* or *bottom-layer intensified*. This classification system allowed for the investigation of the dependence of each type of mode over a large parameter space using the QG model. The QG model was shown to be sufficiently accurate for computing stability characteristics of two-layer mesoscale jets in both the QG and intermediate regimes. It was more accurate for small Rossby numbers and strong stratification parameters, but it was also shown that the model provided good qualitative descriptions outside of the QG regime. The computational efficiency of the model was used to perform broad parameter sweeps in relatively short times. This chapter extended the unstratified model parameter space search conducted in [20].

Three different cases were introduced and studied. In the case of two-layer barotropic

shear it was found that four unstable modes could be realized: two sinuous modes, and two varicose modes — one of each corresponded to a lower-layer intensified mode, while the other corresponded to a surface-layer intensified mode. Two of the modes were barotropic and entirely in phase, and two modes were baroclinic and entirely out of phase. The two barotropic modes were previously well known in literature, and the baroclinic sinuous mode was first observed in [3]. The baroclinic varicose mode was not observed in [3] because the stratification used was too weak. This thesis presented both baroclinic modes and also mapped out the region of parameter space where they might be observed using the semi-analytic QG model. The case of mixed BT-BC shear with no net transport revealed a fifth possible mode of instability, which was referred to as a classical Phillips mode. It was seen in the QG model that the parameter regime in which this mode may exist was severely limited in the presence of strong stratification. It was also seen that in the presence of weak stratification this mode transitioned from a baroclinic Phillips mode to a standard barotropic sinuous mode when the vertical shear became sufficiently weak. The final case which was studied was that of mixed BT-BC shear with non-zero net transport. This case revealed four modes of instability, however, these modes were not easily classified because of asymmetries in the modal structures.

The nonlinear evolution of barotropic sinuous, baroclinic sinuous and baroclinic Phillips modes was then investigated. In general, it was seen that strongly stratified systems tended to decouple layer dynamics, while weakly stratified systems were more strongly coupled. The early stages of nonlinear evolution revealed that the evolution of a system could depend on multiple linear theory modes, and not just the most dominant one, and that the BT-BC decomposition can be used to quantify growth rates of two separate sinuous modes before nonlinear equilibration occurs.

In chapter 4, the effects of topography on two specific multi-layer configurations was investigated. It was seen that when topographic Rossby waves moved with the flow in the lower layer (i.e. the lower layer flow is prograde), there was a range of topography that destabilized the flow. In contrast, when the topographic Rossby waves moved against the flow in the lower layer (retrograde), the flow was stabilized. It was seen that strong stratification dampened the effects of topography on the dynamics of the surface-layer. This chapter extended the unstratified dependence on topography which was conducted in [21].

The linear stability analysis showed that the growth rates and phase speeds of sinuous modes were strongly affected by the presence of topography, while varicose modes were significantly less modified by the presence of topography. Sinuous modes were shifted to smaller length scales in retrograde topography, and larger length scales in prograde

topography. Further, it was shown that there is a parameter regime where a one-layer model may not resolve the dynamics of systems in large topography regimes; specifically, in the RSW model with two-layer barotropic flow and sufficiently strong retrograde topography, the baroclinic sinuous mode became the most unstable mode. It remained to be determined how this result extends to the case of more realistic stratification and what importance, if any, it has on oceanographic shear flows. Additionally, it was shown that the dominant growing mode in systems with no topography did not necessarily remain dominant in the presence of topography. In particular, strongly stratified systems saw different dominant modes for small topographic deformation. The strongly stratified mixed BT-BC shear case with no net transport showed that the classical baroclinic Phillips mode is sensitive to changes in topography. This expands on the results of chapter 3, which showed that in the strongly stratified regime the BCPhil mode was sensitive to vertical shear. It was therefore concluded that the classic Phillips mode of baroclinic instability exists preferentially in weakly stratified regimes.

The nonlinear evolution regime was also shown to become modified in the presence of topography. It was seen that in the two-layer barotropic case the presence of strong topography limited the meridional span of jets well into the nonlinear regime. Additionally, it was seen that in the two-layer mixed BT-BC shear case with no net transport in the presence of prograde topography that the evolving mode showed traces of both baroclinic and barotropic instability, as predicted by the linear analysis.

Overall, this thesis discussed concepts of barotropic and baroclinic instability, and investigated how these instabilities manifested in idealized two-layer flows. Numerical methods were used to approximate and quantify stability characteristics, and to investigate how nonlinear two-layer jets evolve. It was seen that topography can have both stabilizing and destabilizing effects and that strong stratification can decouple layer dynamics. The mesoscale ocean is complicated, and there is no general method of understanding the whole system, however, this work has shown that even simple idealized models can be used to understand complicated processes at fundamental levels.

There are several avenues of potential future work. The two-layer model has proven to be a good paradigm to investigate the dynamics of two-layer jets, but it is restrictive. Using a fully stratified model to investigate the flows presented here would allow for more general conclusions to be made about barotropic and baroclinic mesoscale jets. In chapter 3, it was seen that varying the layer depths could change the dynamics of a two-layer system. This analysis can be expanded to different flows using both the RSW and QG models, combined with nonlinear code. Finally, applying the idealized multi-layer RSW

model to real world flows is another avenue of future research. In particular, applying the three-layer model to the Gulf of Oman is of interest due to available field data and the importance of the area for industrial shipping and transport.

# References


[1] B.K. Arbic and G.R. Flierl. Effects of mean flow direction on energy, isotropy, and coherence of baroclinically unstable beta-plane geostrophic turbulence. J. Phys. Oceanogr., 2004.

[2] E. Boss, N. Paldor, and L. Thompson. Stability of a potential vorticity front: from quasi-geostrophy to shallow water. J. Fluid Mech., 315:65–84, 1996.

[3] F. Bouchut, B. Ribstein, and V. Zeitlin. Inertial, barotropic and baroclinic instabilities of the bickley jet in two-layer rotating shallow water model. Phys. Fluids, pages 126601–1 –22, 2011.

[4] A.J. Bowen and R.A. Holman. Shear instabilities of the mean longshore current. J. Geophys. Res., 94(C12):18023–18030, 1989.

[5] J.G. Charney. The dynamics of long waves in a baroclinic westerly current. J. of Meteor., 4(5):135–162, 1947.

[6] B. Cushman-Roisin and Beckers JM. Introduction to Geophysical Fluid Dynamics: Physical and Numerical Aspects. Academic Press, 2009.

[7] E.T. Eady. Long waves and cyclone waves. Tellus, 1:33–52, 1949.

[8] G.R. Flierl. Models of vertical structure and the calibration of two-layer models. Dyn. Atmos. Ocean, 2(341-381), 1978.

[9] G.R. Flierl, P. Malanotte-Rizzoli, and N.J. Zabusky. Nonlinear waves and coherent vortex structures in barotropic $\beta$-plane jets. J. Phys. Oceanogr., 17:1408–1438, 1987.

[10] R.L. Irwin and F.J. Poulin. Instabilities in an idealized two-layer ocean model with weak stratification. J. Phys. Oceanogr., 2014.

[11] P.E. Isachsen. Baroclinic instability and eddy tracer transport across sloping bottom topography: How well does a modified eady model do in primitive equation simulations? Ocean Modelling, 2010.

[12] J. Lambaerts, G. Lapeyre, and V. Zeitlin. Moist versus dry baroclinic instability in a shallow-water model of the atmosphere with moist convection. J. Atmos. Sci., 68(1234-1252), 2011.

[13] J. Lambaerts, G. Lapeyre, and V. Zeitlin. Moist versus dry baroclinic instability in a simplified two-layer atmospheric model with condensation and latent heat release. J. Atmos. Sci., 69(1405-1426), 2012.

[14] M.S. Lozier and M.S.C. Reed. The influence of topography on the stability of shelf-break fronts. J. Phys. Oceanogr., 35:1023–1036, 2005.

[15] M.J. Molemaker, J.C. McWilliams, and I. Yavneh. Baroclinic instability and loss of balance. J. Phys. Oceanogr., 35:1505–1517, 2005.

[16] P.P. Niiler and L.A. Mysak. Barotropic waves along an eastern continental shelf. Geophys. Astrophys. Fluid Dyn., 1971.

[17] J. Pedlosky. A study of the time dependent ocean circulation. J. Atmos. Sci., 22:267–272, 1965.

[18] J. Pedlosky. Geophysical Fluid Dynamics. Springer-Verlag, 1987.

[19] N.A. Phillips. Energy transformations and meridional circulations associated with simple baroclinic waves in a two-level geostrophic model. Tellus, 6:273–286, 1954.

[20] F.J. Poulin and G.R. Flierl. The nonlinear evolution of barotropically unstable jets. J. Phys. Oceangr., 33(10), 2003.

[21] F.J. Poulin and G.R. Flierl. The influence of topography on the stability of jets. J. Phys. Oceangr., 35:811–825, 2005.

[22] F.J. Poulin, A. Stegner, M. Hernandez-Arencibia, A. Marrero-Diaz, and P. Sangra. Steep shelf stabilization of the bransfield coastal current: linear stability analysis. J. Phys. Oceanogr., 44:714–732, 2014.

[23] B. Ribstein, R. Plougonven, and V. Zeitlin. Inertial versus baroclinic instability of the bickley jet in continuously stratified rotating fluid. J. Fluid Mech., 743:1–31, 2014.

[24] P. Sangra, C. Gordo, M. Hernandez-Arencibia, A. Marrero-Diaz, A. Rodriguez-Santana, A. Stegner, A. Martinez-Marrero, J.L. Pelegri, and T. Pichon. The Bransfield current system. Deep-Sea Research I, 2011.

[25] X.J. Carton T. Meunier and R. Duarte. Influence of a deep flow on a surface boundary current. Geophys. Astrophys. Fluid Dyn., 2012.

[26] L.D. Talley. Radiating barotropic instability. J. Phys. Oceanogr., 13:972–987, 1983.

[27] L.D. Talley. Radiating instabilities of thin baroclinic jets. J. Phys. Oceanogr., 13:2161–2181, 1983.

[28] L.D. Talley, G.L. Pickard, W.J. Emery, and J.H. Swift. Descriptive Physical Oceanography: An Introduction. Elsevier, 2011.

[29] L.N. Trefethen. Spectral Methods in MATLAB. SIAM, 2000.

[30] G.K. Vallis. Atmospheric and Oceanic Fluid Dynamics. Cambridge University Press, Cambridge, U.K., 2006.

[31] P. Wang, J.C. McWilliams, and Z. Kizner. Ageostrophic instability in rotating shallow water. J. Fluid Mech., 712:327–353, 2012.